A&A 460, 467–485 (2006)
DOI: 10.1051/0004-6361:20053872

Astronomy & Astrophysics

A survey of submillimeter C and CO lines in nearby galaxies⋆

E. Bayet[1], M. Gerin[1], T. G. Phillips[2], and A. Contursi[3]

[1] Laboratoire de Radioastronomie (LRA), Observatoire de Paris and École Normale Supérieure (CNRS-UMR 8112), 24 rue Lhomond, 75005 Paris, France
e-mail: estelle.bayet@lra.ens.fr
[2] California Institute of Technology, Downs Laboratory of Physics 320-47, Pasadena, CA 91125, USA
[3] Max Planck Institute fuer Extraterrestrische Physik, Giessenbachstrasse, 85748 Garching, Germany

Received 21 July 2005 / Accepted 21 August 2006

ABSTRACT

Aims. While the search for molecular gas in distant galaxies is based on the detection of submillimeter CO rotational lines, the current CO surveys of nearby galaxies are restricted to the millimeter CO lines. The submillimeter CO lines are formed in warm and dense molecular gas and are therefore sensitive to the physical conditions whereas the CO ($J = 1 \rightarrow 0$) line is a tracer of the total molecular gas mass. In order to be able to compare the properties of molecular gas in nearby and distant galaxies, we have observed C and CO submillimeter lines (including the ^{12}CO(6−5) and ^{12}CO(7−6) lines) in a sample of nearby galaxies using the *Caltech Submillimeter Observatory (CSO)*.

Methods. We have obtained a complete view of the CO cooling curve (also called CO spectral energy distribution) by combining the submillimeter CSO data with previous observations found in the literature. We made use of Large Velocity Gradient (LVG) models to analyse the observed CO cooling curve, predict CO line intensities from $J = 1 \rightarrow 0$ to $J = 15 \rightarrow 14$ in the studied galaxies, and derive the physical properties of the warm and dense molecular gas : the kinetic temperature (T_K); the gas density ($n(H_2)$); the CO column density divided by the line width $N(^{12}CO)/\Delta v$. The predictions for the line intensities and for the total CO cooling power, obtained from LVG modelling have been compared with predictions from Photo Dissociation Regions (PDR) models.

Results. We show how the CO SED varies according to the galaxy star forming activity. For active nuclei, the peak is located near the ^{12}CO(6−5) or ^{12}CO(7−6) rotational lines, while, for normal nuclei, most of the energy is carried by the ^{12}CO(4−3) and ^{12}CO(5−4) lines. Whatever the spectral type of the nucleus, the observed C cooling rate is lower than the observed CO cooling rate (by a factor of $\geqslant$4). The CO cooling curve of nearby starburst galaxies (e.g. NGC 253) has a quite similar shape to the CO cooling curve of distant galaxies. Therefore, the CO cooling curves are useful diagnostics for the star forming activity in distant objects.

Key words. galaxies: starburst – galaxies: ISM – galaxies: nuclei – submillimeter – ISM: molecules

1. Introduction

It is well known that the far infrared fine-structure lines of abundant elements (oxygen, carbon, nitrogen, silicon, sulfur, etc.), either in their neutral or ionized states, contribute most of the gas cooling of the interstellar medium in galaxies (Hollenbach & Tielens 1999; Goicoechea et al. 2005). Far infrared fine-structure lines from ionized atoms are useful tracers of HII regions (e.g. Goicoechea et al. 2005). For the neutral ISM, the main cooling lines are those of ionized carbon [CII] and neutral oxygen [OI]. By analyzing a set of ISO observations of external galaxies, Malhotra et al. (2001) have concluded that PDRs contribute to a large fraction of the emission of the [CII] and [OI] lines. In molecular gas, the cooling radiation due to atomic carbon and carbon monoxide is significant. The theoretical predictions (Goldsmith & Langer 1978; Hollenbach & Tielens 1999) have been confirmed by the COBE-FIRAS and ISO-LWS observations of the Milky Way: apart from [CII], [OI], [OII] and [NII], the most intense lines are from C and CO. The relative contributions of the different lines of C and CO vary along the Galactic plane : the brightest lines and more excited states are seen towards the Galactic Center, while the rest of the disk shows lower excitation. Also, C contributes less in proportion to the total cooling towards the Galactic Center than towards the disk (Bennett et al. 1994; Fixsen et al. 1999).

The CO cooling is typically provided by the submillimeter lines, with rotational quantum numbers between 3 and 8 (Bayet et al. 2004). Such observations can be performed from high altitude dry mountain sites, such as the Mauna Kea summit in Hawaii. Previous studies using the *James Clerk Maxwell Telescope* (*JCMT*) and the *CSO* have shown that the ^{12}CO(4−3) line is generally bright in galaxy nuclei (Guesten et al. 1993; Israel et al. 1995; Israel & Baas 2001, 2003; Kramer et al. 2005, ...). Much less information is available on the other high frequency CO lines. The first report of extragalactic ^{12}CO(6−5) detections was published by Harris et al. (1991) 15 years ago. In the past years new analyses of the ^{12}CO(6−5) and ^{12}CO(7−6) emission have been presented by Ward et al. (2001, 2003) for M 82, and by Bradford et al. (2003) and Bayet et al. (2004) for NGC 253 and Henize 2−10. A first comparison of the CO line spectrum, also called "CO SED" (see Weiß et al. 2005; Mao et al. 2000, ...) in star forming galaxies is presented by Bayet et al. (2004). They show that the CO line spectrum is very similar in the two star forming galaxy nuclei, NGC 253 and Henize 2−10. Distant starburst galaxies seem also to share the same CO spectrum

⋆ Appendices A and B and Figs. 4, 5, 8–11, 13, 15, 16 are only available in electronic form at http://www.aanda.org

Table 1. Basic properties of the sample galaxies.

	Type	RA(1950)	Dec(1950)	Dist. (Mpc)	Velocity LSR ($km\,s^{-1}$)	Optical size[a]	Metallicity: $12+\log\frac{O}{H}$
IC 10	dIrr IV/BCD[a]	00:17:44.0	59:00:18.0	1[1]	–344	6.8′×5.8′	8.31 ± 0.20[14]
NGC 253[b]	SAB(s)c;H_{II}, Sbrst	00:45:05.7	–25:33:38.0	2.5[18]	240	27.5′×6.8′	8.99 ± 0.31[16]
IC 342	SAB(rs)cd HII[a]	03:41:57.2	67:56:27.0	1.8[2]	35	21.4′×20.9’	≈9.30[15]
Henize 2−10[b]	I0 pec, Sbrst	08:34:07.2	–14:26:06.0	6[17]	850	30″× 40 ’’	≈8.93[16]
M 82	I0;Sbrst HII[a]	09:51:43.8	69:55:00.9	3.2[3]	200	11.2′×4.3′	9.00 ± 0.12[14]
NGC 3079	SB(s)c;LINER Sy2[a]	09:58:35.0	55:55:15.4	15.6[4]	1331	7.9′×1.4′	–
IRAS 10565+2448	LINER HII[a]	10:56:36.2	24:48:40.0	172[5]	12 923	0.4′×0.3′	–
NGC 4038	SB(s)m pec[a]	11:59:19.0	–18:35:23.0	13.8[6]	1634	5.9′×3.2′	–
Overlap	SA(s)m pec[a]	11:59:21.1	–18:36:17.0	13.8[6]	1510	3.1′×1.6′	–
NGC 4736	(R)SA(r)ab;Sy2 LINER[a]	12:48:32.4	41:23:28.0	4.3[7]	314	11.2′×9.1’	9.01 ± 0.17[16]
Mrk 231	SA(rs)c? pec Sy1[a]	12:54:05.0	57:08:39.0	173.9[8]	12 650	1.3′×1.0′	–
Centaurus A	S0 pec Sy2[a]	13:22:31.6	–42:45:32.0	3.5[9]	550	25.7′×20.0’	–
M 51	SA(s)bc pec; HII Sy2.5[a]	13:27:46.1	47:27:14.0	9.6[10]	470	11.2′×6.9’	9.23 ± 0.12[16]
M 83	SAB(s)c; HII Sbrst[a]	13:34:11.3	–29:36:42.6	3.5[11]	516	12.9′×11.5′	9.16 ± 0.12[16]
Arp 220	S?;LINER; HII Sy2[a]	15:32:46.7	23:40:08.0	77[10]	5450	1.5′×1.2′	–
NGC 6090	Sd pec HII[a]	16:10:23.9	52:35:11.0	118[12]	8831	2.8′×1.5′	–
NGC 6946	SAB(rs)cd HII[a]	20:33:48.8	59:58:50.0	5.5[13]	50	11.5′×9.8′	9.06 ± 0.17[16]

References: 1: Adopted value (see text); 2: McCall (1989); Karachentsev & Tikhonov (1993); 3: Dumke et al. (2001) consistent with the value of Tammann & Sandage (1968); 4: Sofue et al. (1999); 5: Glenn & Hunter (2001); 6: Saviane et al. (2004); 7: Tully & Fisher (1987); 8: Bryant & Scoville (1999); 9: de Vaucouleurs et al. (1979); 10: de Vaucouleurs (1991); 11: Thim et al. (2003); 12: Redshift from Gerin & Phillips (1999) with $H_0 = 75\ km\,s^{-1}\,Mpc^{-1}$; 13: Tully (1988); 14: Arimoto et al. (1996); 15: Vila-Costas & Edmunds (1992); Garnett (1998); 16: Zaritsky et al. (1994); 17: Johansson (1987); 18 : As in Mauersberger et al. (1996) (see Bayet et al. (2004)); [a]: Data from the NED database; [b]: See Bayet et al. (2004) to obtain more information on the properties of NGC 253 and Henize 2−10.

(Cox et al. 2002; Bertoldi et al. 2003; Carilli et al. 2004; Pety et al. 2004; Walter et al. 2004; Carilli et al. 2005, ...).

Although contributing less than CO, atomic carbon is an important coolant in the ISM (Gerin & Phillips 2000). While observations of the ground state line ($^3P_1-^3P_0$ at 492 GHz) can be found in the literature for a few tens of sources (e.g. Gerin & Phillips 2000; Israel & Baas 2002) there are very few reported detections of the excited line ($^3P_2-^3P_1$ at 809 GHz) although the contribution of the latter line to the neutral carbon cooling is at least similar to the contribution of the ground state line (Stutzki et al. 1997; Bayet et al. 2004).

As potential tracers of the gas cooling, submillimeter C and CO lines are expected to provide information on the gas heating rate, which is dominated by the incident FUV radiation, mainly due to massive and young stars. Therefore, the molecular cooling lines are expected to provide information on the galaxy star forming activity, as do the fine structure lines in the far infrared. In order to have a full picture of the CO cooling, the contribution of missing CO lines (blocked by the Earth's atmosphere) can be predicted from the series of observed lines, using state-of-the-art radiative transfer models. The method has been presented in our previous paper (Bayet et al. 2004). In this paper, we present in this paper results of a survey of the C and CO submillimeter lines in a sample of nearby galaxies. The data are used for the two following purposes: *i) determination of the molecular cooling rate in galaxies of different morphological type; ii) study the shape of the CO cooling curves obtained in the target galaxies*. From this analysis, we show that the combined information on C and CO submillimeter line spectra can be used as a powerful diagnostic of galaxy star forming activity.

The galaxy sample is presented in Sect. 2, the observations parameters are described in Sect. 3, while the resulting spectra and maps are introduced in Sect. 4. We discuss in Sect. 5 how we use LVG and PDR models for fitting the series of observed CO lines. In Sect. 6, we compare results obtained for the center of Milky Way and for the Cloverleaf QSO with those derived from this work for our galaxy sample. The main conclusions are summarized in Sect. 7.

2. The sample

We have selected galaxies which are bright in the $^{12}CO(1-0)$ and $^{12}CO(2-1)$ lines and are nearby (distance less than 20 Mpc, except for the two ULIRGs Arp220 and Markarian 231). Galaxies have also been selected to have a large variety of galaxy types. The sample includes normal spiral galaxies (IC 342, M 51, NGC 4736, NGC 6946), starburst galaxies (M 82, M 83, NGC 253, NGC 3079), irregular, star forming galaxies (IC 10, Henize 2−10), interacting galaxies (The Antennae, NGC 6090), ULIRGs (Arp 220, IRAS 10565+2448, Markarian 231) and the elliptical galaxy Centaurus A. In this work, we analyzed two positions in the Antennae galaxies: the nucleus of the northern component, NGC 4038, and a position named "Overlap" hereafter, which corresponds to the position of the most massive H_2 concentration, not very far from the nucleus of NGC 4039 (the coordinates of NGC 4038 and Overlap are listed in Table 1). Intense MIR emission due to star formation has been detected at the Overlap position (Vigroux et al. 1996) as well as bright CO lines (GMC4-5 in Wilson et al. 2000) .

Properties of the sample galaxies are summarized in Table 1. Although it is not a complete sample (because these observations are difficult and time consuming) it includes representative types of nearby galaxies.

3. Observations

The observations were made during various sessions at the *Caltech Submillimeter Observatory* (*CSO*) in Hawaii (USA) with the Superconducting Tunnel Junction receivers operated in double-side band mode. The atmospheric conditions varied

from good ($\tau_{225} \lesssim 0.1$) to excellent ($\tau_{225} \approx 0.06$). We used a chopping secondary mirror with a frequency of around 1 Hz. We used a 3′ chopping throw for the [CI]($^3P_1-^3P_0$), CO(2−1), CO(3−2) and CO(4−3) lines. There is no sign of contamination by emission in the off beams. We restricted the chopping throw to 1′ for [CI]($^3P_2-^3P_1$), CO(6−5) and CO(7−6) as the emission is very compact in these lines. Spectra were measured with two acousto-optic spectrometers (effective bandwidth of 1000 MHz and 500 MHz). The first one has a spectral resolution about 1.5 MHz and the second one about 2 MHz. The IF frequency of the CSO receivers is 1.5 GHz. The main beam efficiencies (η) of the CSO were 69.8%, 74.6%, 51.5%, 28% and 28% at 230, 345, 460, 691 and 806 GHz respectively, as measured on planets[1]. For the [CI]($^3P_1-^3P_0$) and the [CI]($^3P_2-^3P_1$) lines, we used receivers at 492 and 809 GHz, so η = 51.5% and 28%, respectively. We used the ratio $\frac{1}{\eta}$ to convert T_A^* into T_{mb}. The beam size at 230, 345, 460, 691 and 806 GHz is 30.5″, 21.9″, 14.5″, 10.6″ and 8.95″[1]. The pointing was checked using planets (Jupiter, Mars and Saturn) and evolved stars (e.g. IRC 10216, R-Hya, CRL 2688, CRL 618, NGC 7027, R-CAS and O-Ceti) for all lines except CO(7−6). Planets were the sole pointing sources at 806 GHz. The pointing accuracy is around 5″. The overall calibration accuracy is ≈20%. Data have been reduced using the GILDAS/CLASS data analysis package. The spectra have been smoothed to a velocity resolution of ≈10 km s^{-1}. Gaussian profiles have been fitted to observed spectra (see Figs. 1 to 16), and linear baselines have been subtracted.

4. Data analysis

4.1. Spectra and maps

Spectra of the galaxy nuclei are shown in Figs. 1 to 14. The spectra taken at positions in the spiral arms of M 83 are shown in Fig. 15 while those taken at positions in the NGC 6946 arms are presented in Fig. 16. The observed line is indicated above. Figures 18 and 17 show integrated intensity maps of the ^{12}CO(3−2) (top) and the ^{12}CO(6−5) (bottom) lines towards M 83 and IC 342, respectively.

Tables B.1 and B.2 in Appendix B list the line intensities (A in K km s^{-1} and I in Wm^{-2} sr^{-1}) and the line fluxes (F in Wm^{-2}) resulting from Gaussian fits for the sample galaxies (for each observation, we give the corresponding beam size). I (in Wm^{-2} sr^{-1}) is derived using Eqs. (3) and (4) in Bayet et al. (2004). To compute the flux, F (in Wm^{-2}), we used Eq. (5) in Bayet et al. (2004). The estimated errors on data listed in Tables B.1 and B.2 are also indicated in Col. 5. For most sources, the atomic carbon [CI]($^3P_1-^3P_0$) data have been published by Gerin & Phillips 2000 but they have been analyzed again for consistency. All the CSO observations we obtained for our galaxy sample are summarized in Table B.1 where we list the data for all positions in the nucleus as well as in the spiral arms when it is appropriate.

Table B.2 in the electronic appendix presents central position data for a restricted sample (IC 10, IC 342, M 83, NGC 4038, Overlap and NGC 6946) we have been able to observe extensively (up to the ^{12}CO(6−5) or ^{12}CO(7−6) line). For these sources, we list the available informations in the literature, in the same way as Bayet et al. (2004) did for NGC 253 and Henize 2−10. All CO transitions we used for the modelling work, are identified with an asterisk in Col. 8 of Table B.2.

[1] See web site: `http://www.submm.caltech.edu/cso/`

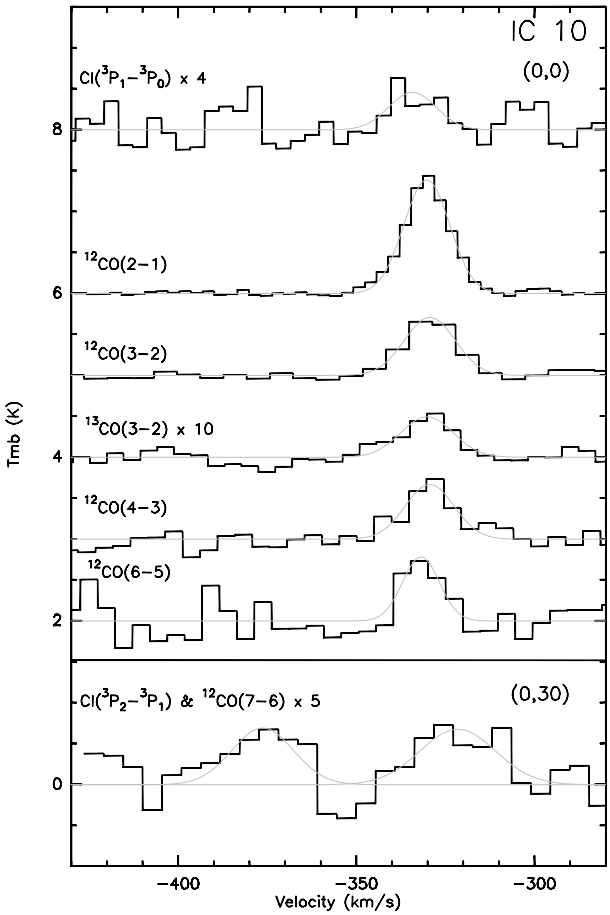

Fig. 1. Observed spectra towards IC 10 nucleus (see Table B.1) except for the [CI]($^3P_2-^3P_1$) and the ^{12}CO(7−6) spectra which correspond to the offset position (0″, 30″). Velocities (horizontal axis) are given in km s^{-1} relative to the LSR (V_{LSR}) and the line intensities (vertical axis) are in units of T_{mb} (K). The grey curves are Gaussian fits. The observed line is written above each spectrum. In this figure, we present the [CI]($^3P_2-^3P_1$) and the ^{12}CO(7−6) lines on the same spectrum since they have been observed simultaneously. The [CI]($^3P_1-^3P_0$) spectrum is from Gerin & Phillips (2000) but it has been analyzed again to obtain an homogeneous dataset of observations.

Moreover, in order to compare at the same spatial resolution different CO line intensities, we have convolved the line intensities to a common (final) beam size of 21.9″, which is the CSO beam size at the frequency of the ^{12}CO(3−2) line. Precisely, to perform this convolution, we multiplied A, I and F by factors depending on the size of each emitting source (see Eqs. (A.1) to (A.4) in Appendix A), the initial (observed) beam size and the final beam size (21.9″). To determine the source sizes, we used high spatial resolution maps and fitted Gaussian spatial profile to these maps. The sources may be either axisymmetric ($a \times a$) or elliptical ($a \times b$). Table 2 lists the adopted source sizes and the maps we used for this measurement.

Bayet et al. (2004) used the same method in their study of NGC 253 and Henize 2−10.

4.2. The C and CO cooling rates

We have derived the observed C and CO cooling rates which provide an essential information for the thermal balance of the studied galaxy nuclei. We estimated the observed C and CO cooling rates by summing the intensities (I in Wm^{-2} sr^{-1}) of all

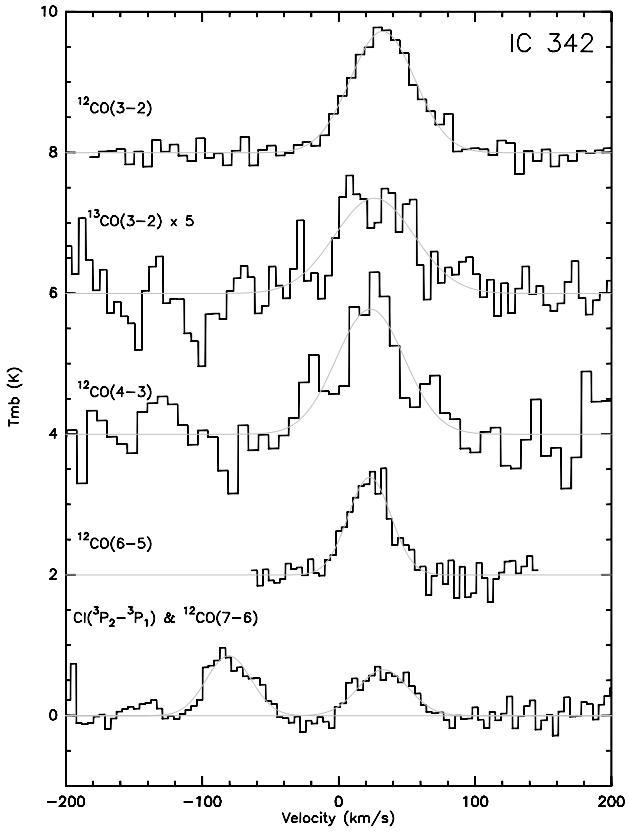

Fig. 2. Observed spectra towards IC 342 nucleus (see Table B.1). See the caption of Fig. 1. We present the [CI](^{3}P$_2$–^{3}P$_1$) and the ^{12}CO(7–6) lines on the same spectrum since they have been observed simultaneously.

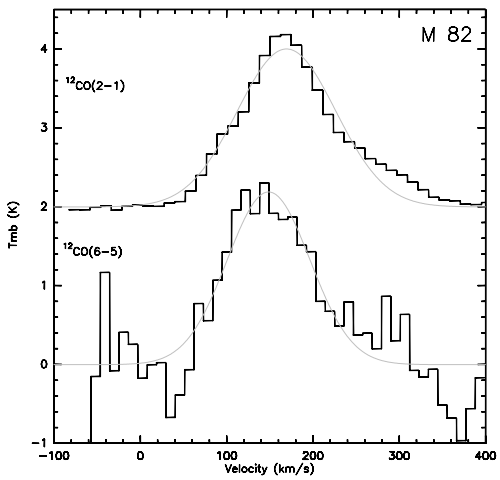

Fig. 3. Observed spectra towards M 82 nucleus (see Table B.1). See the caption of Fig. 1.

CO transitions listed in Table B.2 and identified with an asterisk (both literature data and our dataset). We have computed the observed C and CO cooling rates in the galaxy nuclei for a common beam size of 21.9″. This corresponds to linear scales of 106 pc, 191 pc, 1.5 kpc, 372 pc and 584 pc for the IC 10, IC 342, NGC 4038 (and the Overlap region), M 83 and NGC 6946 nuclei, respectively. The observed cooling rates for C and CO are listed in Table 3 together with the CO cooling rates derived from PDR and LVG models (see Sect. 5.2).

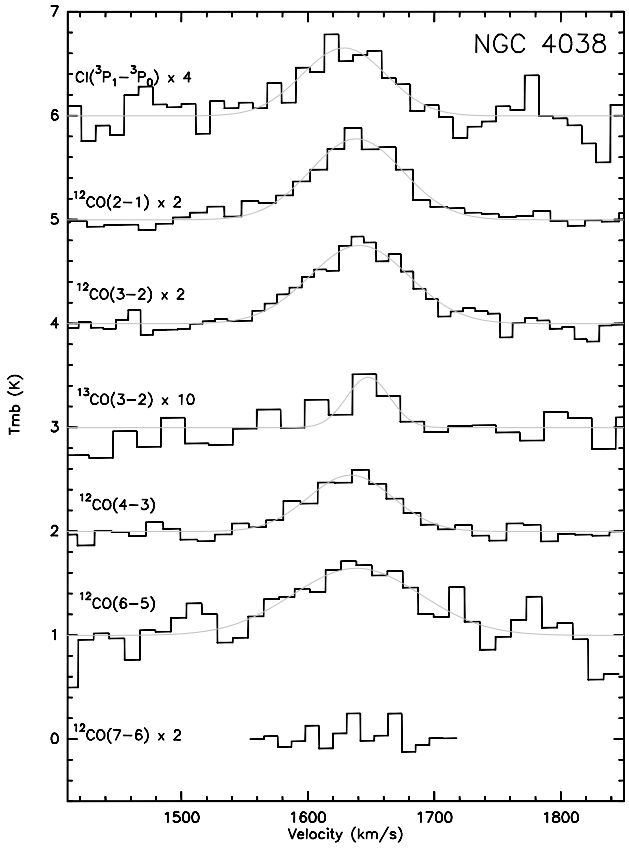

Fig. 6. Observed spectra towards NGC 4038 nucleus (see Table B.1). See the caption of Fig. 1.

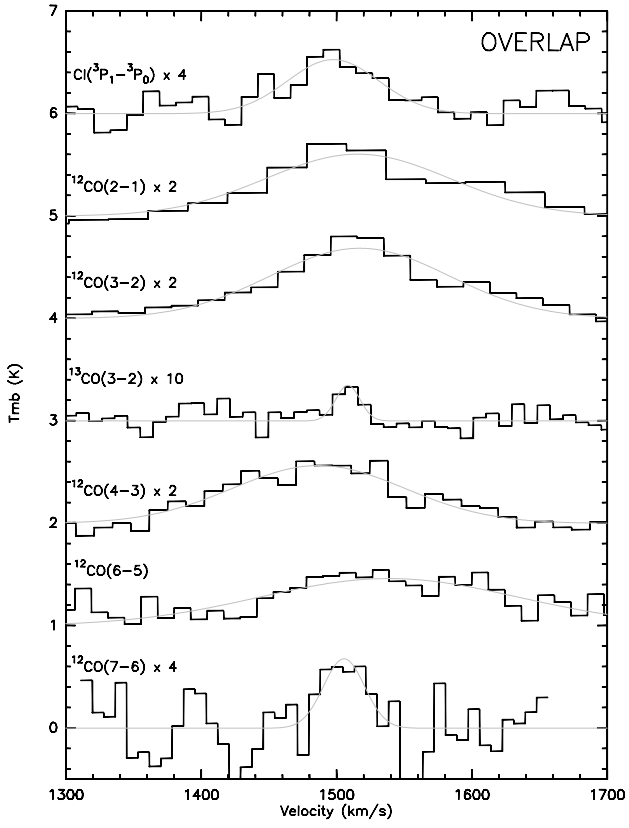

Fig. 7. Observed spectra towards the Overlap region (see Table B.1). See the caption of Fig. 1.

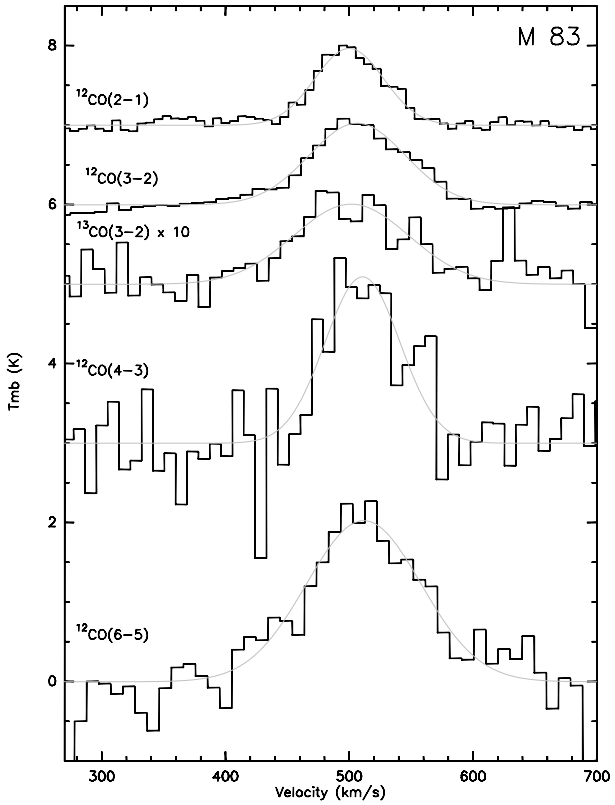

Fig. 12. Observed spectra towards M 83 nucleus (see Table B.1). See the caption of Fig. 1.

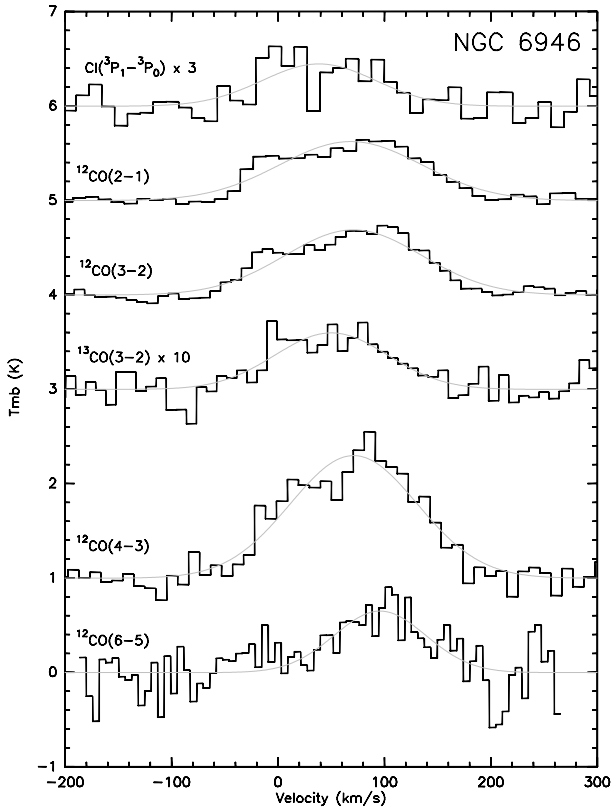

Fig. 14. Observed spectra towards NGC 6946 nucleus (see Table B.1). See the caption of Fig. 1.

For all studied galaxies, the CO lines contributing the most to the observed CO cooling rates are ^{12}CO(6−5) and ^{12}CO(7−6), followed by ^{12}CO(4−3) and ^{12}CO(3−2), with varying relative contributions of those lines in the studied sources. These results confirm that the CO transitions with high-J ($J_{\rm upper} \geqslant 3$) are contributing the most to the total observed CO cooling rate, with the highest contribution for the ^{12}CO(6−5) line in the observed galaxies.

For all targets, it is also noticeable that the observed CO cooling rate is higher than the observed C cooling rate, by a factor of $\lesssim$4.0 for IC 10 and IC 342, of 6.9 and 19.7 for NGC 253 and Henize 2−10, respectively (see Bayet et al. 2004 for these last two sources), of $\gtrsim$20 for NGC 4038, Overlap, M 83 and NGC 6946, respectively. In the NGC 4038, Overlap, M 83 and NGC 6946 nuclei, the line which contributes the most to the C cooling rate ([CI](^{3}P$_2$−^{3}P$_1$), as it is shown in the following) has not been observed yet, but the difference between the C and CO cooling rates is large enough not to modify the dominant role of carbon monoxide for the gas cooling with respect to the atomic carbon.

Similar results have been observed for the distant galaxies J1148+5251 (z = 6.42) and PSS2322+1944 (z = 4.12) (see Cox et al. 2002; Bertoldi et al. 2003; Pety et al. 2004; Walter et al. 2004). The lines which contribute the most to the CO cooling rates are those with $J_{\rm upper} \geqslant 3$. The difference between the C and CO cooling rates seems also to be important (factor of >10) in distant objects.

Because the observed C and CO cooling rates are computed with the observed lines only (see asterisks in Table B.2), unobserved lines (e.g. [CI](^{3}P$_2$−^{3}P$_1$), ^{12}CO(5−4) or ^{12}CO(8−7)) might contribute significantly to the CO or C cooling rates. Therefore, we used models in Sect. 5 to predict the missing line intensities; and also to obtain the physical properties of the warm and dense gas contained in the galaxy nuclei. Table 3 shows that the observed CO cooling rate is ≈70% of the modelled CO cooling rate for galaxies with ^{12}CO(7−6) detections and 25%−50% for galaxies without ^{12}CO(7−6) detections.

5. CO models

5.1. Description of the models

In this section, we used the measured CO line ratios from the line intensities (I and A) to determine the physical conditions of warm and dense molecular gas in galactic nuclei; namely the kinetic temperature (T_k), the gas density (n(H$_2$)), the CO column density divided by the line width (N(CO)/Δv) and the Far UV radiation field ($\chi_{\rm FUV}$). In the first section, we use a LVG radiative transfer model and in Sect. 5.3, we discuss the use of a PDR model. XDR model results applied to AGN nuclei from our sample will be presented in a forthcoming paper.

The radiative transfer models, based on the LVG formalism, have been developed by Goldreich & Kwan (1974); de Jong et al. (1975). The source is modelled as a one component spherical cloud, with uniform kinetic temperature and density. When using both ^{12}CO and ^{13}CO data, there are four main variables in LVG models: the molecular hydrogen density n(H$_2$), the gas kinetic temperature T_K, the CO column density divided by the line width, and the ^{12}CO/^{13}CO abundance ratio. The LVG approximation is used for efficiently solving the radiative transfer equation, when the molecule level populations are not thermalized. LVG models are useful for a first order determination of the gas properties. However, as the medium is assumed to be homogeneous, these models provide an average description of

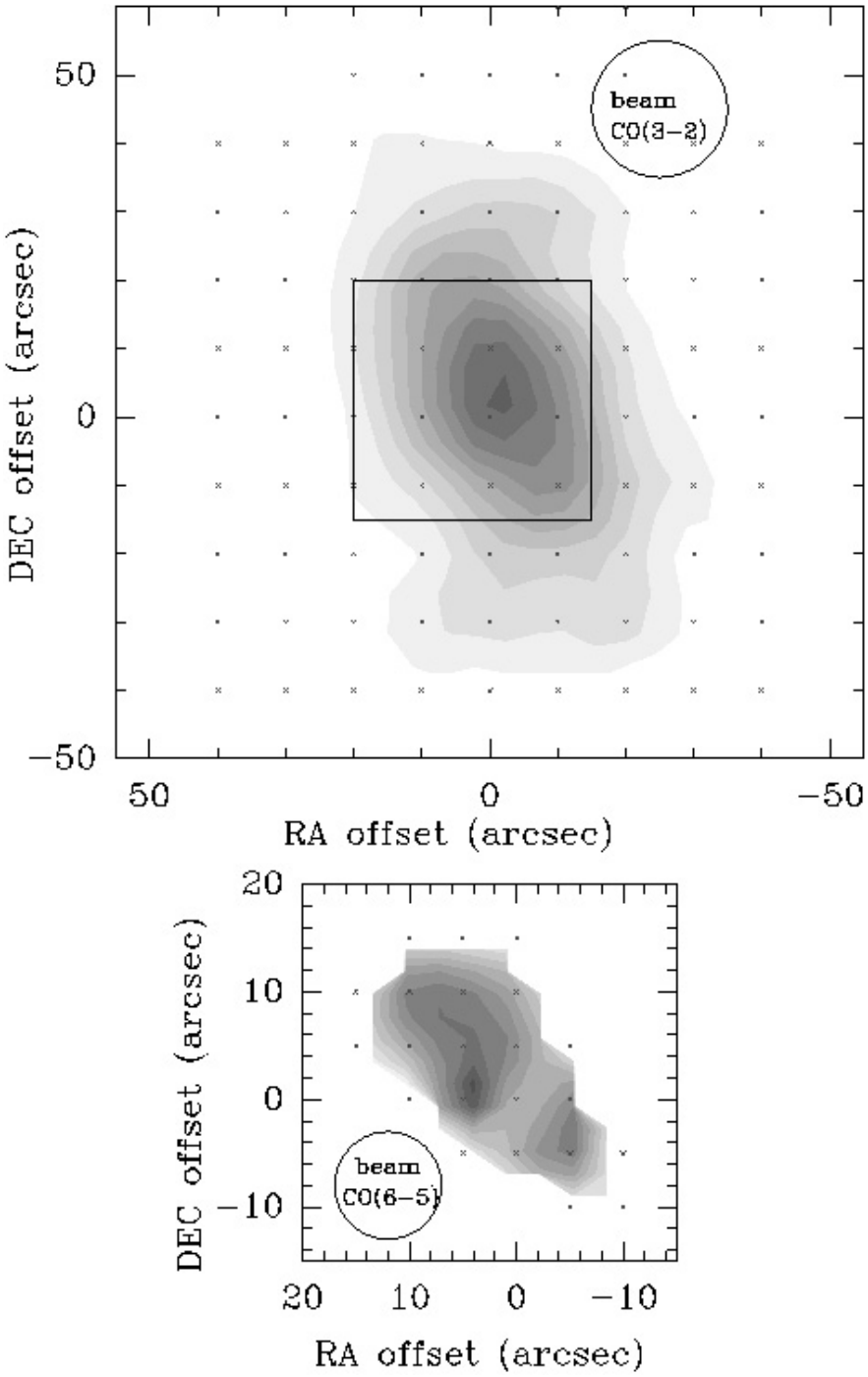

Fig. 17. Map of the velocity integrated intensity of ^{12}CO(3−2) (*top*) and ^{12}CO(6−5) (*bottom*) towards IC 342. The CO emission is integrated over the velocity ranges –200 to 200 km s^{-1} and −50 to 150 km s^{-1}, respectively. For both maps, the crosses show the observed positions. The contours of the ^{12}CO(3−2) map range from $\int T_{\rm mb}{\rm d}v$ = 12 K km s^{-1} to 112 K km s^{-1} with 10 K km s^{-1} steps. For the ^{12}CO(6−5) map, the contours range from $\int T_{\rm mb}{\rm d}v$ = 8 K km s^{-1} to 108 K km s^{-1} with 10 K km s^{-1} steps. The intensity peak value of the ^{12}CO(3−2) map is $\int T_{\rm mb}{\rm d}v \approx$ 110 K km s^{-1}. The intensity peak value of the ^{12}CO(6−5) map is $\int T_{\rm mb}{\rm d}v \approx$ 108 K km s^{-1}. The black box in the upper figure represents the size of the lower figure. The circles indicate the beam sizes at the frequency of the ^{12}CO(3−2) line (*top*) and at the frequency of the ^{12}CO(6−5) line (*bottom*). No pointing error was detected for this map.

the molecular gas, which is known to exhibit structure at smaller spatial scales than sampled by these observations.

Photo-dissociation region (PDR) models are more sophisticated than LVG models as they solve simultaneously for the gas chemistry, photo-dissociation and thermal balance, taking into account the relevant physical and chemical processes. Such models have been developed during the past two decades, for a variety of astrophysical sources, from giant molecular clouds illuminated by the interstellar radiation field to the conditions experienced by circumstellar disks or by dense matter, very close to hot massive stars (Tielens & Hollenbach 1985a,b; Le Bourlot et al. 1993; Koester et al. 1994; Sternberg & Dalgarno 1995; Hollenbach & Tielens 1999; Kaufman et al. 1999). In PDR models, the line emission of the most abundant species, which

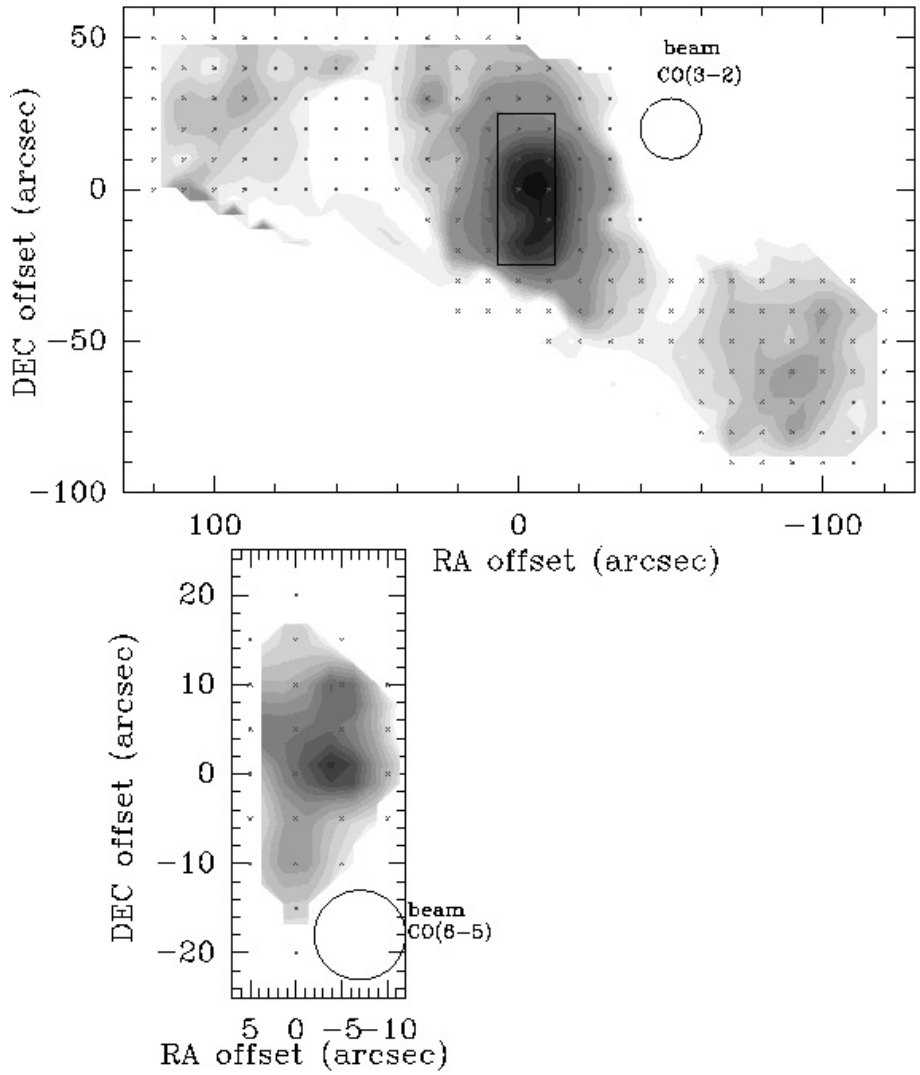

Fig. 18. Map of the velocity integrated intensity of ^{12}CO(3−2) (*top*) and ^{12}CO(6−5) (*bottom*) lines towards M 83. For both maps, the CO emission is integrated over the velocity range 200 to 800 km s^{-1}, and the crosses show the observed positions. The contours of the ^{12}CO(3−2) map range from $\int T_{\rm mb}{\rm d}v$ = 3 K km s^{-1} to 18 K km s^{-1} with 3 K km s^{-1} steps, and from $\int T_{\rm mb}{\rm d}v$ = 21 K km s^{-1} to 102 K km s^{-1} with 10 K km s^{-1} steps. For the ^{12}CO(6−5) map, the contours range from $\int T_{\rm mb}{\rm d}v$ = 20 K km s^{-1} to 320 K km s^{-1} with 25 K km s^{-1} steps. The intensity peak value of the ^{12}CO(3−2) map is $\int T_{\rm mb}{\rm d}v \approx$ 100 K km s^{-1}. The intensity peak value of the ^{12}CO(6−5) map is $\int T_{\rm mb}{\rm d}v \approx$ 318 K km s^{-1}. The ^{12}CO(6−5) map has been shifted by +5″ along the minor axis due to a pointing error The black box in the upper figure represents the size of the lower figure. The circles indicate the beam size at the frequency of the ^{12}CO(3−2) line (*top*) and at the frequency of the ^{12}CO(6−5) line (*bottom*).

Table 2. Source sizes used to convolve the data to 21.9″. For each source, we used maps (specified in Col. 5) to determine the shape of the Gaussian intensity profile (axisymmetric : a × a or elliptical: a × b) and estimate the values of the full widths at half maximum (FWHM).

	FWHM	line (frequency)	Observed beam size	References
IC 10	20.0″ × 20.0″	^{12}CO(4−3) (461 GHz)	14.5″	This work[1]
NGC 253[a]	23.0″ × 11.0″	^{12}CO(6−5) (691 GHz)	10.6″	Bayet et al. (2004)[2]
IC 342	11.0″ × 11.0″	^{12}CO(6−5) (691 GHz)	10.6″	This work[3]
Henize 2−10[a]	13.0″ × 13.0″	^{12}CO(3−2) (345 GHz)	22″	Meier et al. (2001)[4]
NGC 4038	13.2″ × 9.9″	^{12}CO(1−0) (115 GHz)	4.91″ × 3.15″	Wilson et al. (2000)[5]
Overlap	11.0″ × 8.8″	^{12}CO(1−0) (115 GHz)	4.91″ × 3.15″	Wilson et al. (2000)[6]
M 83	12.0″ × 10.6″	^{12}CO(6−5) (691 GHz)	10.6″	This work[7]
NGC 6946	17.0″ × 17.0″	^{12}CO(4−3) (461 GHz)	17″	Nieten et al. (1999)[8]

[a] We include the sources from Bayet et al. (2004). References: [1] The 20″ *FWHM* is in agreement with the size deduced from the CO maps found in Wilson & Reid (1991) or in Bolatto et al. (2000); [2] Bayet et al. (2004) found good agreement with the source size deduced from Peng et al. (1996) map; [3] The 11″ *FWHM* is very similar to the size deduced from the ^{12}CO(4−3) map of Israel & Baas (2003). Eckart et al. (1990) using the IRAM-30 m telescope, obtained a map in the ^{12}CO(2−1) line which shows a source size around 20″. [4] See Bayet et al. (2004); [5] OVRO map; [6] Overlap corresponds to SGMC 4-5 in this OVRO map; [7] Lundgren et al. (2004) considered the M 83 nucleus as a 12″ axisymmetric source which agrees with our value; [8] The ^{12}CO(1−0) map published by Weliachew et al. (1988), is consistent with a 15″ source size.

Table 3. Parameters of the "best fit" LVG and PDR models for IC 10, IC 342, NGC 4038, Overlap, M 83 and NGC 6946. For each galaxy, the same abundance ratio $\frac{^{12}C}{^{13}C}{}^{b}$ and the same Δv^a are used for constraining both LVG and PDR models. To compare observations and predictions deduced from models, the observed CO (^{12}CO and ^{13}CO) and the observed C cooling rates are listed at the bottom.

	IC 10	IC 342	NGC 4038	Overlap	M 83	NGC 6946
$\frac{^{12}C}{^{13}C}{}^{b}$	40	40	40	40	40	40
Δv^a (km s^{-1})	15	54	92	155	91	158
LVG MODELS						
$N(^{12}CO)/\Delta v^a$ (cm^{-2}/km s^{-1})	3.0×10^{16}	3.5×10^{17}	3.2×10^{16}	2.4×10^{16}	6.0×10^{16}	7.0×10^{16}
$n(H_2)$ (cm^{-3})	7.0×10^{5}	1.9×10^{3}	3.5×10^{5}	8.0×10^{3}	6.5×10^{5}	1.5×10^{3}
T_K (K)	25	40	40	145	40	130
$FF_{LVG}{}^{c}$	4.6×10^{-2}	6.7×10^{-2}	1.7×10^{-2}	1.3×10^{-2}	3.6×10^{-2}	2.7×10^{-2}
LVG Predicted ^{12}CO cooling (Wm^{-2} sr^{-1})	5.7×10^{-9}	3.7×10^{-8}	4.1×10^{-8}	4.3×10^{-8}	1.3×10^{-7}	4.8×10^{-8}
LVG Predicted ^{13}CO cooling (Wm^{-2} sr^{-1})	2.2×10^{-10}	1.9×10^{-9}	1.0×10^{-9}	7.4×10^{-10}	4.1×10^{-9}	1.0×10^{-9}
PDR MODELS						
FUV radiation χ_{FUV} ($\times G_0$)	5.5×10^{4}	8.5×10^{3}	2.5×10^{5}	1.5×10^{5}	5.5×10^{4}	1.5×10^{5}
n(H) (cm^{-3})	2.0×10^{5}	1.5×10^{5}	3.0×10^{5}	3.5×10^{5}	5.0×10^{5}	1.0×10^{5}
$FF_{PDR}{}^{c}$	1.3×10^{-2}	2.9×10^{-2}	9.4×10^{-1}	9.2×10^{-1}	1.2×10^{-2}	2.9×10^{-2}
PDR Predicted ^{12}CO cooling (Wm^{-2} sr^{-1})	5.8×10^{-9}	3.6×10^{-8}	3.9×10^{-8}	4.9×10^{-8}	1.2×10^{-7}	4.6×10^{-8}
PDR Predicted ^{13}CO cooling (Wm^{-2} sr^{-1})	3.1×10^{-10}	3.2×10^{-9}	1.2×10^{-9}	1.8×10^{-9}	5.1×10^{-9}	2.1×10^{-9}
PDR Predicted C cooling (Wm^{-2} sr^{-1})	4.5×10^{-9}	2.8×10^{-8}	2.9×10^{-8}	2.6×10^{-8}	3.7×10^{-8}	8.7×10^{-8}
Observations^{e}						
Observed ^{12}CO cooling (Wm^{-2} sr^{-1})	4.0×10^{-9}	2.5×10^{-8}	1.7×10^{-8}	1.9×10^{-8}	4.3×10^{-8}	2.7×10^{-8}
Observed ^{13}CO cooling (Wm^{-2} sr^{-1})	5.7×10^{-11}	9.0×10^{-10}	9.9×10^{-11}	1.2×10^{-10}	4.2×10^{-10}	3.9×10^{-10}
Observed C cooling (Wm^{-2} sr^{-1})	1.1×10^{-9}	6.4×10^{-9}	9.2×10^{-10d}	7.1×10^{-10d}	2.3×10^{-9d}	1.4×10^{-9d}

[a] Deduced from Gaussian fits to the ^{12}CO(3−2) line profiles. [b] Assumed $\frac{^{12}C}{^{13}C}$. [c] FF is the filling factor of the CO emitting region in the 21.9″ beam. [d] Based on the sole C($^3P_1$−$^3P_0$) transition. [e] See C and CO lines identified with an asterisk in Table B.2.

determine the gas cooling rate, is usually calculated under the LVG approximation. Because of the many physical and chemical processes involved, PDR models use a simple geometry for the modelled cloud, which can be either plane parallel or spherical. When applied to CO line emission, PDR model predictions correspond to the integral along the line of sight of the contributions of the different regions in the modelled, plane parallel, cloud, with pronounced kinetic temperature and abundance variations from the warm outer shells to the cold interior. Therefore, the contributions of these different regions to the CO emission depends on the rotational line, the high-J CO lines being more sensitive to the warm gas (≳20 K), while the CO(1−0) contribution is biased to the cold gas (<20 K).

We have chosen to use both types of models as they are built with different hypotheses and therefore provide different information when the model outputs are compared with CO observations. As LVG models are simple and fast, they are largely used in the analysis of extragalactic CO data. But LVG models are obviously a crude approximation to the complex mixture of physical conditions in galaxy nuclei. Although solving the radiative transfer under the same LVG approximation, PDR models consider kinetic temperature and CO abundance gradients along the line of sight. By comparing the PDR and LVG model predictions for the same source, we gain some insight on the quality of the models, especially on the reliability of the predictions for the missing CO lines, and on the computation of the CO cooling rate.

5.2. LVG models

5.2.1. Fitting procedures

We have shown in Bayet et al. (2004) (Fig. 1) that the CO lines with $J_{upper} \geqslant 3$ provide a good signature of the warm molecular gas ($T_k \gtrsim 20$ K). In this paper, we used the same method, and

Table 4. Observed and predicted ("best" LVG model) line ratios for the studied sources.

A (K km s^{-1})	IC 10 obs.*	IC 342 obs.*	A (K km s^{-1})	NGC 4038 obs.*	Overlap obs.*	A (K km s^{-1})	M 83 obs.*	NGC 6946 obs.*
$\frac{^{12}CO(3-2)}{^{12}CO(4-3)}$	1.8 ± 0.3^a	2.2 ± 0.3^a	$\frac{^{12}CO(3-2)}{^{12}CO(4-3)}$	1.5 ± 0.2	2.4 ± 0.3	$\frac{^{12}CO(3-2)}{^{12}CO(4-3)}$	1.1 ± 0.4^a	1.5 ± 0.3^a
$\frac{^{12}CO(3-2)}{^{12}CO(6-5)}$	2.5 ± 0.5^a	4.1 ± 0.4^a	$\frac{^{12}CO(3-2)}{^{12}CO(6-5)}$	1.1 ± 0.2^a	1.7 ± 0.8^a	$\frac{^{12}CO(3-2)}{^{12}CO(6-5)}$	1.2 ± 0.3^a	4.6 ± 1.0^a
$\frac{^{12}CO(3-2)}{^{12}CO(7-6)}$	8.7 ± 2.4^a	15.0 ± 1.6^a	–	–	–	–	-	-
$\frac{^{12}CO(2-1)}{^{12}CO(7-6)}$	10.8 ± 4.6^a	18.5 ± 5.3^a	$\frac{^{12}CO(2-1)}{^{12}CO(6-5)}$	1.6 ± 0.5^a	2.2 ± 1.3^a	$\frac{^{12}CO(2-1)}{^{12}CO(6-5)}$	1.4 ± 0.1^a	6.9 ± 1.6^a
$\frac{^{12}CO(3-2)}{^{13}CO(3-2)}$	10.3 ± 2.1^a	5.5 ± 0.7^a	$\frac{^{12}CO(3-2)}{^{13}CO(3-2)}$	18.0 ± 11.0^a	$30.2 \pm 8.2^{a,b}$	$\frac{^{12}CO(3-2)}{^{13}CO(3-2)}$	8.5 ± 2.6^a	17.1 ± 2.0^a
$\frac{^{12}CO(1-0)}{^{13}CO(1-0)}$	–	11.3 ± 0.4	$\frac{^{12}CO(1-0)}{^{13}CO(1-0)}$	–	–	$\frac{^{12}CO(1-0)}{^{13}CO(1-0)}$	–	11.1 ± 4.4
$\frac{^{12}CO(2-1)}{^{13}CO(2-1)}$	15.4 ± 6.2	10.9 ± 2.6	$\frac{^{12}CO(2-1)}{^{13}CO(2-1)}$	24.3 ± 9.7	16.3 ± 6.6	$\frac{^{12}CO(2-1)}{^{13}CO(2-1)}$	4.5 ± 0.5	29.7 ± 6.7
	LVG model $T_K = 25$ K	LVG model $T_K = 40$ K		LVG model $T_K = 40$ K	LVG model $T_K = 145$ K		LVG model $T_K = 40$ K	LVG model $T_K = 130$ K
$\frac{^{12}CO(3-2)}{^{12}CO(4-3)}$	1.2	1.3	$\frac{^{12}CO(3-2)}{^{12}CO(4-3)}$	1.1	1.1	$\frac{^{12}CO(3-2)}{^{12}CO(4-3)}$	1.1	1.4
$\frac{^{12}CO(3-2)}{^{12}CO(6-5)}$	2.8	4.1	$\frac{^{12}CO(3-2)}{^{12}CO(6-5)}$	1.6	2.7	$\frac{^{12}CO(3-2)}{^{12}CO(6-5)}$	1.4	5.1
$\frac{^{12}CO(3-2)}{^{12}CO(7-6)}$	8.4	15.6	$\frac{^{12}CO(3-2)}{^{12}CO(7-6)}$	2.7	5.9	$\frac{^{12}CO(3-2)}{^{12}CO(7-6)}$	1.9	13.9
$\frac{^{12}CO(2-1)}{^{12}CO(7-6)}$	9.1	17.9	$\frac{^{12}CO(2-1)}{^{12}CO(6-5)}$	1.5	2.3	$\frac{^{12}CO(2-1)}{^{12}CO(6-5)}$	1.4	6.1
$\frac{^{12}CO(3-2)}{^{13}CO(3-2)}$	11.6	5.4	$\frac{^{12}CO(3-2)}{^{13}CO(3-2)}$	16.7	23.9	$\frac{^{12}CO(3-2)}{^{13}CO(3-2)}$	10.1	17.1
$\frac{^{12}CO(1-0)}{^{13}CO(1-0)}$	27.3	4.2	$\frac{^{12}CO(1-0)}{^{13}CO(1-0)}$	33.7	36.8	$\frac{^{12}CO(1-0)}{^{13}CO(1-0)}$	28.6	18.6
$\frac{^{12}CO(2-1)}{^{13}CO(2-1)}$	14.4	3.5	$\frac{^{12}CO(2-1)}{^{13}CO(2-1)}$	22.3	27.9	$\frac{^{12}CO(2-1)}{^{13}CO(2-1)}$	14.8	12.7

* Ratio derived from observations marked with asterisks in Table B.2; [a] values used as constraints for the LVG models; [b] value from Table 2 in Zhu et al. (2003).

constrain the fits of LVG or PDR models by the line intensity ratios from the observed CO submillimeter lines.

More precisely, for IC 10 and IC 342, we used the following line intensity ratios (see Table 4): $\frac{^{12}CO(3-2)}{^{12}CO(4-3)}$, $\frac{^{12}CO(3-2)}{^{12}CO(6-5)}$, $\frac{^{12}CO(3-2)}{^{12}CO(7-6)}$, $\frac{^{12}CO(2-1)}{^{12}CO(7-6)}$ and $\frac{^{12}CO(3-2)}{^{13}CO(3-2)}$. Some observations of NGC 4038 and Overlap suffer from large error bars. Indeed, the ^{12}CO(4−3) and the ^{12}CO(7−6) lines have a lower signal-to-noise ratio than other transitions (see Figs. 23 and 22 where these lines appear clearly too faint). Therefore, we chose for those sources the following ratios to constrain the models: $\frac{^{12}CO(3-2)}{^{12}CO(6-5)}$, $\frac{^{12}CO(2-1)}{^{12}CO(6-5)}$ and $\frac{^{12}CO(3-2)}{^{13}CO(3-2)}$ (see Table 4). Since we missed the ^{12}CO(7−6) line for M 83 and NGC 6946, we used the following line intensity ratios: $\frac{^{12}CO(3-2)}{^{12}CO(4-3)}$, $\frac{^{12}CO(3-2)}{^{12}CO(6-5)}$, $\frac{^{12}CO(2-1)}{^{12}CO(6-5)}$ and $\frac{^{12}CO(3-2)}{^{13}CO(3-2)}$ (see Table 4).

To compute these line intensity ratios, we used data identified with an asterisk in Table B.2 (precisely, in the Col. 5: the line area, A, in K km s^{-1}) which have been previously scaled to a common beam size of 21.9″ (see Sect. 4.1). Values of line intensity ratios are listed in Table 4. The ^{13}CO data are particularly useful for measuring the CO column densities while the ^{12}CO data provide constraints on the kinetic temperature and the H_2 density. The ^{12}CO and ^{13}CO spectra used are displayed in Figs. 1 to 14 (see Sect. 4.1).

We made use of a least square fitting method (taking into account the errors of the observed intensity line ratios) to determine the physical conditions which reproduce the observations the best. The line width Δv and the $\frac{^{12}CO}{^{13}CO}$ abundance ratio (X_{galaxy} in Bayet et al. 2004), are not part of the fitting process. Δv is set to the value deduced from Gaussian fits of the ^{12}CO(3−2) spectra (FWHM). The Δv values used for the target galaxies are reported in Table 3. The $\frac{^{12}CO}{^{13}CO}$ abundance ratio is set to 40 (see Table 3) for IC 10, IC 342, NGC 4038, Overlap, M 83 and NGC 6946, the value used in previous LVG modelling works on the same galaxies (for IC 342 in Mauersberger & Henkel 1993; Henkel et al. 1998; for NGC 4038 in Zhu et al. 2003, for M 83 in Mauersberger & Henkel 1993 and for NGC 6946, in Israel & Baas 2001). But for IC 10, Petitpas & Wilson (1998a) used a $\frac{^{12}CO}{^{13}CO}$ abundance ratio of 50 and for Overlap, Zhu et al. (2003) used two different abundance ratios (40 and 60).

5.2.2. Results

For these six sources, we varied $N(^{12}CO)$ from 1.0×10^{16} cm^{-2} to 1.0×10^{20} cm^{-2}, T_K from 10 K to 255 K and $n(H_2)$ from 10 cm^{-3} to 10^7 cm^{-3}. Model solutions (physical parameters which reproduce the observations the best) for each source are given in Table 3. As an example of the used fitting process, we present in Fig. 19 results of the LVG model calculations for NGC 4038 (right side) and M 83 (left side). In this figure, we plot $\Delta\chi^2$ ($\chi^2 - \chi^2_{min}$) contours in the 2D parameter space ($n(H_2)$(cm^{-3}) vs. T_K(K)). In this figure, the parameter $N(^{12}CO)/\Delta v$ has been set to its "best fit" value. More precisely, in Fig. 19, we have selected all LVG model solutions within a small interval in $N(^{12}CO)/\Delta v$ centered around the best $N(^{12}CO)/\Delta v$ value (see the chosen interval values at the top of each plot) for a better gridding of the ($n(H_2)$, T_K) parameter space. Similar plots were obtained for each target. The "best fit" model (with χ^2_{min}), is located at the intersection of the two black lines in Fig. 19. Predicted line intensity ratios from the best fit models are listed in Table 4. In Fig. 19 the best models are located in the black zones which have a "banana" shape in the ($n(H_2)$, T_K) plane. It is clear that the fitting

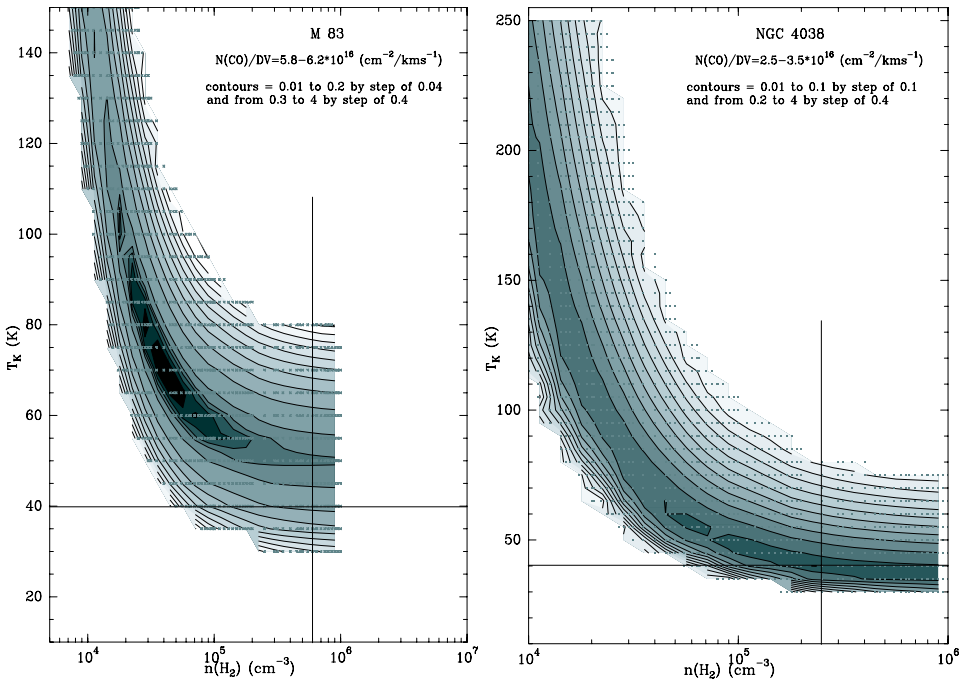

Fig. 19. LVG model results for NGC 4038 (*right side*) and M 83 (*left side*). For each source, the "best" fit $N(^{12}\mathrm{CO})/\Delta v$ (indicated at the top) is found by minimizing χ^2. In fact, to avoid gridding problems, we use all models within a small interval centered around the best $N(^{12}\mathrm{CO})/\Delta v$ value, listed in Table 3. We plot $\Delta\chi^2$ contours in the T_K (K) vs. $n(\mathrm{H_2})(\mathrm{cm}^{-3})$ space. The contour levels for M 83 and for NGC 4038 are indicated in the plots. The LVG models with higher $\Delta\chi^2$ (>4) are not represented. In both figures, the dark areas represent the zones where χ^2 is the lowest. Each cross corresponds to a LVG model solution. The best fit is located at the intersection of the two black lines.

process using the LVG framework is highly degenerated since acceptable fits (black zones) can be obtained over a large domain of the parameter space. For NGC 4038, we conclude that the gas density is not well constrained while the temperature range is reasonably narrow. For M 83, we have the reverse case: the gas density is well constrained while the temperature range is broad. We notice that, despite the degeneracy, predicted CO line intensities computed from models located in the black areas in Figs. 19 do not differ significantly (variations in line intensity between models localized in the black areas are $\lesssim$3%). Therefore, LVG predictions are relevant for computing the CO cooling rate. In Figs. 20−25, we present the best LVG models for the studied sources (IC 10, IC 342, NGC 4038, Overlap, M 83 and NGC 6946). For each source, we list the physical parameters corresponding to the best solutions in Table 3. Comparisons between observed and modelled line intensity ratios are given in Table 4.

The LVG models have been used for predicting ^{12}CO line intensities from ^{12}CO(1−0) up to ^{12}CO(15−14) and the ^{13}CO line intensities from ^{13}CO(1−0) up to ^{13}CO(6−5). The predicted ^{12}CO and the ^{13}CO cooling rates are computed by summing all ^{12}CO and ^{13}CO line intensities and are listed in Table 3. We obtained the following results:

- The "best" model for IC 10 is illustrated with grey triangles in Fig. 20. The lines which contribute the most to the ^{12}CO and to the ^{13}CO cooling rates are the ^{12}CO(5−4) line (26.6% of the total intensity), the ^{12}CO(6−5) line (25.1%) and the ^{12}CO(4−3) line (17.9%), the ^{13}CO(4−3) line (30.0%), the ^{13}CO(5−4) line (29.5%) and the ^{12}CO(6−5) line (18.3%), respectively.
- The "best" model for IC 342 is illustrated with grey triangles in Fig. 21. The lines which contribute the most to the ^{12}CO cooling rate are ^{12}CO(5−4) (28.1% of the total intensity), ^{12}CO(6−5) (22.2%) and ^{12}CO(4−3) (21.7%) while the lines which dominate the ^{13}CO cooling rate are ^{13}CO(3−2) (36.3%), ^{13}CO(4−3) (27.7%) and ^{13}CO(2−1) (19.2%).
- For NGC 4038, we obtained a "best" model represented in Fig. 22 with grey triangles. The lines which contribute the most to the ^{12}CO cooling rate are ^{12}CO(6−5) line (22.8%), the ^{12}CO(7−6) line (21.16%) and the ^{12}CO(5−4) line (17.4%) while the main lines of the ^{13}CO cooling rate are the ^{13}CO(5−4) (33.0%), ^{13}CO(6−5) (32.3%) and the ^{13}CO(4−3) (22.9%) lines.
- For Overlap, we obtained a "best" model represented in Fig. 23 with grey triangles. The ^{12}CO(6−5) line represents 21.2% of the ^{12}CO cooling rate while the ^{12}CO(5−4) and the ^{12}CO(7−6) lines correspond to 21.0% and 15.7%, respectively. The main lines for the ^{13}CO cooling are the ^{13}CO(5−4) (29.9%), ^{13}CO(4−3) (28.3%) and the ^{13}CO(6−5) (22.9%) lines.
- For M 83, the "best" model is represented in Fig. 24 with grey triangles. The ^{12}CO(7−6) line represents 22.7% of the ^{12}CO cooling rate while the ^{12}CO(6−5) and the ^{12}CO(8−7) lines correspond to 19.4% and 18.4%, respectively. The ^{12}CO cooling rate deduced from this "best" model is less accurate than for the previous galaxies since we constrained LVG models without the ^{12}CO(7−6) line. The ^{13}CO cooling rate is dominated by the intensities of the ^{13}CO(6−5) (34.0%), ^{13}CO(5−4) (32.8%) and the ^{13}CO(4−3) (22.0%) lines.
- For NGC 6946, we obtained a "best" model represented in Fig. 25 with grey triangles. The main lines for the ^{12}CO cooling rate are the ^{12}CO(5−4) (23.6%), the ^{12}CO(4−3) (20.3%) and the ^{12}CO(6−5) (18.9%) lines. The ^{12}CO cooling rate deduced from this "best" model is less accurate than for the previous galaxies since we constrained LVG models

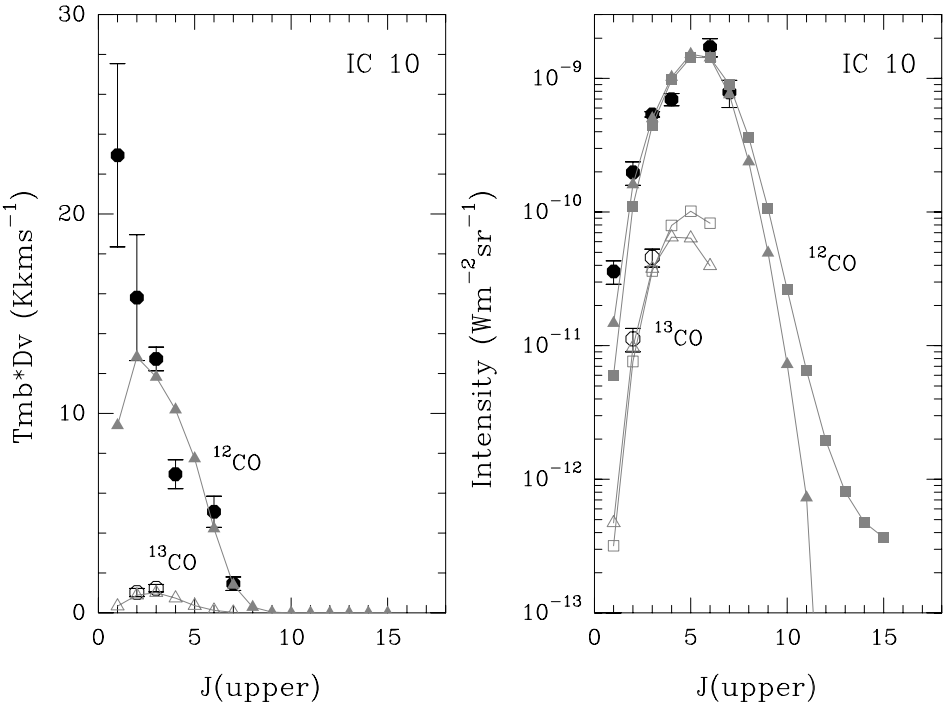

Fig. 20. "best" LVG and PDR models compared with observations for IC 10 (see Table 3 for the model parameters). On the left side, we plot integrated intensities in K km s^{-1} vs. $J_{\rm upper}$. On the right side, we plot I in Wm^{-2} sr^{-1} vs. $J_{\rm upper}$. In all figures, grey triangles represent the LVG model while the grey squares represent results from the PDR model (see Sect. 5.3). Observations (with error bars) taken from the literature and from our data set are shown in black. The ^{13}CO transitions are represented with open symbols while the ^{12}CO transitions use filled symbols.

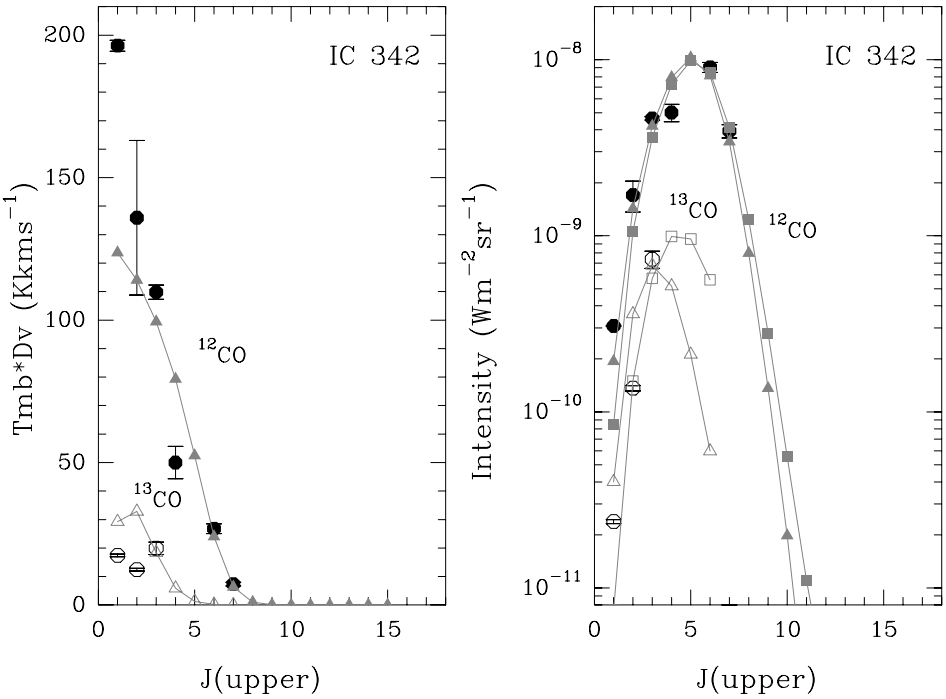

Fig. 21. "best"LVG and PDR models compared with observations for IC 342 (see Table 3 for the model parameters). See caption of Fig. 20.

without the ^{12}CO(7−6) line. The ^{13}CO cooling rate is dominated by the intensities of the ^{13}CO(3−2) (28.8%), ^{13}CO(4−3) (27.5%) and the ^{13}CO(5−4) (18.4%) lines.

We present in Figs. 20−25, the predicted integrated areas (A in K km s^{-1}) and the predicted line intensities (I in Wm^{-2} sr^{-1}) for all ^{12}CO transitions up to J = 15−14 and for all ^{13}CO transitions up to ^{13}CO(6−5). We have computed the predicted integrated areas, A, using the predicted antenna temperature from the models and multiplying it by the line width Δv and by the surface filling factor, FF$_{\rm LVG}$ (both listed in Table 3). For each observed CO line, we have estimated the surface filling factor (FF$_{\rm LVG}$) of molecular clouds in the 21.9″ beam using the ratio $A_{\rm observations}$ (K km s^{-1})/$A_{\rm model}$ (K km s^{-1}). We have made an average, weighted by the S/N, for the filling factors pertaining to each observed transition. For NGC 4038 and Overlap, we have not taken into account the ^{12}CO(4−3) and the

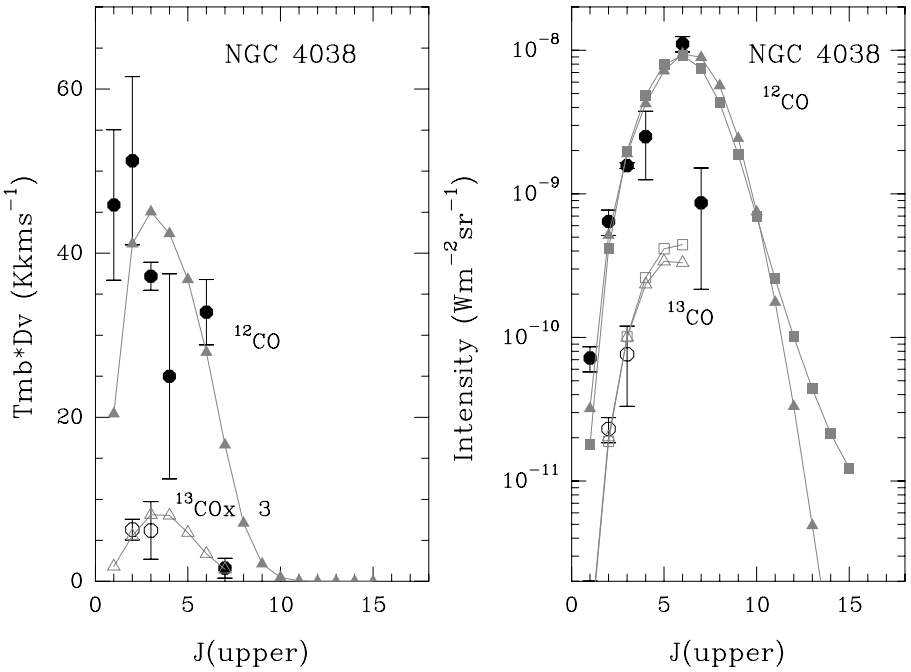

Fig. 22. "best" LVG and PDR models compared with observations for NGC 4038 (see Table 3 for the model parameters). See caption of Fig. 20.

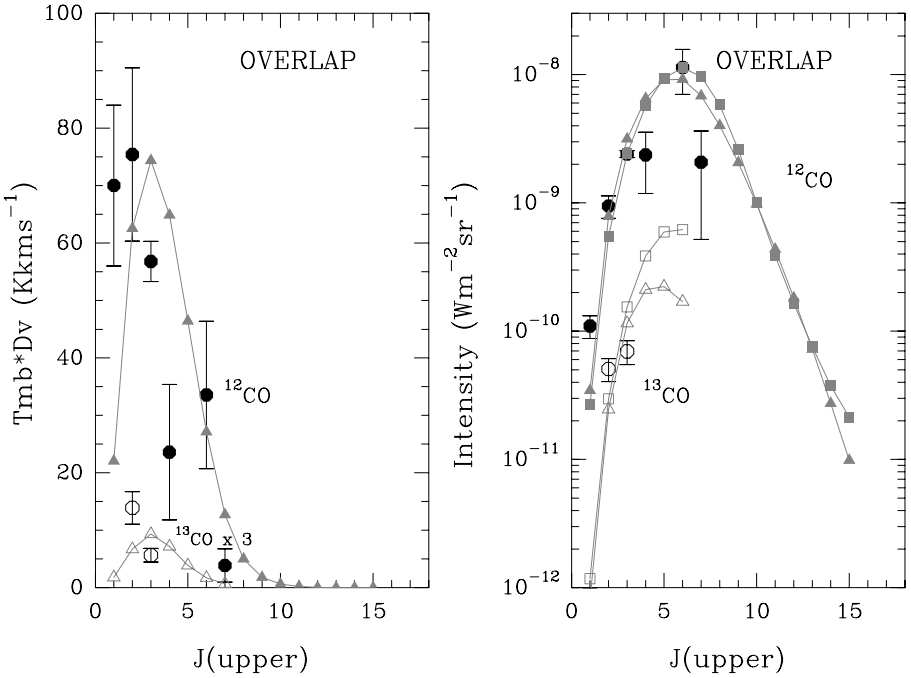

Fig. 23. "best" LVG and PDR models compared with observations for Overlap (see Table 3 for the model parameters). See caption of Fig. 20.

^{12}CO(7−6) lines because they have the lowest signal-to-noise ratio (see Figs. 22 and 23). For the studied sources, we have obtained surface filling factor of a few % (1.3 to 6.7%) in a 21.9″ beam size.

5.2.3. Discussion

From the above analysis we can conclude that LVG models can be confidently used to determine the CO cooling rates, provided that a sufficiently complete data set is available. Even though several points in the parameter space with different physical conditions fit the observed data equally well, the derived CO cooling rates are very similar in all studied cases. The key point is the combination of ^{12}CO(6−5) and ^{12}CO(7−6) data as these two lines provide the largest contribution to the observed ^{12}CO cooling. It will be particularly interesting to observe the ^{12}CO(5−4) line which is shown to be also a main cooling line in these galaxies. In addition to the ^{12}CO(5−4), ^{12}CO(6−5) and ^{12}CO(7−6) lines, data for ^{12}CO(8−7) and ^{12}CO(9−8) lines would be most useful to discriminate models, and for a more accurate determination of the ^{12}CO cooling rates. We also showed that ^{12}CO lines with $J_{\rm upper} \geqslant 10$ are predicted to be weak and will not have significant antenna temperatures (see Figs. 20−25, plots on the left side). In addition ^{13}CO(6−5) data would also be extremely useful for constraining the models, for better estimating the ^{13}CO cooling rates and for measuring the opacity of ^{12}CO(6−5)

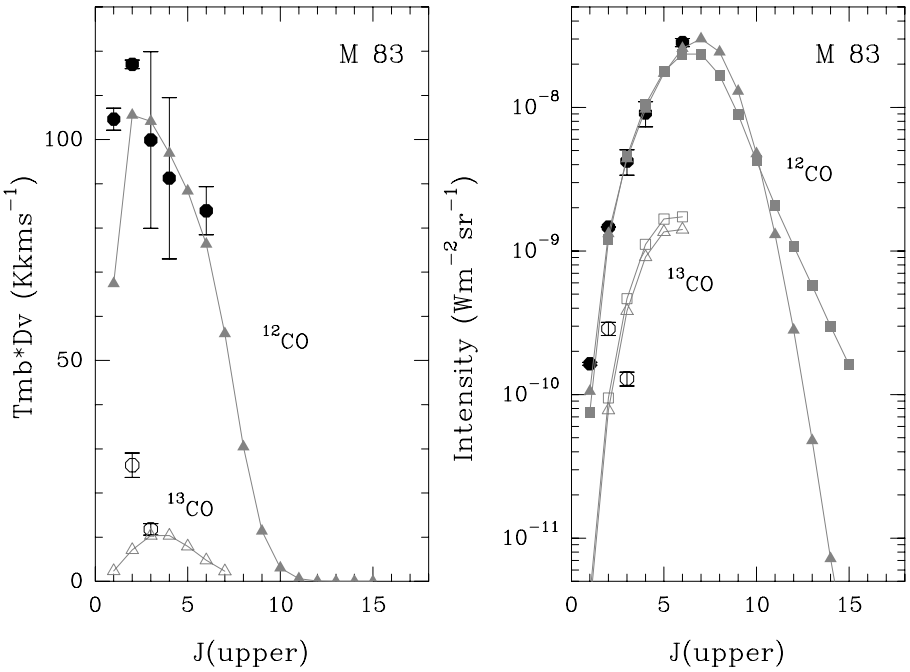

Fig. 24. "best" LVG and PDR models compared with observations for M 83 (see Table 3 for the model parameters). See caption of Fig. 20.

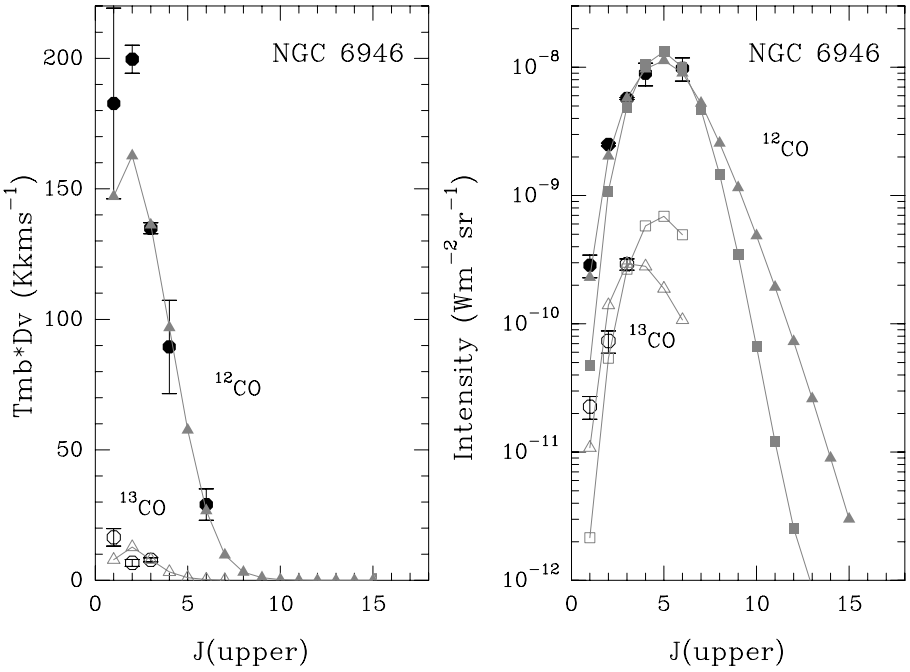

Fig. 25. "best" LVG and PDR models compared with observations for NGC 6946 (see Table 3 for the model parameters). See caption of Fig. 20.

line. Indeed, when comparing the predicted and observed intensities of the ^{13}CO lines, the importance of high-J ^{13}CO lines shows up. For the studied galaxies, ^{13}CO(3−2) is the most intense observed line (see this work and Bayet et al. 2004). For most sources, predicted ^{13}CO(6−5) line intensities are at least as strong as ^{13}CO(3−2) intensities.

Because the LVG models have been constrained by the high-J CO line intensity ratios, intensities of the low-J CO transitions are not well fitted (see for instance the ^{12}CO(1−0) or the ^{12}CO(2−1) predicted intensities in Figs. 20−22 and 25). To relieve that problem, a two component LVG model would be needed, one component fitting the low-J CO transitions and another one for the high-J CO transitions. It was not our purpose here but Harrison et al. (1999); Bradford et al. (2003) did it for the galaxy NGC 253.

We have compared the physical parameters (see Table 3) corresponding to our best fit LVG models with results obtained in previous studies for the same galaxies. For IC 10, Petitpas & Wilson (1998a) presented an acceptable LVG solution: $N(^{12}\mathrm{CO})/\Delta v = 5.0 \times 10^{17}$ cm^{-2}/km s^{-1}, $n(\mathrm{H_2}) = 10^4$−10^5 cm^{-3} and $T_K = 100$ K. We suggest a higher value for the gas density and lower values for $N(^{12}\mathrm{CO})/\Delta v = 3 \times 10^{16}$ cm^{-2}/km s^{-1} and $T_K = 25$ K than those proposed by Petitpas & Wilson (1998a). The differences can be explained

by the fact that we do not use the same set of CO line intensity ratios: Petitpas & Wilson (1998a) used line ratios combining low-J CO lines (^{12}CO(2−1), ^{13}CO(2−1), ^{12}CO(3−2) and ^{13}CO(3−2)) while we used a larger number of intensity ratios focussed on the high-J CO lines (see Table 4). For IC 342, Israel & Baas (2003) fit their data using a LVG model with $N(^{12}\mathrm{CO})/\Delta v = 6{-}10 \times 10^{16}$ cm^{-2}/km s^{-1}, $T_K = 100{-}150$ K and $n(\mathrm{H_2}) = 3.0 \times 10^3$ cm^{-3}. Eckart et al. (1990) suggested a model with $N(^{12}\mathrm{CO}) = 3{-}4 \times 10^{18}$ cm^{-2}, $T_K > 20$ K and a density around $n(\mathrm{H_2}) \approx 2.0 \times 10^3$ cm^{-3} for the center of IC 342. Meier et al. (2000) deduced from their observations a beam-averaged density of $n(\mathrm{H_2}) = 1.3 \times 10^3$ cm^{-3}. Our model agrees very well with the gas density values proposed in the two latter articles. The fitted $N(^{12}\mathrm{CO})/\Delta v$ value is intermediate between results of Israel & Baas (2003) and Eckart et al. (1990). For T_K, we agree better with the value proposed by Eckart et al. (1990) than with the one proposed by Israel & Baas (2003). For NGC 4038, Zhu et al. (2003) proposed a one component model ($N(^{12}\mathrm{CO})/\Delta v = 3.4 \times 10^{16}$ cm^{-2}/km s^{-1}, $n(\mathrm{H_2}) = 1{-}4{\times}10^3$ cm^{-3} and $T_K = 43$ K) in good agreement with our study except for the $n(\mathrm{H_2})$ value. For Overlap, the one component model proposed by Zhu et al. (2003) has $N(^{12}\mathrm{CO})/\Delta v \approx 1.0{\times}10^{16}$ cm^{-2}/km s^{-1}, $n(\mathrm{H_2}) = 1{-}5{\times}10^3$ cm^{-3} and $T_K = 33$ K for their (0″; 10″) offset positions which almost corresponds to our Overlap position. The agreement of the former study with our values is not as good as for NGC 4038 but Zhu et al. (2003) used a higher CO abundance ratio (^{12}CO/^{13}CO = 60) than we do (40), which may be at the origin of the differences. For M 83, Israel & Baas (2001) presented two LVG models: one with $N(^{12}\mathrm{CO})/\Delta v = 1{-}3 \times 10^{17}$ cm^{-2}/km s^{-1}, $T_K = 30{-}150$ K and $n(\mathrm{H_2}) = 0.5{-}3.0 \times 10^3$ cm^{-3}, and one with $N(^{12}\mathrm{CO})/\Delta v = 0.06{-}1 \times 10^{17}$ cm^{-2}/km s^{-1}, $T_K = 60{-}100$ K and $n(\mathrm{H_2}) = 0.03{-}1.0 \times 10^5$ cm^{-3}. Our fitted parameters compare well with both models, although they are closer to the second model conditions. For NGC 6946, Walsh et al. (2002) proposed the following LVG model: $N(^{12}\mathrm{CO})/\Delta v = 2.9 \times 10^{16}$ cm^{-2}/km s^{-1}, $T_K = 40$ K and $n(\mathrm{H_2}) = 2.0{\times}10^3$ cm^{-3}. Israel & Baas (2001) presented two other possible LVG models: one with $N(^{12}\mathrm{CO})/\Delta v = 1{-}10 \times 10^{17}$ cm^{-2}/km s^{-1}, $T_K = 30{-}150$ K and $n(\mathrm{H_2}) = 0.5{-}1.0 \times 10^3$ cm^{-3}, and one with $N(^{12}\mathrm{CO})/\Delta v = 3{-}6 \times 10^{16}$ cm^{-2}/km s^{-1}, $T_K = 30{-}150$ K and $n(\mathrm{H_2}) = 0.1{-}1.0 \times 10^4$ cm^{-3}. All these models are consistent with the parameters obtained in the present work.

5.3. PDR models

5.3.1. Fitting procedures

We use the PDR models developed by Le Bourlot et al. (1993) for Galactic sources (see also Le Petit et al. 2002). The source is modelled as a plane-parallel slab, illuminated on both sides by FUV radiation to better reproduce a starburst environment where massive stars, and giant molecular clouds, are spatially correlated. Model parameters include the gas density, assumed uniform, the intensity of the illuminating FUV radiation, the gas phase elemental abundances, the grain properties and the gas to dust ratio.

We considered that all galaxies have a metallicity close to solar (see Table 1), and we used Milky Way abundances in our models ($12 + \log(\frac{\mathrm{O}}{\mathrm{H}}) = 8.90 \pm 0.04$ Arimoto et al. 1996). For IC 10 and IC 342, this hypothesis may be rather crude considering the lower and higher (respectively) metallicity of their nuclei ($12 + \log(\frac{\mathrm{O}}{\mathrm{H}}) = 8.31 \pm 0.2$ in Arimoto et al. 1996 and $12 + \log(\frac{\mathrm{O}}{\mathrm{H}}) = 9.30$ in Vila-Costas & Edmunds 1992). Therefore results obtained on these sources should be considered more cautiously. Standard grain properties and a gas to dust ratio appropriate for Galactic interstellar clouds have been adopted. The ^{12}C/^{13}C ratios are the same as used above for the LVG models (see Table 3). We have sampled a wide range of parameter space, varying the gas density, n(H) from 1.0×10^2 cm^{-3} to 1.0×10^7 cm^{-3}, and the incident FUV flux, χ_{FUV}, from 1.5×10^3 G_0 to 1.5×10^6 G_0, where G_0 is the local average interstellar radiation field (ISRF) determined by Draine (1978) ($G_0 = 2.7 \times 10^{-3}$ erg cm^{-2} s^{-1}). We fit the PDR models with the same line intensity ratios used to fit the the LVG models (see Table 5) but computed from values listed in Table B.2 (with an asterisk) expressed in Wm^{-2} sr^{-1}, a unit more appropriate for PDR model calculations. Indeed, the output values (emissivities) from PDR models calculations are expressed in erg cm^{-2} s^{-1} sr^{-1}.

The best model is obtained using a least square fitting method as applied in Sect. 5.2 taking into account the errors on the observations.

5.3.2. Results

Best fit solutions (physical parameters) for the selected galaxies are presented in Table 3. Model predictions for the CO line emissivities are shown in the right side of Figs. 20−25 for IC 10, IC 342, NGC 4038, Overlap, M 83 and NGC 6946, respectively. Model predictions have been scaled by a surface filling factor ($\mathrm{FF_{PDR}}$ listed in Table 3) to match the observed line intensities. As stated above, PDR models have been developed for local interstellar clouds. The velocity dispersion of the modelled cloud is a parameter in those models, which is used for computing the photo-dissociation rates of $\mathrm{H_2}$ and CO, and the line emissivities. This parameter is set to 1 km s^{-1}, a typical figure for local molecular clouds (see Wolfire et al. 1990). Using a PDR model for fitting galaxy observations is complicated by the fact that, in a galaxy, many PDRs contribute to the signal detected in each beam, resulting in a broad line (tens to hundreds of km s^{-1}), compared to a single PDR line (1 km s^{-1}). To correct for this effect, the modelled emissivities have been multiplied by the line width ratio, $\frac{\Delta v(\mathrm{galaxy})}{\Delta v(\mathrm{PDR})}$, where Δv(galaxy) is the line width of the CO lines as reported in Table 3, and where $\Delta v(\mathrm{PDR}) = 1$ km s^{-1}. Once this correction is performed, PDR model results are compared with observed data in the same way as the LVG models (see Sect. 5.2). The surface filling factors of the emission in the beam, $\mathrm{FF_{PDR}}$, are also computed (and listed in Table 3) and they are in reasonable agreement with those derived from LVG models for all sources.

The PDR solutions obtained from the least square fitting procedure are described below for the individual galaxies. The ^{12}CO and the ^{13}CO cooling rates are summarized in Table 3.

- For IC 10, the "best" model is represented in Fig. 20 with grey squares. The ^{12}CO(5−4) line represents 24.7% of the total ^{12}CO cooling rate while the ^{12}CO(6−5) and ^{12}CO(4−3) lines correspond to 24.6% and 16.8%, respectively. The main lines for the ^{13}CO cooling rate are the ^{13}CO(5−4) (33.0%), ^{13}CO(6−5) (26.8%) and ^{13}CO(4−3) (25.8%) lines.
- For IC 342, the "best" model is represented in Fig. 21 with grey squares. The lines which contribute the most to the ^{12}CO cooling rate are the ^{12}CO(5−4) (27.3% of the total intensity), ^{12}CO(6−5) (23.6%) and ^{12}CO(4−3) (20.1%) lines. The lines which contribute the most to the ^{13}CO cooling rate are the ^{13}CO(4−3) (30.6%), ^{13}CO(5−4) (29.6%) and ^{13}CO(3−2) (17.7%) lines.

Table 5. Observed and predicted ("best" PDR model) line intensity ratios.

I (Wm^{-2} sr^{-1})	IC 10 obs.*	IC 342 obs.*	I (Wm^{-2} sr^{-1})	NGC 4038 obs.*	OVERLAP obs.*
$\frac{^{12}CO(3-2)}{^{12}CO(4-3)}$	0.8 ± 0.1^{a}	0.9 ± 0.1^{a}	$\frac{^{12}CO(3-2)}{^{12}CO(4-3)}$	$0.6 \pm 7.7 \times 10^{-2}$	1.0 ± 0.1
$\frac{^{12}CO(3-2)}{^{12}CO(6-5)}$	$0.3 \pm 6.3 \times 10^{-2,a}$	$0.5 \pm 4.5 \times 10^{-2,a}$	$\frac{^{12}CO(3-2)}{^{12}CO(6-5)}$	$0.1 \pm 2.4 \times 10^{-2,a}$	$0.2 \pm 9.4 \times 10^{-2,a}$
$\frac{^{12}CO(3-2)}{^{12}CO(7-6)}$	0.7 ± 0.2^{a}	1.2 ± 0.1^{a}	$\frac{^{12}CO(3-2)}{^{12}CO(7-6)}$	1.8 ± 0.6^{a}	1.2 ± 0.2^{a}
$\frac{^{12}CO(2-1)}{^{12}CO(7-6)}$	0.3 ± 0.1^{a}	0.4 ± 0.1	$\frac{^{12}CO(2-1)}{^{12}CO(6-5)}$	$(5.8 \pm 1.9) \times 10^{-2,a}$	$(8.3 \pm 4.9) \times 10^{-2,a}$
$\frac{^{12}CO(3-2)}{^{13}CO(3-2)}$	11.8 ± 2.3^{a}	6.3 ± 0.8^{a}	$\frac{^{12}CO(3-2)}{^{13}CO(3-2)}$	20.6 ± 12.6^{a}	$34.5 \pm 9.4^{a,b}$
$\frac{^{12}CO(1-0)}{^{13}CO(1-0)}$	–	12.9 ± 0.5	$\frac{^{12}CO(1-0)}{^{13}CO(1-0)}$	–	–
$\frac{^{12}CO(2-1)}{^{13}CO(2-1)}$	17.6 ± 7.0	12.5 ± 3.0	$\frac{^{12}CO(2-1)}{^{13}CO(2-1)}$	27.9 ± 11.1	18.6 ± 7.5
	PDR model	PDR model		PDR model	PDR model
$\frac{^{12}CO(3-2)}{^{12}CO(4-3)}$	0.5	0.5	$\frac{^{12}CO(3-2)}{^{12}CO(4-3)}$	0.4	0.4
$\frac{^{12}CO(3-2)}{^{12}CO(6-5)}$	0.3	0.4	$\frac{^{12}CO(3-2)}{^{12}CO(6-5)}$	0.2	0.2
$\frac{^{12}CO(3-2)}{^{12}CO(7-6)}$	0.5	0.9	$\frac{^{12}CO(3-2)}{^{12}CO(7-6)}$	0.3	0.2
$\frac{^{12}CO(2-1)}{^{12}CO(7-6)}$	0.1	0.3	$\frac{^{12}CO(2-1)}{^{12}CO(6-5)}$	4.5×10^{-2}	4.9×10^{-2}
$\frac{^{12}CO(3-2)}{^{13}CO(3-2)}$	12.3	6.3	$\frac{^{12}CO(3-2)}{^{13}CO(3-2)}$	19.6	15.7
$\frac{^{12}CO(1-0)}{^{13}CO(1-0)}$	18.9	11.3	$\frac{^{12}CO(1-0)}{^{13}CO(1-0)}$	24.6	22.6
$\frac{^{12}CO(2-1)}{^{13}CO(2-1)}$	14.6	7.1	$\frac{^{12}CO(2-1)}{^{13}CO(2-1)}$	21.9	18.5

	M 83 obs.*	NGC 6946 obs.*
$\frac{^{12}CO(3-2)}{^{12}CO(4-3)}$	0.5 ± 0.2^{a}	0.6 ± 0.1^{a}
$\frac{^{12}CO(3-2)}{^{12}CO(6-5)}$	$0.1 \pm 3.9 \times 10^{-2,a}$	0.6 ± 0.1^{a}
$\frac{^{12}CO(3-2)}{^{12}CO(7-6)}$	–	–
$\frac{^{12}CO(2-1)}{^{12}CO(6-5)}$	$(5.2 \pm 3.8) \times 10^{-2,a}$	$0.3 \pm 5.9 \times 10^{-2,a}$
$\frac{^{12}CO(3-2)}{^{13}CO(3-2)}$	32.7 ± 10.1^{a}	19.5 ± 2.3^{a}
$\frac{^{12}CO(1-0)}{^{13}CO(1-0)}$	–	12.7 ± 5.1
$\frac{^{12}CO(2-1)}{^{13}CO(2-1)}$	$5.1 \pm 0.6 \times 10^{-2}$	34.0 ± 7.6
	PDR model	PDR model
$\frac{^{12}CO(3-2)}{^{12}CO(4-3)}$	0.4	0.5
$\frac{^{12}CO(3-2)}{^{12}CO(6-5)}$	0.2	0.5
$\frac{^{12}CO(3-2)}{^{12}CO(7-6)}$	0.2	1.0
$\frac{^{12}CO(2-1)}{^{12}CO(6-5)}$	5.1×10^{-2}	0.1
$\frac{^{12}CO(3-2)}{^{13}CO(3-2)}$	9.8	18.3
$\frac{^{12}CO(1-0)}{^{13}CO(1-0)}$	19.3	22.2
$\frac{^{12}CO(2-1)}{^{13}CO(2-1)}$	12.6	20.1

* Ratio derived from observations marked with asterisks in Table B.2; [a] values used as constraints for the LVG models; [b] value from Table 2 in Zhu et al. (2003); – values not observed neither found in literature.

- For NGC 4038, the "best" model is represented in Fig. 22 with grey squares. The lines which contribute the most to the ^{12}CO and to the ^{13}CO cooling rates are the $^{12}CO(6-5)$ (23.4% of the total intensity), $^{12}CO(5-4)$ (20.3%), $^{12}CO(7-6)$ (19.0%) lines and the $^{13}CO(6-5)$ (35.7%), $^{13}CO(5-4)$ (33.4%) and $^{13}CO(4-3)$ (21.1%) lines, respectively.
- For the Overlap region, the "best" model is represented in Fig. 23 with grey squares. The lines which contribute the most to the ^{12}CO and to the ^{13}CO cooling rates are the $^{12}CO(6-5)$ (22.9% of the total intensity), $^{12}CO(7-6)$ (19.7%), $^{12}CO(5-4)$ (19.1%) lines and the $^{13}CO(6-5)$ (34.7%), $^{13}CO(5-4)$ (33.3%) and $^{13}CO(4-3)$ (21.6%) lines, respectively.
- For M 83, the "best" model is represented in Fig. 24 with grey squares. The lines which contribute the most to the ^{12}CO cooling rate are the $^{12}CO(6-5)$ (20.4% of the total intensity), $^{12}CO(7-6)$ (20.4%) and $^{12}CO(5-4)$ (15.4%) lines. The lines which contribute the most to the ^{13}CO cooling rate are the $^{13}CO(6-5)$ (34.1%), $^{13}CO(5-4)$ (32.9%) and $^{13}CO(4-3)$ (21.9%) lines.
- For NGC 6946, the "best" model is represented in Fig. 25 with grey squares. The lines which contribute the most to the ^{12}CO cooling rate are the $^{12}CO(5-4)$ (28.5% of the total

intensity), ^{12}CO(4−3) (22.7%) and ^{12}CO(6−5) (21.6%) lines. The main lines for the ^{13}CO cooling rate are the ^{13}CO(5−4) (33.0%), ^{13}CO(4−3) (27.8%) and ^{13}CO(6−5) (23.7%) lines.

For the IC 10 nucleus (Fig. 20), we obtained a good agreement between the two solutions proposed by the LVG and PDR models (similarly shaped curves and ^{12}CO cooling rates); probably because of the high data quality. Small differences appear in the ^{13}CO cooling curves since the peak seems to be located at the ^{13}CO(4−3) transition for the LVG model while the PDR peak clearly corresponds to the ^{13}CO(5−4) transition. ^{13}CO(6−5) observations would be very useful to discriminate between the model solutions.

In IC 342 (Fig. 21), we observed an excellent agreement between the two model solutions, the sole difference being in the peak position for the ^{13}CO cooling curves (the LVG peak corresponding to the ^{13}CO(3−2) line while the PDR one being located at ^{13}CO(4−3)). Here also, ^{13}CO(6−5) data would be very useful to better localize the ^{13}CO peak. In this case, we have a very complete and high quality dataset. The ^{12}CO cooling rate deduced from the PDR model is very close to the ^{12}CO cooling rate computed from the LVG model.

At the Antennae positions (Overlap and NGC 4038 in Figs. 22 and 23), LVG models, as well as PDR models, do not reproduce observations adequately due to the low signal-to-noise ratio of both ^{12}CO(7−6) and ^{12}CO(4−3) lines. Indeed, because these latter observations are weaker than we expected, we have not considered them in the least square fitting procedures. However, for NGC 4038, both model solutions (LVG and PDR) are coherent: the maximum of the ^{12}CO cooling curve deduced from the LVG model is the same as the result from the PDR model (^{12}CO(6−5)) and the ^{12}CO cooling rates are similar. For Overlap, the maxima of the LVG and PDR ^{12}CO cooling curves appear both for ^{12}CO(6−5) and the predicted ^{12}CO cooling rates from the LVG and PDR models are close to each other. Despite this, we clearly see differences in the predicted line intensities from LVG and PDR models, certainly due to the lack of relevant ^{12}CO(7−6) detections. Concerning the ^{13}CO cooling curves shown in the right side of Fig. 22 (for NGC 4038) the two model solutions are compatible. Consequently, the total ^{13}CO cooling rate agrees between the LVG and PDR models (see Table 3). For the Overlap position (Fig. 23), the LVG and PDR ^{13}CO cooling curves peak at the different positions (^{13}CO(6−5) for the PDR and ^{13}CO(5−4) for the LVG) but the ^{13}CO cooling rate are different by a factor $\lesssim$3 (see Table 3). For NGC 4038 and Overlap, ^{13}CO(6−5) observations would be very useful to discriminate between model solutions.

For M 83, the lack of ^{12}CO(7−6) data explains the differences (noticeable in Figs. 24) between the LVG and PDR solutions for the ^{12}CO cooling curves. The peak corresponds to the ^{12}CO(7−6) line in the LVG and PDR models. Observations of the ^{12}CO(7−6), ^{12}CO(8−7) lines and possibly up would be very useful. Despite the different shape of the ^{12}CO cooling curves, very similar ^{13}CO cooling curves are obtained. We notice that although the M 83 dataset is less complete than for other sources, we obtained fairly similar values of the LVG and PDR ^{12}CO cooling rates (see Table 3).

For NGC 6946, the peak positions of the ^{12}CO cooling curves are similar (^{12}CO(5−4)) for the LVG and the PDR models. Also in this case, observations of the ^{12}CO(7−6) and ^{12}CO(8−7) lines appear essential to discriminate between model solutions. For the ^{13}CO cooling curve, we observed stronger differences especially for the peak position since the LVG maximum corresponds to the ^{13}CO(3−2) line while the PDR maximum appears for the ^{13}CO(5−4) line. Once again, the ^{13}CO(6−5) observation would be very useful to better localize the ^{13}CO peak.

5.3.3. Discussion

As PDR models provide predictions for lines of C^+, O, and C together with CO rotational lines, it is interesting to check whether the proposed PDR solutions are appropriate to reproduce observation of other cooling lines such as the fine structure lines of atomic carbon. In fact, for all sources studied here (see Table 3), the predicted C cooling rates are typically larger than those observed one by significant factors (between 4.5 and 50).

For a large majority of the sample galaxies, we conclude that PDR models focussed on the high-J CO lines do not correctly reproduce the observed atomic carbon data well. To better model the observed atomic carbon transitions, another set of physical conditions might be a better choice. For example, we could have increased the total extinction A_v, set to 10 mag in the PDR models we used. It is expected that the relative contributions of C and CO will change as CO lines are produced at larger depths than C. We performed a few calculations, variyng the total extinction across the slab, A_v. As expected, Co lines become more prominent relative to C lines with increased A_v. However, the observed ratio is never reached. A more completed study of the parameter space is needed, which is beyond the scope of this paper.

6. Comparison with the Center of Milky Way and the Cloverleaf QSO

It is interesting to compare this galaxy sample with other, well known, sources. As we previously discussed previously, the peak position of the ^{12}CO cooling curves shifts between nuclei. In Figs. 26 and 27, we compare the ^{12}CO cooling curves for the center of the Milky Way and the Cloverleaf QSO [HB89] 1413+117 with our sample galaxies. We completed the set of observed ^{12}CO lines with predictions from PDR models up to ^{12}CO(15−14). Because the PDR model for Overlap is less reliable, we excluded this source from this study. We have kept NGC 4038 because LVG and PDR model results are consistent for this object. Flux values for the center of the Milky Way and for the Cloverleaf QSO are from Fixsen et al. (1999) and Barvainis et al. (1997); Tsuboi et al. (1999); Weiß et al. (2003), respectively.

The CO cooling rates (listed in Table 3) appear to be higher in the starburst environments (NGC 253 in Bayet et al. 2004, M 83) than in the normal spiral galaxy (IC 342, NGC 6946) or irregular galaxies (Henize 2−10 in Bayet et al. 2004 and IC 10). This phenomenon seems not to be solely a distance effect since we obtained the highest observed CO cooling rates for NGC 253 and M 83, two galaxies which are neither the nearest nor the farthest sources (2.5 Mpc and 3.5 Mpc, respectively). Moreover, the lowest observed CO cooling rates are obtained for Henize 2−10 and IC 10 which distances are 6 Mpc and 1 Mpc, respectively.

By looking at Figs. 26 and 27, we can distinguish three different behaviors : for Henize 2−10 and the Cloverleaf QSO, the CO cooling curve peaks at the ^{12}CO(7−6) line or up; for IC 10, NGC 253, NGC 4038, M 83 and NGC 6946, the turnover

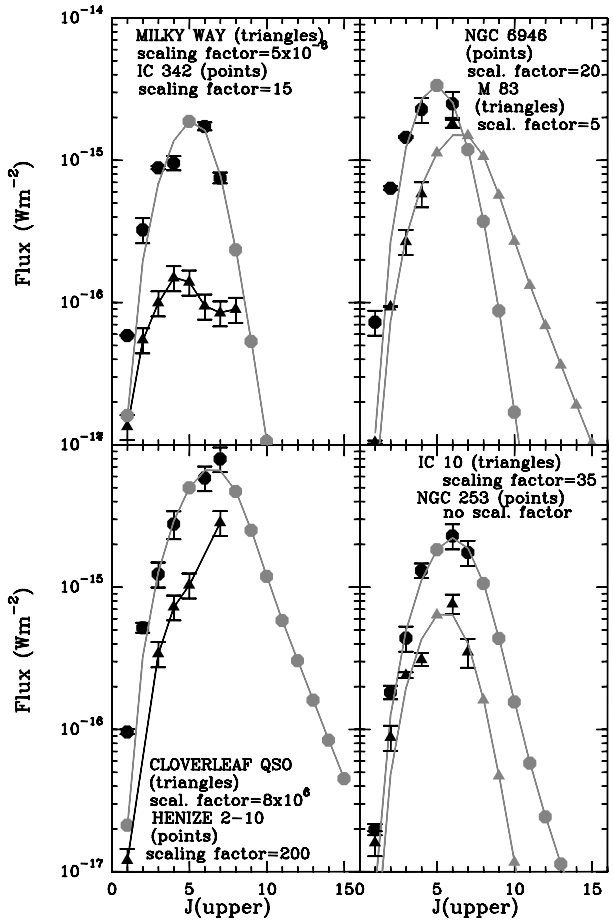

Fig. 26. Flux (Wm^{-2}) vs. J_{upper} for the center of the Milky Way (*top left*, triangles), IC 342 (*top left*, points), NGC 6946 (*top right*, points), M 83 (*top right*, triangles), the Cloverleaf QSO (*bottom left*, triangles), Henize 2−10 (*bottom left*, points) IC 10 (*bottom right*, triangles) and NGC 253 (*bottom right*, points). PDR models (grey points or grey triangles) have been used to obtained line fluxes of unobserved lines (e.g. ^{12}CO(5−4), ^{12}CO(7−6), ^{12}CO(8−7), ^{12}CO(9−8), ...) depending on the completeness of the dataset obtained for each source. Observations are shown in black with error bars. To ease the comparison, we applied scaling factors on all sources data except for NGC 253. The value of these scaling factors is specified for each source on the plots. We notice that for the Cloverleaf QSO, the ^{12}CO(1−0) line flux is an upper limit (see Tsuboi et al. 1999).

appears at the ^{12}CO(6−5) line[2]; and for the center of the Milky Way and IC 342, the turnover is found near the ^{12}CO(4−3) line. We may ask whether these observed differences are solely consequences of the difference in linear resolution solely, or whether they are due to differences in physical conditions.

The turnover of the ^{12}CO cooling curve does not depend on the distance, since there is no obvious correlation between the distance and the position of the CO peak. For instance, the fact that the Cloverleaf QSO and Henize 2−10 have very similar CO cooling curve shapes (see Fig. 26), is related to the close similarities of the physical properties of the warm gas for these two sources, which translates into similar CO line ratios.

[2] For NGC 6946, due to the lack of the ^{12}CO(7−6) detection, the LVG and PDR predictions are less reliable than for the other sources for which we have a more complete dataset. To determine the position of the NGC 6946 CO cooling curve, we chose to trust the observations rather than the predictions.

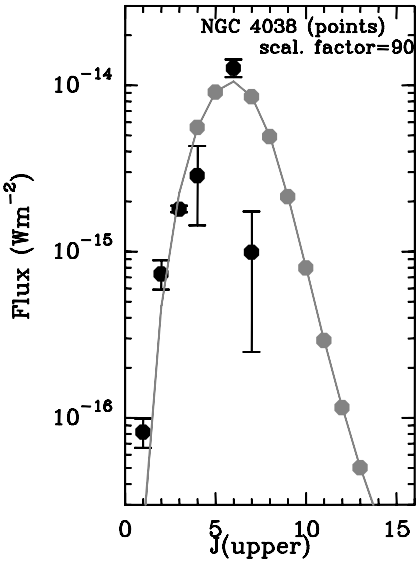

Fig. 27. Flux (Wm^{-2}) vs. J_{upper} for the NGC 4038 nucleus (points). See the caption of Fig. 26. In this figure, we plot observations of the ^{12}CO(4−3) and ^{12}CO(7−6) lines even though they have a low signal-to-noise ratio. We also plot their PDR predicted fluxes.

The position of the peak in the CO cooling curves is a particularly interesting parameter, as it moves towards higher J for more actively star forming galaxies. Indeed, such curves could be used to diagnose the gas properties and measure the cooling rate in galaxies. Few detections are necessary (high-J CO lines as ^{12}CO(6−5) and ^{12}CO(7−6)) to obtain a first estimation of the gas cooling rate.

7. Conclusions

In this paper, we have presented observations of the C and CO submillimeter lines (up to the ^{12}CO(7−6) line at 806 GHz and the [CI]($^3P_2$−$^3P_1$) line at 809 GHz) for the Antennae galaxies (NGC 4038 and the overlap region between the two nuclei), the nuclei of IC 10, IC 342, M 83 and NGC 6946 (see Tables B.1 and B.2). We also detected submillimeter C and CO lines for the following galaxies: nucleus of Arp 220, Centaurus A, IRAS 10565+2448, M 51, M 82, Markarian 231, NGC 3079, NGC 4736, NGC 6090 nuclei and in the spiral arms of M 83 and NGC 6946.

We succeed in fitting all observed CO lines to accurately estimate the CO cooling rate. LVG and PDR models have been used for fitting the CO line intensities. As we selected sources with different morphological types, we have compared the contribution of C and CO and the shape of the CO cooling curves between galaxies.

1 The total CO cooling rates were estimated summing intensities (I in Wm^{-2} sr^{-1}) of all CO transitions up to ^{12}CO(15−14), derived either from observations or from PDR model predictions. We showed that the total CO cooling rate is higher in the starburst nuclei (M 83 and NGC 253) than in normal galaxies (IC 342 and NGC 6946) and irregular galaxies (IC 10 and Henize 2−10).
2 The shape of the CO cooling curve depends on the galaxy activity. The CO cooling is maximum for the the ^{12}CO(7−6) line and up for Henize 2−10 and the Cloverleaf QSO, while for IC 10, NGC 253, NGC 4038, M 83 and NGC 6946 the turnover appears at the ^{12}CO(6−5) line. For the center of the

Milky Way and IC 342, the turnover is located at ^{12}CO(4−3) line. These lines are the main CO cooling lines, which shows the predominant role of the high-J CO lines ($\gtrsim^{12}$CO(5−4)) in the molecular gas cooling. *The shape of the CO cooling curve can be used as a diagnostic of the galaxy star forming activity*.

3 Whatever the morphological type, the C cooling rates are lower than the CO cooling rates (the ratio varies from a factor of $\lesssim$4.0 for IC 10 and IC 342, of $\geqslant$10 for NGC 253 and Henize 2−10 (reported in Bayet et al. 2004). The factor are estimated to be $\approx$20 for NGC 4038, Overlap, M 83 and NGC 6946. As we missed the [CI](^{3}P$_2$−^{3}P$_1$) line at 809 GHz for the Antennae, M 83 and NGC 6946, the latter figures should be confirmed with more observations.

Our analysis made use of two complementary models: LVG models (Large Velocity Gradient for radiative transfer calculations) and PDR models (combining chemistry, thermal balance and radiative transfer) for deriving the physical conditions in the galaxy nuclei, and for computing the intensity of the missing CO lines. We obtained the following results:

4 We succeeded in deriving physical properties (the kinetic temperature (T_K), the gas density (n(H$_2$)), the CO column density divided by the line width ($N(^{12}\mathrm{CO})/\Delta v$) and the Far-UV radiation field (χ_{FUV})) of the warm and dense molecular gas, using high-J CO and ^{13}CO line intensity ratios for constraining the models. The LVG models alone can be highly degenerated as an extended region in the (n(H$_2$); T_K) parameter space provides equally good fits. However, best models provide consistent estimations of the CO cooling rates.

5 The surface filling factor of the molecular emission amounts to 1−7% in a 21.9″ beam. High resolution observations, using existing (IRAM-PdBI, SMA) or planned (CARMA, ALMA) (sub)millimeter interferometers, should be able to resolve individual sources in these galaxies.

6 The ^{12}CO(5−4) line appears as one of the main CO cooling line for most sources. Unfortunately, the line is blocked by the atmosphere for local galaxies. Spatial missions (e.g. the Herschel Space Observatory) will soon provide measurements of this important line. We also showed the key role of the ^{13}CO(6−5) and ^{12}CO(8−7) lines as constraints to PDR and LVG models. Future observations with ALMA and the Herschel satellite will provide these informations.

7 While ^{12}CO(3−2) and ^{12}CO(4−3) lines are detected in star forming regions outside galaxy nuclei, we could not detect ^{12}CO(6−5) emission there because of the lack of sensitivity. A similar analysis on spiral arm regions should be performed in the near future.

8 For our galaxy nuclei sample, PDR solutions fitted to the CO lines, do not provide a good match to the fine structure line intensities of neutral carbon.

Acknowledgements. This work has benefitted from financial support from the CNRS/INSU research programs PCMI & PNG. We thank J. Cernicharo and M. Perault for letting us use their CO LVG models and J. Le Bourlot for introducing us to the Meudon PDR model. We made use of the SIMBAD and NED data base for helping us finding basic galaxy properties. The CSO is funded by the NSF under contract # AST 9980846.

References

Aalto, S., Booth, R. S., Black, J. H., & Johansson, L. E. B. 1995, A&A, 300, 369
Arimoto, N., Sofue, Y., & Tsujimoto, T. 1996, PASJ, 48, 275
Baas, F., Israel, F. P., & Koornneef, J. 1994, A&A, 284, 403
Barvainis, R., Maloney, P., Antonucci, R., & Alloin, D. 1997, ApJ, 484, 695
Bayet, E., Gerin, M., Phillips, T. G., & Contursi, A. 2004, A&A, 427, 45
Bennett, C. L., Fixsen, D. J., Hinshaw, G., et al. 1994, ApJ, 434, 587
Bertoldi, F., Cox, P., Neri, R., et al. 2003, A&A, 409, L47
Bolatto, A. D., Jackson, J. M., Wilson, C. D., & Moriarty-Schieven, G. 2000, ApJ, 532, 909
Bradford, C. M., Nikola, T., Stacey, G. J., et al. 2003, ApJ, 586, 891
Bryant, P. M., & Scoville, N. Z. 1999, AJ, 117, 2632
Carilli, C. L., Walter, F., Bertoldi, F., et al. 2004, AJ, 128, 997
Carilli, C. L., Solomon, P., Vanden Bout, P., et al. 2005, ApJ, 618, 586
Casoli, F., Clausset, F., Combes, F., Viallefond, F., & Boulanger, F. 1990, A&A, 233, 357
Clausset, F., Casoli, F., Viallefond, F., & Combes, F. 1991, in Dynamics of Galaxies and Their Molecular Cloud Distributions, IAU Symp. 146, 88
Cox, P., Omont, A., Djorgovski, S. G., et al. 2002, A&A, 387, 406
de Jong, T., Dalgarno, A., & Chu, S. I. 1975, ApJ, 199, 69
de Vaucouleurs, G. 1991, Science, 254, 1667
de Vaucouleurs, G., de Vaucouleurs, A., & Nieto, J. L. 1979, AJ, 84, 1811
Dumke, M., Nieten, C., Thuma, G., Wielebinski, R., & Walsh, W. 2001, A&A, 373, 853
Eckart, A., Downes, D., Genzel, R., et al. 1990, ApJ, 348, 434
Fixsen, D. J., Bennett, C. L., & Mather, J. C. 1999, ApJ, 526, 207
Gao, Y., Lo, K. Y., Lee, S. W., & Lee, T. H. 2001, ApJ, 548, 172
Garnett, D. R. 1998, in Abundance Profiles: Diagnostic Tools for Galaxy History, ASP Conf. Ser., 147, 78
Gerin, M., & Phillips, T. G. 1998, ApJ, 509, L17
Gerin, M., & Phillips, T. G. 1999, in The Physics and Chemistry of the Interstellar Medium, Proceedings of the 3rd Cologne-Zermatt Symposium, held in Zermatt, September 22−25, 1998, ed. V. Ossenkopf, J. Stutzki, & G. Winnewisser, GCA-Verlag Herdecke, 58
Gerin, M., & Phillips, T. G. 2000, ApJ, 537, 644
Glenn, J., & Hunter, T. R. 2001, ApJS, 135, 177
Goicoechea, J. R., Martín-Pintado, J., & Cernicharo, J. 2005, ApJ, 619, 291
Goldreich, P., & Kwan, J. 1974, ApJ, 189, 441
Goldsmith, P. F., & Langer, W. D. 1978, ApJ, 222, 881
Guesten, R., Serabyn, E., Kasemann, C., et al. 1993, ApJ, 402, 537
Handa, T., Nakai, N., Sofue, Y., Hayashi, M., & Fujimoto, M. 1990, PASJ, 42, 1
Harris, A. I., Stutzki, J., Graf, U. U., et al. 1991, ApJ, 382, L75
Harrison, A., Puxley, P., Russell, A., & Brand, P. 1995, MNRAS, 277, 413
Harrison, A., Henkel, C., & Russell, A. 1999, MNRAS, 303, 157
Henkel, C., Chin, Y. N., Mauersberger, R., & Whiteoak, J. B. 1998, A&A, 329, 443
Hollenbach, D. J., & Tielens, A. G. G. M. 1999, Rev. Mod. Phys., 71, 173
Ishizuki, S., Kawabe, R., Ishiguro, M., et al. 1990, ApJ, 355, 436
Israel, F. P., & Baas, F. 2001, A&A, 371, 433
Israel, F. P., & Baas, F. 2002, A&A, 383, 82
Israel, F. P., & Baas, F. 2003, A&A, 404, 495
Israel, F. P., White, G. J., & Baas, F. 1995, A&A, 302, 343
Johansson I. 1987, A&A, 182, 179
Karachentsev, I. D., & Tikhonov, N. A. 1993, A&AS, 100, 227
Kaufman, M. J., Wolfire, M. G., Hollenbach, D. J., & Luhman, M. L. 1999, ApJ, 527, 795
Kobulnicky, H. A., Dickey, J. M., Sargent, A. I., Hogg, D. E., & Conti, P. S. 1995, AJ, 110, 116
Koester, B., Stoerzer, H., Stutzki, J., & Sternberg, A. 1994, A&A, 284, 545
Kramer, C., Mookerjea, B., Bayet, E., et al. 2005, A&A, 441, 961
Le Bourlot, J., Pineau des Forets, G., Roueff, E., & Schilke, P. 1993, ApJ, 416, L87
Le Petit, F., Roueff, E., & Le Bourlot, J. 2002, A&A, 390, 369
Lundgren, A. A., Wiklind, T., Olofsson, H., & Rydbeck, G. 2004, A&A, 413, 505
Malhotra, S., Kaufman, M. J., Hollenbach, D., et al. 2001, ApJ, 561, 766
Mao, R. Q., Henkel, C., Schulz, A., et al. 2000, A&A, 358, 433
Mauersberger, R., & Henkel, C. 1993, Rev. Mod. Astron., 6, 69
Mauersberger, R., Henkel, C., Wielebinski, R., Wiklind, T., & Reuter, H. P. 1996, A&A, 305, 421
Mauersberger, R., Henkel, C., Walsh, W., & Schulz, A. 1999, A&A, 341, 256
McCall, M. L. 1989, AJ, 97, 1341
Meier, D. S., Turner, J. L., & Hurt, R. L. 2000, ApJ, 531, 200
Meier, D. S., Turner, J. L., Crosthwaite, L. P., & Beck, S. C. 2001, AJ, 121, 740
Nieten, C., Dumke, M., Beck, R., & Wielebinski, R. 1999, A&A, 347, L5
Peng, R., Zhou, S., Whiteoak, J. B., Lo, K. Y., & Sutton, E. C. 1996, ApJ, 470, 821

Petitpas, G. R., & Wilson, C. D. 1998a, ApJ, 496, 226
Petitpas, G. R., & Wilson, C. D. 1998b, ApJ, 503, 219
Pety, J., Beelen, A., Cox P., et al. 2004, A&A, 428, L21
Saviane, I., Hibbard, J. E., & Rich, R. M. 2004, AJ, 127, 660
Sofue, Y., Doi, M., Ishizuki, S., Nakai, N., & Handa, T. 1988, PASJ, 40, 511
Sofue, Y., Tutui, Y., Honma, M., et al. 1999, ApJ, 523, 136
Stanford, S. A., Sargent, A. I., Sanders, D. B., & Scoville, N. Z. 1990, ApJ, 349, 492
Sternberg, A., & Dalgarno, A. 1995, ApJS, 99, 565
Stutzki, J., Graf, U. U., Haas, S., et al. 1997, ApJ, 477, L33
Tammann, G. A., & Sandage, A. 1968, ApJ, 151, 825
Thim, F., Tammann, G. A., Saha, A., et al. 2003, ApJ, 590, 256
Tielens, A. G. G. M., & Hollenbach, D. 1985a, ApJ, 291, 722
Tielens, A. G. G. M., & Hollenbach, D. 1985b, ApJ, 291, 747
Tsuboi, M., Miyazaki, A., Imaizumi, S., & Nakai, N. 1999, PASJ, 51, 479
Tully, R. B. 1988, Science, 242, 310
Tully, R. B., & Fisher, J. R. 1987, S&T, 74, 612
Vigroux, L., Mirabel, F., Altieri, B., et al. 1996, A&A, 315, L93
Vila-Costas, M. B., & Edmunds, M. G. 1992, MNRAS, 259, 121
Wall, W. F., Jaffe, D. T., Bash, F. N., & Israel, F. P. 1991, ApJ, 380, 384
Wall, W. F., Jaffe, D. T., Bash, F. N., et al. 1993, ApJ, 414, 98
Walsh, W., Beck, R., Thuma, G., et al. 2002, A&A, 388, 7
Walter, F., Carilli, C., Bertoldi, F., et al. 2004, ApJ, 615, L17
Ward, J. S., Zmuidzinas, J., Harris, A. I., & Isaak, K. G. 2001, Bull. Amer. Astron. Soc., 33, 1482
Ward, J. S., Zmuidzinas, J., Harris, A. I., & Isaak, K. G. 2003, ApJ, 587, 171
Weiß, A., Henkel, C., Downes, D., & Walter, F. 2003, A&A, 409, L41
Weiß, A., Walter, F., & Scoville, N. Z. 2005, A&A, 438, 533
Weliachew, L., Casoli, F., & Combes, F. 1988, A&A, 199, 29
Wilson, C. D., & Reid, I. N. 1991, ApJ, 366, L11
Wilson, C. D., Scoville, N., Madden, S. C., & Charmandaris, V. 2000, ApJ, 542, 120
Wolfire, M. G., Tielens, A. G. G. M., & Hollenbach, D. 1990, ApJ, 358, 116
Zaritsky, D., Kennicutt, R. C., & Huchra, J. P. 1994, ApJ, 420, 87
Zhu, M., Seaquist, E. R., & Kuno, N. 2003, ApJ, 588, 243

Online Material

Appendix A: Convolution formulae

As CO lines have been observed with different spatial resolutions, the line intensities should be convolved to the same linear resolution before performing meaningful comparisons. The final resolution of 21.9″ has been chosen since it corresponds to the beaim size of the CSO when observing at 345 GHz (frequency of the ^{12}CO(3−2)). To perform this convolution, we modelled emitting region of each galaxy using Gaussian profiles either axisymmetric (see Eq. (A.1)) or elliptical (see Eq. (A.2)):

$$f_s(x,y) = f_0 \frac{1}{\pi\sigma_s^2} \exp - \frac{x^2+y^2}{\sigma_s^2} \quad (A.1)$$

$$f_s(x,y) = f_0 \frac{1}{\pi\sigma_{s,x}\sigma_{s,y}} \exp - \frac{x^2}{\sigma_{s,x}^2} \exp - \frac{y^2}{\sigma_{s,x}^2} \quad (A.2)$$

where f_0 is a normalisation constant and where the Full Width Half Maximum ($FWHM$) is $FWHM_s = 2\sigma_s\sqrt{\ln 2}$ in the axisymmetric case, and $FWHM_{s,x} = 2\sigma_{s,x}\sqrt{\ln 2}$ et $FWHM_{s,y} = 2\sigma_{s,y}\sqrt{\ln 2}$ in the elliptical case. The beam profile is also Gaussian, with a beam size $FWHM_{\rm obs} = 2\sigma_{\rm obs}\sqrt{\ln 2}$. The true source size ($FWHM_s$) is obtained by performing a deconvolution of the observed size using the known beam profile.

The final line intensities is obtained by multiplying the observed signal by the following scaling factor, which depends on the source size, initial and final spatial resolution :

$$\text{fact} = \frac{\theta_{\rm mb,init}^2 + FWHM_s^2}{\theta_{\rm mb,fin}^2 + FWHM_s^2} \quad (A.3)$$

for the axisymmetric case, and:

$$\text{fact} = \sqrt{\frac{\theta_{\rm mb,init}^2 + FWHM_{s,x}^2}{\theta_{\rm mb,fin}^2 + FWHM_{s,x}^2}} \sqrt{\frac{\theta_{\rm mb,init}^2 + FWHM_{s,y}^2}{\theta_{\rm mb,fin}^2 + FWHM_{s,y}^2}} \quad (A.4)$$

for elliptical sources.

Appendix B: Tables of data

Table B.1. Results from the Gaussian fits derived from spectra of the Antennae (NGC 4038 et Overlap), Arp 220, Centaurus A, Henize 2-10, IC 10, IC 342, IRAS 10565, M 51, M 82, M 83, Mrk 231, NGC 253, NGC 891, NGC 1068, 3079, NGC 4736, NGC 6090 and NGC 6946. The observed lines (^{12}CO, ^{13}CO and C) are indicated in the first column. For each source, the RA(1950) and DEC(1950) positions of the center (0″,0″) is listed in Table 1. The indication ^{a} corresponds to the spectra shown in this article (see Figs. 1 to 16).

Transition	Freq (GHz)	beam size(″)	offset position(″)	$\int(T_{\rm mb}{\rm d}v)$ (K km s^{-1})	Intensity (Wm^{-2}sr^{-1})	Flux (Wm^{-2})
The Antennae NGC 4038						
CI(^{3}P$_1$–^{3}P$_0$)	492.162	14.55	(0,0)^a	13.7 ± 2.1	1.7×10^{-9}	9.4×10^{-18}
^{12}CO(2–1)	230.538	30.50	(0,0)^a	35.6 ± 1.3	4.5×10^{-10}	1.1×10^{-17}
^{12}CO(3–2)	345.796	21.90	(–20,0)	15.9 ± 1.8	6.7×10^{-10}	8.6×10^{-18}
		21.90	(–10,0)	29.5 ± 1.4	1.2×10^{-9}	1.6×10^{-17}
		21.90	(0,0)^a	37.2 ± 1.7	1.6×10^{-9}	2.0×10^{-17}
		21.90	(0,10)	23.4 ± 1.3	9.9×10^{-10}	1.3×10^{-17}
		21.90	(10,0)	23.5 ± 2.2	9.9×10^{-10}	1.3×10^{-17}
^{13}CO(3–2)	330.588	21.90	(0,0)^a	2.1 ± 1.2	7.6×10^{-11}	9.8×10^{-19}
^{12}CO(4–3)	461.041	14.55	(0,0)^a	45.3 ± 3.5	4.5×10^{-9}	2.6×10^{-17}
^{12}CO(6–5)	691.473	10.60	(3,3)^a	85.5 ± 10.4	2.9×10^{-8}	8.7×10^{-17}
^{12}CO(7–6)	806.652	8.95	(0,0)^a	2.6 ± 1.6	1.4×10^{-9}	3.0×10^{-18}
		8.95	(3,3)	4.9 ± 1.3	2.6×10^{-9}	5.6×10^{-18}
The Antennae Overlap						
CI(^{3}P$_1$–^{3}P$_0$)	492.162	14.55	(0,0)^a	11.2 ± 1.5	1.4×10^{-9}	7.7×10^{-18}
^{12}CO(2–1)	230.538	30.50	(–20,–10)	20.7 ± 2.6	2.6×10^{-10}	6.4×10^{-18}
		30.50	(0,–20)	8.9 ± 2.7	1.1×10^{-10}	2.8×10^{-18}
		30.50	(0,0)^a	51.0 ± 2.6	6.4×10^{-10}	1.6×10^{-17}
		30.50	(0,20)	58.3 ± 2.6	7.3×10^{-10}	1.8×10^{-17}
		30.50	(0,40)	24.8 ± 2.6	3.1×10^{-10}	7.7×10^{-18}
^{12}CO(3–2)	345.796	21.90	(0,0)^a	56.8 ± 3.5	2.4×10^{-9}	3.1×10^{-17}
		21.90	(0,20)	43.2 ± 3.0	1.8×10^{-9}	2.3×10^{-17}
		21.90	(10,0)	31.5 ± 3.1	1.3×10^{-9}	1.7×10^{-17}
		21.90	(10,10)	22.0 ± 4.0	9.3×10^{-10}	1.2×10^{-17}
^{12}CO(4–3)	461.041	14.55	(0,0)^a	45.1 ± 2.4	4.5×10^{-9}	2.5×10^{-17}
^{12}CO(6–5)	691.473	10.60	(0,–3)^a	97.0 ± 37.1	3.3×10^{-8}	9.8×10^{-17}
^{12}CO(7–6)	806.652	8.95	(0,0)^a	13.4 ± 1.6	7.2×10^{-9}	1.5×10^{-17}
ARP 220						
CI(^{3}P$_1$–^{3}P$_0$)	492.162	14.55	(0,0)^a	26.7 ± 2.0	3.3×10^{-9}	1.8×10^{-17}
^{12}CO(3–2)	345.796	21.90	(0,0)^a	27.9 ± 1.9	1.2×10^{-9}	1.5×10^{-17}
CENT-AURUS A						
CI(^{3}P$_1$–^{3}P$_0$)	492.162	14.55	(0,0)^a	81.7 ± 3.2	1.0×10^{-8}	5.6×10^{-17}
IC 10						
CI(^{3}P$_1$–^{3}P$_0$)	492.162	14.55	(5,0)^a	3.9 ± 1.2	4.7×10^{-10}	2.7×10^{-18}
		14.55	(5,10)	5.6 ± 0.6	6.8×10^{-10}	3.8×10^{-18}
		14.55	(–5,10)	4.1 ± 0.4	5.0×10^{-10}	2.8×10^{-18}
CI(^{3}P$_2$–^{3}P$_1$)	809.902	8.95	(0,30)^a	3.0 ± 0.7	1.6×10^{-9}	3.5×10^{-18}
^{12}CO(2–1)	230.538	30.50	(–40,20)	8.0 ± 0.2	1.0×10^{-10}	2.5×10^{-18}
		30.50	(–40,10)	12.3 ± 0.2	1.5×10^{-10}	3.8×10^{-18}
		30.50	(–20,0)	2.1 ± 0.1	2.6×10^{-11}	6.5×10^{-19}
		30.50	(0,–10)	16.4 ± 0.3	2.1×10^{-10}	5.1×10^{-18}
		30.50	(0,0)^a	22.3 ± 0.2	2.8×10^{-10}	7.0×10^{-18}
		30.50	(0,10)	19.1 ± 0.2	2.4×10^{-10}	5.9×10^{-18}
		30.50	(10,0)	26.1 ± 0.2	3.3×10^{-10}	8.1×10^{-18}
		30.50	(10,10)	22.9 ± 0.2	2.9×10^{-10}	7.1×10^{-18}
		30.50	(10,20)	11.4 ± 0.2	1.4×10^{-10}	3.5×10^{-18}
		30.50	(20,0)	13.0 ± 0.3	1.6×10^{-10}	4.1×10^{-18}
		30.50	(30,10)	4.5 ± 0.3	5.7×10^{-11}	1.4×10^{-18}
^{12}CO(3–2)	345.796	21.90	(–45,20)	3.0 ± 0.8	1.3×10^{-10}	1.6×10^{-18}
		21.90	(–45,10)	4.0 ± 0.7	1.7×10^{-10}	2.2×10^{-18}
		21.90	(–35,10)	5.9 ± 0.7	2.5×10^{-10}	3.2×10^{-18}
		21.90	(–35,20)	4.7 ± 0.7	2.0×10^{-10}	2.5×10^{-18}
		21.90	(–5,0)	11.5 ± 0.9	4.9×10^{-10}	6.2×10^{-18}
		21.90	(–5,10)	10.0 ± 0.9	4.3×10^{-10}	5.4×10^{-18}
		21.90	(5,–10)	8.7 ± 0.9	3.7×10^{-10}	4.7×10^{-18}
		21.90	(5,0)^a	12.7 ± 0.7	5.3×10^{-10}	6.8×10^{-18}
		21.90	(5,10)	12.7 ± 0.6	5.4×10^{-10}	6.9×10^{-18}
		21.90	(15,0)	11.1 ± 0.8	4.7×10^{-10}	6.0×10^{-18}

Table B.1. continued.

Transition	Freq (GHz)	beam size(″)	offset position(″)	$\int(T_{\rm mb}{\rm d}v)$ (K km s^{-1})	Intensity (Wm^{-2}sr^{-1})	Flux (Wm^{-2})
		21.90	(15,10)	8.3 ± 0.8	3.5×10^{-10}	4.5×10^{-18}
^{13}CO(3−2)	330.588	21.90	(–10,0)	0.8 ± 0.4	3.1×10^{-11}	4.0×10^{-19}
		21.90	(0,0)[a]	0.9 ± 0.1	3.3×10^{-11}	4.3×10^{-19}
		21.90	(0,10)	1.2 ± 0.2	4.6×10^{-11}	5.8×10^{-19}
		21.90	(0,20)	0.6 ± 0.3	2.1×10^{-11}	2.7×10^{-19}
		21.90	(0,30)	2.8 ± 0.6	1.0×10^{-10}	1.3×10^{-18}
		21.90	(10,0)	0.9 ± 0.3	3.3×10^{-11}	4.3×10^{-19}
^{12}CO(4−3)	461.041	14.55	(–40,10)	4.1 ± 0.6	4.1×10^{-10}	2.3×10^{-18}
		14.55	(–15,10)	5.6 ± 1.9	5.6×10^{-10}	3.2×10^{-18}
		14.55	(–15,20)	3.9 ± 2.3	3.9×10^{-10}	2.2×10^{-18}
		14.55	(–5,10)	6.3 ± 0.9	6.3×10^{-10}	3.5×10^{-18}
		14.55	(5,−10)	8.8 ± 1.9	8.8×10^{-10}	5.0×10^{-18}
		14.55	(5,0)[a]	10.4 ± 1.2	1.0×10^{-9}	5.9×10^{-18}
		14.55	(5,10)	11.3 ± 1.0	1.1×10^{-9}	6.4×10^{-18}
		14.55	(5,20)	7.0 ± 1.2	7.0×10^{-10}	4.0×10^{-18}
		14.55	(15,0)	11.6 ± 1.2	1.2×10^{-9}	6.6×10^{-18}
		14.55	(15,10)	10.7 ± 1.9	1.1×10^{-9}	6.1×10^{-18}
		14.55	(15,20)	6.9 ± 2.0	6.9×10^{-10}	3.9×10^{-18}
^{12}CO(6−5)	691.473	10.60	(0,30)	4.3 ± 1.3	1.5×10^{-9}	4.4×10^{-18}
		10.60	(5,0)	3.1 ± 5.0	1.0×10^{-9}	3.1×10^{-18}
		10.60	(5,10)[a]	11.2 ± 1.7	3.8×10^{-9}	1.1×10^{-17}
^{12}CO(7−6)	806.652	8.95	(0,30)[a]	3.6 ± 0.8	2.0×10^{-9}	4.1×10^{-18}
IC 342						
CI(^{3}P$_2$−^{3}P$_1$)	809.902	8.95	(–5,−5)	29.8 ± 3.9	1.6×10^{-8}	3.5×10^{-17}
		8.95	(–5,0)	35.3 ± 4.6	1.9×10^{-8}	4.1×10^{-17}
		8.95	(0,0)[a]	35.1 ± 3.7	1.9×10^{-8}	4.1×10^{-17}
		8.95	(0,5)	25.8 ± 3.7	1.4×10^{-8}	3.0×10^{-17}
		8.95	(5,−5)	14.9 ± 4.6	8.1×10^{-9}	1.7×10^{-17}
		8.95	(5,0)	49.8 ± 6.3	2.7×10^{-8}	5.8×10^{-17}
		8.95	(5,5)	31.8 ± 6.6	1.7×10^{-8}	3.7×10^{-17}
		8.95	(10,10)	9.0 ± 2.2	4.9×10^{-9}	1.0×10^{-17}
^{12}CO(3−2)	345.796	21.90	(–10,−10)	72.9 ± 6.4	3.1×10^{-9}	3.9×10^{-17}
		21.90	(–10,0)	70.1 ± 3.2	3.0×10^{-9}	3.8×10^{-17}
		21.90	(–10,10)	51.0 ± 5.1	2.2×10^{-9}	2.8×10^{-17}
		21.90	(0,−10)	56.1 ± 7.1	2.4×10^{-9}	3.0×10^{-17}
		21.90	(0,0)[a]	109.8 ± 2.5	4.6×10^{-9}	5.9×10^{-17}
		21.90	(0,10)	97.0 ± 3.5	4.1×10^{-9}	5.2×10^{-17}
		21.90	(0,20)	65.5 ± 4.4	2.8×10^{-9}	3.5×10^{-17}
		21.90	(10,0)	95.3 ± 7.7	4.0×10^{-9}	5.1×10^{-17}
		21.90	(10,10)	69.2 ± 7.4	2.9×10^{-9}	3.7×10^{-17}
		21.90	(10,20)	68.0 ± 3.2	2.9×10^{-9}	3.7×10^{-17}
^{13}CO(3−2)	330.588	21.90	(–10,0)	6.7 ± 0.5	2.5×10^{-10}	3.2×10^{-18}
		21.90	(0,−10)	3.1 ± 0.3	1.1×10^{-10}	1.4×10^{-18}
		21.90	(0,0)[a]	19.9 ± 2.2	7.4×10^{-10}	9.4×10^{-18}
		21.90	(0,10)	9.0 ± 0.4	3.3×10^{-10}	4.3×10^{-18}
		21.90	(10,0)	2.9 ± 0.7	1.1×10^{-10}	1.4×10^{-18}
^{12}CO(4−3)	461.041	14.55	(0,0)	110.8 ± 12.6	1.1×10^{-8}	6.3×10^{-17}
^{12}CO(6−5)	691.473	10.60	(–5,−10)	19.6 ± 16.6	6.6×10^{-9}	2.0×10^{-17}
		10.60	(–5,−5)	84.1 ± 9.5	2.8×10^{-8}	8.5×10^{-17}
		10.60	(–5,0)	72.9 ± 13.1	2.5×10^{-8}	7.4×10^{-17}
		10.60	(–5,5)	23.7 ± 6.4	8.0×10^{-9}	2.4×10^{-17}
		10.60	(0,0)[a]	54.6 ± 3.3	1.8×10^{-8}	5.5×10^{-17}
		10.60	(0,5)	73.3 ± 5.3	2.5×10^{-8}	7.4×10^{-17}
		10.60	(0,10)	54.8 ± 9.6	1.9×10^{-8}	5.5×10^{-17}
		10.60	(5,0)	108.1 ± 7.0	3.7×10^{-8}	1.1×10^{-16}
		10.60	(5,5)	90.9 ± 5.5	3.1×10^{-8}	9.2×10^{-17}
		10.60	(5,10)	80.9 ± 9.6	2.7×10^{-8}	8.2×10^{-17}
		10.60	(5,15)	17.5 ± 4.3	5.9×10^{-9}	1.8×10^{-17}
		10.60	(10,5)	57.0 ± 7.1	1.9×10^{-8}	5.8×10^{-17}
		10.60	(10,10)	81.6 ± 7.3	2.8×10^{-8}	8.3×10^{-17}
^{12}CO(7−6)	806.652	8.95	(–5,−5)	39.8 ± 3.4	2.1×10^{-8}	4.6×10^{-17}
		8.95	(–5,0)	33.0 ± 6.9	1.8×10^{-8}	3.8×10^{-17}
		8.95	(0,−5)	25.1 ± 5.9	1.3×10^{-8}	2.9×10^{-17}
		8.95	(0,0)[a]	30.2 ± 2.8	1.6×10^{-8}	3.5×10^{-17}

Table B.1. continued.

Transition	Freq (GHz)	beam size(″)	offset position(″)	$\int(T_{\rm mb}{\rm d}v)$ (K km s^{-1})	Intensity (Wm^{-2}sr^{-1})	Flux (Wm^{-2})
		8.95	(0,5)	33.3 ± 4.1	1.8×10^{-8}	3.8×10^{-17}
		8.95	(5,−5)	19.0 ± 5.6	1.0×10^{-8}	2.2×10^{-17}
		8.95	(5,0)	40.3 ± 3.5	2.2×10^{-8}	4.6×10^{-17}
		8.95	(5,5)	29.7 ± 4.5	1.6×10^{-8}	3.4×10^{-17}
		8.95	(10,5)	17.7 ± 3.9	9.5×10^{-9}	2.0×10^{-17}
IRAS 10565						
CI(^{3}P$_1$−^{3}P$_0$)	492.162	14.55	(0,0)[a]	11.4 ± 2.1	1.4×10^{-9}	7.8×10^{-18}
^{12}CO(3−2)	345.796	21.90	(0,0)[a]	12.9 ± 2.1	5.5×10^{-10}	7.0×10^{-18}
M 51						
CI(^{3}P$_1$−^{3}P$_0$)	492.162	14.55	(0,0)[a]	15.1 ± 2.6	1.8×10^{-9}	1.0×10^{-17}
		14.55	(−24,−24)[a]	12.8 ± 1.4	1.6×10^{-9}	8.8×10^{-18}
		14.55	(0,12)[a]	8.1 ± 1.5	9.9×10^{-10}	5.6×10^{-18}
^{12}CO(4−3)	461.041	14.55	(−84,−84)	5.5 ± 1.1	5.5×10^{-10}	3.1×10^{-18}
		14.55	(−24,−24)[a]	32.0 ± 3.0	3.2×10^{-9}	1.8×10^{-17}
		14.55	(0,0)[a]	36.7 ± 2.4	3.7×10^{-9}	2.1×10^{-17}
		14.55	(0,12)[a]	16.0 ± 1.8	1.6×10^{-9}	9.1×10^{-18}
M 82						
^{12}CO(2−1)	230.538	30.50	(−10,−10)	131.8 ± 4.2	1.7×10^{-9}	4.1×10^{-17}
		30.50	(−10,0)	267.7 ± 3.5	3.4×10^{-9}	8.3×10^{-17}
		30.50	(−10,10)	352.9 ± 4.1	4.4×10^{-9}	1.1×10^{-16}
		30.50	(0,−10)	148.9 ± 4.0	1.9×10^{-9}	4.6×10^{-17}
		30.50	(0,0)[a]	286.4 ± 2.2	3.6×10^{-9}	8.9×10^{-17}
		30.50	(0,10)	394.0 ± 5.0	4.9×10^{-9}	1.2×10^{-16}
		30.50	(10,−10)	131.2 ± 4.4	1.6×10^{-9}	4.1×10^{-17}
		30.50	(10,0)	293.8 ± 4.3	3.7×10^{-9}	9.1×10^{-17}
		30.50	(10,10)	408.2 ± 5.4	5.1×10^{-9}	1.3×10^{-16}
		30.50	(10,20)	389.7 ± 4.5	4.9×10^{-9}	1.2×10^{-16}
		30.50	(20,20)	328.0 ± 4.0	4.1×10^{-9}	1.0×10^{-16}
		30.50	(30,20)	238.9 ± 3.6	3.0×10^{-9}	7.4×10^{-17}
^{12}CO(6−5)	691.473	10.60	(−10,−10)	218.7 ± 16.4	7.4×10^{-8}	2.2×10^{-16}
		10.60	(−10,0)	154.4 ± 12.7	5.2×10^{-8}	1.6×10^{-16}
		10.60	(−10,10)	111.1 ± 23.9	3.8×10^{-8}	1.1×10^{-16}
		10.60	(−5,−5)	170.0 ± 28.2	5.7×10^{-8}	1.7×10^{-16}
		10.60	(−5,0)	202.6 ± 19.9	6.9×10^{-8}	2.0×10^{-16}
		10.60	(−5,5)	252.5 ± 25.1	8.5×10^{-8}	2.6×10^{-16}
		10.60	(0,−10)	194.8 ± 30.2	6.6×10^{-8}	2.0×10^{-16}
		10.60	(0,−5)	346.8 ± 21.4	1.2×10^{-7}	3.5×10^{-16}
		10.60	(0,0)[a]	263.0 ± 21.0	8.9×10^{-8}	2.7×10^{-16}
		10.60	(0,5)	212.0 ± 20.6	7.2×10^{-8}	2.1×10^{-16}
		10.60	(0,10)	90.8 ± 23.7	3.1×10^{-8}	9.2×10^{-17}
		10.60	(5,−5)	188.2 ± 26.6	6.4×10^{-8}	1.9×10^{-16}
		10.60	(5,0)	280.0 ± 19.6	9.5×10^{-8}	2.8×10^{-16}
		10.60	(5,5)	366.2 ± 28.2	1.2×10^{-7}	3.7×10^{-16}
		10.60	(10,−10)	211.9 ± 15.2	7.2×10^{-8}	2.1×10^{-16}
		10.60	(10,0)	282.1 ± 19.2	9.5×10^{-8}	2.9×10^{-16}
		10.60	(10,10)	219.7 ± 15.8	7.4×10^{-8}	2.2×10^{-16}
M 83						
^{12}CO(2−1)	230.538	30.50	(−10,0)	62.4 ± 1.3	7.8×10^{-10}	1.9×10^{-17}
		30.50	(0,0)[a]	67.4 ± 2.2	8.4×10^{-10}	2.1×10^{-17}
		30.50	(0,10)	65.5 ± 1.4	8.2×10^{-10}	2.3×10^{-17}
		30.50	(0,−10)	101.8 ± 1.5	1.3×10^{-9}	3.2×10^{-17}
		30.50	(10,0)	72.4 ± 1.4	9.1×10^{-10}	2.2×10^{-17}
^{12}CO(3−2)	345.796	21.90	(−90,−60)[a]	21.5 ± 1.4	9.1×10^{-10}	1.2×10^{-17}
		21.90	(0,0)[a]	99.9 ± 1.6	4.2×10^{-9}	5.4×10^{-17}
		21.90	(90,30)[a]	17.9 ± 1.4	7.6×10^{-10}	9.7×10^{-18}
^{13}CO(3−2)	330.588	21.90	(−90,−60)[a]	1.5 ± 0.5	5.5×10^{-11}	7.0×10^{-19}
		21.90	(0,0)[a]	11.8 ± 1.3	4.3×10^{-10}	5.5×10^{-18}
		21.90	(0,10)	11.2 ± 1.2	4.3×10^{-10}	5.3×10^{-18}
		21.90	(90,30)[a]	1.8 ± 0.3	6.8×10^{-11}	8.7×10^{-19}
^{12}CO(4−3)	461.041	14.55	(−90,−60)[a]	14.8 ± 3.0	1.5×10^{-9}	8.4×10^{-18}
		14.55	(−5,−5)	150.1 ± 21.9	1.5×10^{-8}	8.5×10^{-17}
		14.55	(−5,5)	136.1 ± 13.2	1.4×10^{-8}	7.7×10^{-17}
		14.55	(0,0)[a]	159.0 ± 16.4	1.6×10^{-8}	9.0×10^{-17}
		14.55	(0,15)	82.5 ± 8.5	8.3×10^{-9}	4.7×10^{-17}

Table B.1. continued.

Transition	Freq (GHz)	beam size(″)	offset position(″)	$\int(T_{\rm mb}{\rm d}v)$ (K km s^{-1})	Intensity (Wm^{-2}sr^{-1})	Flux (Wm^{-2})
		14.55	(5,−5)	114.1 ± 9.4	1.1×10^{-8}	6.4×10^{-17}
		14.55	(5,5)	286.2 ± 22.7	2.9×10^{-8}	1.6×10^{-16}
		14.55	(10,10)	112.3 ± 13.3	1.1×10^{-8}	6.3×10^{-17}
		14.55	(15,0)	82.4 ± 16.5	8.3×10^{-9}	4.7×10^{-17}
		14.55	(100,30)[a]	19.9 ± 2.7	2.0×10^{-9}	1.1×10^{-17}
^{12}CO(6−5)	691.473	10.60	(−10,0)	134.8 ± 13.7	4.6×10^{-8}	1.4×10^{-16}
		10.60	(−10,5)	65.6 ± 15.5	2.2×10^{-8}	6.6×10^{-17}
		10.60	(−5,−5)	98.6 ± 11.9	3.3×10^{-8}	1.0×10^{-17}
		10.60	(−5,0)	317.5 ± 20.6	1.1×10^{-7}	3.2×10^{-16}
		10.60	(−5,5)	225.8 ± 18.8	7.6×10^{-8}	2.2×10^{-16}
		10.60	(−5,10)	251.7 ± 25.0	8.5×10^{-8}	2.5×10^{-16}
		10.60	(0,−10)	171.7 ± 11.8	5.8×10^{-8}	1.7×10^{-16}
		10.60	(0,−5)	162.0 ± 12.8	5.5×10^{-8}	1.6×10^{-16}
		10.60	(0,0)[a]	235.3 ± 14.5	8.0×10^{-8}	2.4×10^{-16}
		10.60	(0,5)	217.7 ± 20.6	7.4×10^{-8}	2.2×10^{-16}
		10.60	(0,10)	135.2 ± 14.6	4.6×10^{-8}	1.4×10^{-16}
		10.60	(5,0)	81.0 ± 11.3	2.7×10^{-8}	8.2×10^{-17}
		10.60	(5,5)	224.5 ± 21.3	7.6×10^{-8}	2.3×10^{-16}
		10.60	(5,10)	124.0 ± 15.8	4.2×10^{-8}	1.3×10^{-16}
MRK 231						
CI(^{3}P$_1$−^{3}P$_0$)	492.162	14.55	(0,0)[a]	7.5 ± 1.3	9.2×10^{-10}	5.2×10^{-18}
^{12}CO(2−1)	230.538	30.50	(0,0)[a]	11.9 ± 0.5	1.5×10^{-10}	3.7×10^{-18}
^{12}CO(3−2)	345.796	21.90	(0,0)[a]	8.7 ± 0.7	3.7×10^{-10}	4.7×10^{-18}
NGC 891						
CI(^{3}P$_1$−^{3}P$_0$)	492.162	14.55	(0,0)	11.5 ± 1.0	1.4×10^{-9}	7.9×10^{-18}
		14.55	(57,1)	13.3 ± 1.3	1.6×10^{-9}	9.2×10^{-18}
		14.55	(80,−6)	14.9 ± 1.7	1.8×10^{-9}	1.0×10^{-17}
		14.55	(120,−6)	10.8 ± 0.9	1.3×10^{-9}	7.4×10^{-18}
^{13}CO(2−1)	220.39	30.50	(0,0)	4.6 ± 0.3	5.8×10^{-11}	1.4×10^{-18}
		30.50	(9.3,14.5)	5.3 ± 0.4	6.7×10^{-11}	1.7×10^{-18}
		30.50	(17.1,32.9)	3.9 ± 0.7	4.9×10^{-11}	1.2×10^{-18}
		30.50	(25,51)	2.7 ± 0.2	3.4×10^{-11}	8.4×10^{-19}
		30.50	(32.8,69.7)	2.7 ± 0.4	3.4×10^{-11}	8.5×10^{-19}
		30.50	(40.6,88.1)	2.1 ± 0.2	2.6×10^{-11}	6.4×10^{-19}
		30.50	(48.4,107)	4.9 ± 0.6	6.2×10^{-11}	1.5×10^{-18}
		30.50	(56.2,125)	2.4 ± 0.2	3.0×10^{-11}	7.3×10^{-19}
		30.50	(66.3,164)	4.2 ± 0.5	5.2×10^{-11}	1.3×10^{-19}
		30.50	(82,201)	1.4 ± 0.2	1.7×10^{-11}	4.2×10^{-19}
^{12}CO(3−2)	345.796	21.90	(0,0)	11.0 ± 0.3	4.7×10^{-10}	6.0×10^{-18}
		21.90	(7.8,18.4)	11.1 ± 0.6	4.7×10^{10}	6.0×10^{-18}
		21.90	(9.3,14.5)	10.2 ± 0.3	4.3×10^{-10}	5.5×10^{-18}
		21.90	(25,51)	10.1 ± 0.4	4.3×10^{-10}	5.5×10^{-18}
		21.90	(32.8,69.7)	14.0 ± 0.5	5.9×10^{-10}	7.6×10^{-18}
		21.90	(40.6,88.1)	13.2 ± 0.4	5.6×10^{-10}	7.1×10^{-18}
		21.90	(48.4,106.5)	13.8 ± 2.0	5.8×10^{-10}	7.5×10^{-18}
		21.90	(56.2,125)	3.2 ± 0.3	1.3×10^{-10}	1.7×10^{-18}
NGC 3079						
CI(^{3}P$_1$−^{3}P$_0$)	492.162	14.55	(0,0)	59.6 ± 3.8	7.3×10^{-9}	4.1×10^{-17}
		14.55	(0,0)	56.7 ± 3.2	6.9×10^{-9}	3.9×10^{-17}
^{12}CO(3−2)	345.796	21.90	(0,0)[a]	88.7 ± 2.2	3.7×10^{-9}	4.8×10^{-17}
NGC 4736						
CI(^{3}P$_1$−^{3}P$_0$)	492.162	14.55	(0,0)[a]	8.3 ± 2.0	1.0×10^{-9}	5.7×10^{-18}
^{13}CO(2−1)	220.399	30.50	(0,0)[a]	2.2 ± 0.6	2.4×10^{-11}	5.9×10^{-19}
		30.50	(40,0)	0.9 ± 0.2	1.1×10^{-11}	2.5×10^{-19}
^{12}CO(3−2)	345.796	21.90	(0,0)[a]	32.0 ± 2.3	1.4×10^{-9}	1.7×10^{-17}
		21.90	(40,0)	14.8 ± 0.8	6.3×10^{-10}	8.0×10^{-18}
^{13}CO(3−2)	330.588	21.90	(0,0)[a]	0.9 ± 0.4	3.2×10^{-11}	4.1×10^{-19}
NGC 6090						
CI(^{3}P$_1$−^{3}P$_0$)	492.162	14.55	(0,0)[a]	5.5 ± 0.9	6.8×10^{-10}	3.8×10^{-18}
^{12}CO(2−1)	230.538	30.50	(0,0)[a]	13.8 ± 1.1	1.7×10^{-10}	4.3×10^{-18}
^{12}CO(3−2)	345.796	21.90	(0,0)[a]	38.6 ± 1.6	1.6×10^{-9}	2.1×10^{-17}
NGC 6946						
CI(^{3}P$_1$−^{3}P$_0$)	492.162	14.55	(0,0)[a]	20.0 ± 2.4	2.4×10^{-9}	1.4×10^{-17}
		14.55	(20,0)	24.6 ± 3.0	3.0×10^{-9}	1.7×10^{-17}

Table B.1. continued.

Transition	Freq (GHz)	beam size(″)	offset position(″)	$\int(T_{\rm mb}{\rm d}v)$ (K km s^{-1})	Intensity (Wm^{-2}sr^{-1})	Flux (Wm^{-2})
		14.55	(60,0)	9.2 ± 2.2	1.1×10^{-9}	6.4×10^{-18}
		14.55	(110,100)[a]	4.3 ± 0.9	5.3×10^{-10}	3.0×10^{-18}
		14.55	(150,−20)[a]	4.0 ± 0.9	4.8×10^{-10}	2.7×10^{-18}
^{12}CO(2−1)	230.538	30.50	(0,0)[a]	104.7 ± 2.8	1.3×10^{-9}	3.3×10^{-17}
		30.50	(90,90)	6.9 ± 2.0	8.7×10^{-11}	2.2×10^{-18}
		30.50	(90,120)	6.8 ± 1.3	8.5×10^{-11}	2.1×10^{-18}
		30.50	(90,150)	5.3 ± 1.5	6.6×10^{-11}	1.6×10^{-18}
		30.50	(120,−30)	10.8 ± 2.8	1.4×10^{-10}	3.3×10^{-18}
		30.50	(120,0)	4.8 ± 1.3	6.0×10^{-11}	1.5×10^{-18}
		30.50	(150,−30)	8.3 ± 1.7	1.0×10^{-10}	2.6×10^{-18}
		30.50	(150,0)	6.5 ± 1.4	8.2×10^{-11}	2.0×10^{-18}
		30.50	(180,−30)	5.3 ± 1.8	6.7×10^{-11}	1.7×10^{-18}
^{12}CO(3−2)	345.796	21.90	(0,−10)	90.0 ± 2.0	3.8×10^{-9}	4.9×10^{-17}
		21.90	(0,0)[a]	113.3 ± 2.8	4.7×10^{-9}	6.0×10^{-17}
		21.90	(10,0)	134.9 ± 2.1	5.7×10^{-9}	7.3×10^{-17}
		21.90	(100,90)	7.2 ± 1.3	3.1×10^{-10}	3.9×10^{-18}
		21.90	(100,100)	9.7 ± 2.1	4.1×10^{-10}	5.3×10^{-18}
		21.90	(100,110)[a]	6.6 ± 1.3	2.8×10^{-10}	3.6×10^{-18}
		21.90	(110,80)	2.9 ± 0.9	1.2×10^{-10}	1.5×10^{-18}
		21.90	(110,100)	14.7 ± 1.7	6.2×10^{-10}	7.9×10^{-18}
		21.90	(110,110)	19.0 ± 2.4	8.0×10^{-10}	1.0×10^{-17}
		21.90	(140,−20)	33.7 ± 3.4	1.4×10^{-9}	1.8×10^{-17}
		21.90	(150,−30)	45.11 ± 1.7	1.9×10^{-9}	2.4×10^{-17}
		21.90	(150,−20)[a]	9.0 ± 1.6	3.8×10^{-10}	4.9×10^{-18}
		21.90	(150,−10)	10.2 ± 1.7	4.3×10^{-10}	5.5×10^{-18}
		21.90	(150,0)	8.1 ± 1.1	3.4×10^{-10}	4.4×10^{-18}
		21.90	(160,−20)	9.2 ± 1.5	3.9×10^{-10}	5.0×10^{-18}
^{13}CO(3−2)	330.588	21.90	(0,0)[a]	7.9 ± 0.8	2.9×10^{-10}	3.8×10^{-18}
^{12}CO(4−3)	461.041	14.55	(0,0)[a]	194.1 ± 5.7	1.9×10^{-8}	1.1×10^{-16}
		14.55	(110,100)[a]	9.2 ± 1.3	9.2×10^{-10}	5.2×10^{-18}
		14.55	(150,−20)[a]	14.4 ± 2.3	1.4×10^{-9}	8.1×10^{-18}
^{12}CO(6−5)	691.473	10.60	(0,0)[a]	70.1 ± 10.4	2.4×10^{-8}	7.1×10^{-17}
		10.60	(0,10)	51.8 ± 12.7	1.8×10^{-8}	5.2×10^{-17}
		10.60	(5,−10)	111.4 ± 23.0	3.8×10^{-8}	1.1×10^{-16}
		10.60	(5,0)	90.7 ± 9.8	3.1×10^{-8}	9.2×10^{-17}
		10.60	(5,5)	102.4 ± 16.8	3.5×10^{-8}	1.0×10^{-16}
		10.60	(5,10)	83.3 ± 11.7	2.8×10^{-8}	8.4×10^{-17}
		10.60	(5,15)	129.4 ± 55.1	4.4×10^{-8}	1.3×10^{-16}
		10.60	(10,0)	152.4 ± 23.7	5.2×10^{-8}	1.5×10^{-16}
		10.60	(10,10)	181.5 ± 53.7	6.1×10^{-8}	1.8×10^{-16}

Table B.2. Results of the Gaussian fits derived from spectra of the Antennae (NGC 4038 et Overlap), Henize 2-10, IC 10, IC 342, M 83, NGC 253 and NGC 6946. See caption of Table B.1. Data listed in this table are either from literature or from our sample of observations.

Transition	Freq (GHz)	beam size(")	offset position(")	$\int(T_{\rm mb}{\rm d}v)$ (K km s^{-1})	Intensity (Wm^{-2}sr^{-1})	Flux (Wm^{-2})	Ref. [a]
Antennae NGC4038							
CI(^{3}P$_1$−^{3}P$_0$)	492.162	14.55	(0,0)	13.7 ± 2.1	1.7×10^{-9}	9.4×10^{-18}	1
		21.90	(0,0)	7.6 ± 1.2	9.2×10^{-10}	1.2×10^{-17}	1*
^{12}CO(1−0)	115.271	43.00	(0,0)	21.0 ± 2.0	3.3×10^{-11}	1.6×10^{-18}	2
		6.75	(0,0)	415.0 ± 83.0	6.5×10^{-10}	7.9×10^{-19}	3
		21.90	(0,0)	112.1 ± 22.4	1.8×10^{-10}	2.2×10^{-18}	3
		55.00	(0,0)	19.5 ± 3.9	3.1×10^{-11}	2.5×10^{-18}	6
		15.00	(0,0)	80.0 ± 16.0	1.3×10^{-10}	7.5×10^{-19}	4
		21.90	(0,0)	45.9 ± 9.2	7.2×10^{-11}	9.2×10^{-19}	4*
^{12}CO(2−1)	230.538	30.50	(0,0)	35.6 ± 1.3	4.5×10^{-10}	1.1×10^{-17}	5
		20.00	(0,0)	59.1 ± 11.8	7.4×10^{-10}	7.9×10^{-18}	4
		21.90	(0,0)	51.3 ± 10.3	6.4×10^{-10}	8.2×10^{-18}	4*
		30.50	(0,0)	31.3 ± 6.3	3.9×10^{-10}	9.7×10^{-18}	7
^{12}CO(3−2)	345.796	21.90	(0,0)	37.2 ± 1.7	1.6×10^{-9}	2.0×10^{-17}	5*

Table B.2. continued.

Transition	Freq (GHz)	beam size(")	offset position(")	$\int(T_{\rm mb}{\rm d}v)$ (K km s^{-1})	Intensity (Wm^{-2}sr^{-1})	Flux (Wm^{-2})	Ref. [a]
		14.00	(0,0)	56.1 ± 11.2	2.4×10^{-9}	1.2×10^{-17}	4
		21.90	(0,0)	29.4 ± 5.9	1.2×10^{-9}	1.6×10^{-17}	4
^{12}CO(4−3)	461.041	14.55	(0,0)	45.3 ± 3.5	4.5×10^{-9}	2.6×10^{-17}	5
		21.90	(0,0)	25.0 ± 1.9	2.5×10^{-9}	3.2×10^{-17}	5*
^{12}CO(6−5)	691.473	10.60	(3,3)	85.5 ± 10.4	2.9×10^{-8}	8.7×10^{-17}	5
		21.90	(3,3)	32.8 ± 4.0	1.1×10^{-8}	1.4×10^{-16}	5*
^{12}CO(7−6)	806.652	8.95	(3,3)	4.9 ± 1.3	2.6×10^{-9}	5.6×10^{-18}	5
		21.90	(3,3)	1.6 ± 0.4	8.7×10^{-10}	1.1×10^{-17}	5*
^{13}CO(2−1)	220.399	20.00	(0,0)	2.4 ± 0.5	2.7×10^{-11}	2.8×10^{-19}	4*
		21.90	(0,0)	2.1 ± 0.4	2.3×10^{-11}	2.9×10^{-19}	4
		30.50	(0,0)	2.4 ± 0.5	2.6×10^{-11}	6.5×10^{-19}	7
^{13}CO(3−2)	330.588	21.90	(0,0)	2.1 ± 1.2	7.6×10^{-11}	9.8×10^{-19}	5*
		14.00	(0,0)	4.5 ± 0.9	1.7×10^{-10}	8.7×10^{-19}	4
		21.90	(0,0)	2.4 ± 0.5	8.7×10^{-11}	1.1×10^{-18}	4
Antennae Overlap							
CI(^{3}P$_1$−^{3}P$_0$)	492.162	14.55	(0,0)	11.2 ± 1.5	1.4×10^{-9}	7.7×10^{-18}	1
		21.90	(0,0)	5.8 ± 0.8	7.1×10^{-10}	9.1×10^{-18}	1*
^{12}CO(1−0)	115.271	6.75	(0,0)	721.4 ± 144.3	1.1×10^{-9}	1.4×10^{-18}	2
		21.9	(0,0)	163.4 ± 32.7	2.6×10^{-10}	3.3×10^{-18}	2
		43.00	(0,0)	22.0 ± 2.0	3.4×10^{-11}	1.7×10^{-18}	3
		15.00	(0,0)	128.0 ± 25.6	2.0×10^{-10}	1.2×10^{-18}	4
		21.90	(0,0)	70.0 ± 14.0	1.1×10^{-10}	1.4×10^{-18}	4*
		55.00	(0,0)	19.2 ± 3.8	3.0×10^{-11}	2.4×10^{-18}	6
^{12}CO(2−1)	230.538	30.50	(0,0)	58.3 ± 2.6	7.3×10^{-10}	1.8×10^{-17}	5
		20.00	(0,0)	87.9 ± 17.6	1.1×10^{-9}	1.2×10^{-17}	4
		21.90	(0,0)	75.4 ± 15.1	9.5×10^{-10}	1.2×10^{-17}	4*
		30.50	(0,0)	61.2 ± 12.2	7.7×10^{-10}	1.9×10^{-17}	7
^{12}CO(3−2)	345.796	21.90	(0,0)	56.8 ± 3.5	2.4×10^{-9}	3.1×10^{-17}	5*
		14.00	(0,0)	70.3 ± 14.1	3.0×10^{-9}	1.6×10^{-17}	4
		21.90	(0,0)	34.8 ± 7.0	1.5×10^{-9}	1.9×10^{-17}	4
^{12}CO(4−3)	461.041	14.55	(0,0)	45.1 ± 2.5	4.5×10^{-9}	2.5×10^{-17}	5
		21.90	(0,0)	23.6 ± 1.3	2.4×10^{-9}	3.0×10^{-17}	5*
^{12}CO(6−5)	691.473	10.60	(3,3)	97.0 ± 37.1	3.3×10^{-8}	9.8×10^{-17}	5
		21.90	(3,3)	33.6 ± 12.8	1.1×10^{-8}	1.4×10^{-16}	5*
^{12}CO(7−6)	806.652	8.95	(3,3)	13.4 ± 1.6	7.2×10^{-9}	1.5×10^{-17}	5
		21.90	(3,3)	3.9 ± 0.5	2.1×10^{-9}	2.7×10^{-17}	5*
^{13}CO(2−1)	220.399	20.00	(0,0)	5.4 ± 1.1	5.9×10^{-11}	6.3×10^{-19}	4
		21.90	(0,0)	4.6 ± 0.9	5.1×10^{-11}	6.5×10^{-19}	4*
		30.50	(0,0)	3.3 ± 0.7	3.6×10^{-11}	9.0×10^{-19}	7
^{13}CO(3−2)	330.588	14.00	(0,0)	3.8 ± 0.8	1.4×10^{-10}	7.3×10^{-19}	4
		21.90	(0,0)	1.9 ± 0.4	7.0×10^{-11}	8.9×10^{-19}	4*
HENIZE 2-10							
CI(^{3}P$_1$−^{3}P$_0$)	492.162	14.55	(0,0)	4.2 ± 0.8	5.1×10^{-10}	2.9×10^{-18}	4 et 5
		21.90	(0,0)	2.5 ± 0.5	3.0×10^{-10}	3.8×10^{-18}	4 et 5*
^{12}CO(1−0)	115.271	40.0	(0,0)	10.0 ± 0.8	1.6×10^{-11}	6.7×10^{-19}	1
		21.90	(0,0)	27.3 ± 2.2	4.3×10^{-11}	5.5×10^{-19}	1
		55.00	(0,0)	4.9 ± 0.2	7.7×10^{-12}	6.2×10^{-19}	2
		21.90	(0,0)	24.1 ± 1.0	3.8×10^{-11}	4.8×10^{-19}	2*
^{12}CO(2−1)	230.538	21.00	(0,0)	17.3 ± 1.4	2.2×10^{-10}	2.5×10^{-18}	1*
		27.00	(0,0)	6.8 ± 0.8	8.5×10^{-11}	1.7×10^{-18}	2
		21.90	(0,0)	9.4 ± 1.1	1.2×10^{-10}	1.5×10^{-18}	2
^{12}CO(3−2)	345.796	21.90	(0,0)	11.5 ± 2.3	4.9×10^{-10}	6.2×10^{-18}	5*
		21.00	(0,0)	23.2 ± 2.1	9.8×10^{-10}	1.2×10^{-17}	1
		22.00	(0,0)	16.6 ± 0.6	7.0×10^{-10}	9.0×10^{-18}	3
^{12}CO(4−3)	461.041	14.55	(0,0)	18.6 ± 4.2	1.9×10^{-9}	1.1×10^{-17}	5
		21.90	(0,0)	10.9 ± 2.4	1.1×10^{-9}	1.4×10^{-17}	5*
^{12}CO(6−5)	691.473	10.60	(0,0)	15.7 ± 3.1	5.3×10^{-9}	1.6×10^{-17}	5
		21.90	(0,0)	6.8 ± 1.3	2.3×10^{-9}	2.9×10^{-17}	5*
^{12}CO(7−6)	806.652	8.95	(0,0)	15.2 ± 3.0	8.2×10^{-9}	1.7×10^{-17}	5
		21.90	(0,0)	5.8 ± 1.2	3.1×10^{-9}	4.0×10^{-17}	5*
^{13}CO(1−0)	110.201	57.00	(0,0)	0.3 ± 0.1	4.1×10^{-13}	3.6×10^{-20}	2
		21.90	(0,0)	1.6 ± 0.5	2.2×10^{-12}	2.8×10^{-20}	2*

Table B.2. continued.

Transition	Freq (GHz)	beam size(")	offset position(")	$\int(T_{\rm mb}{\rm d}v)$ (K km s^{-1})	Intensity (Wm^{-2}sr^{-1})	Flux (Wm^{-2})	Ref. [a]
		40.00	(0,0)	<0.5	$<6.8\times10^{-13}$	$<2.9\times10^{-20}$	1
		21.90	(0,0)	<	$<\times10^{-12}$	$<\times10^{-20}$	1
^{13}CO(2−1)	220.399	21.00	(0,0)	0.9 ± 0.2	9.9×10^{-12}	1.2×10^{-19}	1*
^{13}CO(3−2)	330.588	21.90	(0,0)	1.8 ± 0.5	6.7×10^{-11}	8.5×10^{-19}	5
		14.00	(0,0)	2.3 ± 0.6	8.5×10^{-11}	4.4×10^{-19}	1
		21.90	(0,0)	1.3 ± 0.3	4.8×10^{-11}	6.1×10^{-19}	1*
IC 10							
CI(^{3}P$_1$−^{3}P$_0$)	492.162	14.55	(5,10)	5.5 ± 0.6	6.8×10^{-10}	3.8×10^{-18}	1
		21.90	(5,10)	3.3 ± 0.4	4.1×10^{-10}	5.2×10^{-18}	1*
		10.80	(0,−3)	2.2 ± 0.5	2.7×10^{-10}	8.4×10^{-19}	2
		21.90	(0,−3)	1.0 ± 0.2	1.2×10^{-10}	1.6×10^{-18}	2*
CI(^{3}P$_2$−^{3}P$_1$)	809.902	8.95	(0,30)	3.0 ± 0.7	1.6×10^{-9}	3.5×10^{-18}	3
		21.90	(0,30)	1.2 ± 0.3	6.6×10^{-10}	8.4×10^{-18}	3*
^{12}CO(1−0)	115.271	22.0	(5,10)	22.8 ± 4.6	3.6×10^{-11}	4.6×10^{-19}	4*
^{12}CO(2−1)	230.538	30.50	(10,0)	26.1 ± 0.2	3.3×10^{-10}	8.1×10^{-18}	3
		21.90	(10,0)	43.7 ± 0.3	5.5×10^{-10}	7.0×10^{-18}	3
		12.50	(5,0)	33.9 ± 6.8	4.2×10^{-10}	1.8×10^{-18}	4
		21.90	(5,0)	17.5 ± 3.5	2.2×10^{-10}	2.8×10^{-18}	4
		22.00	(2.2,10)	15.7 ± 3.1	2.0×10^{-10}	2.5×10^{-18}	5*
		30.50	(0,30)	5.5 ± 1.1	6.9×10^{-11}	1.7×10^{-18}	6
		21.90	(0,30)	9.2 ± 1.8	1.2×10^{-10}	1.5×10^{-18}	6
^{12}CO(3−2)	345.796	21.90	(5,10)	12.7 ± 0.6	5.4×10^{-10}	6.9×10^{-18}	3*
		22.00	(2.2,10)	16.3 ± 3.3	6.9×10^{-10}	8.9×10^{-18}	5
		13.20	(0,−3)	14.9 ± 0.6	6.3×10^{-10}	2.9×10^{-18}	2
		21.90	(0,−3)	8.1 ± 0.3	3.4×10^{-10}	4.4×10^{-18}	2
^{12}CO(4−3)	461.041	14.55	(15,0)	11.6 ± 1.2	1.2×10^{-9}	6.6×10^{-18}	3
		21.90	(15,0)	7.0 ± 0.7	7.0×10^{-10}	8.9×10^{-18}	3*
^{12}CO(6−5)	691.473	10.60	(5,10)	11.2 ± 1.7	3.8×10^{-9}	1.1×10^{-17}	3
		21.90	(5,10)	5.1 ± 0.8	1.7×10^{-9}	2.2×10^{-17}	3*
^{12}CO(7−6)	806.652	8.95	(0,30)	3.6 ± 0.8	1.9×10^{-9}	4.2×10^{-18}	3
		21.90	(0,30)	1.5 ± 0.3	7.9×10^{-10}	1.0×10^{-17}	3*
^{13}CO(2−1)	220.399	30.50	(0,30)	0.4 ± 0.1	4.3×10^{-12}	1.1×10^{-19}	1
		21.90	(0,30)	0.7 ± 0.2	7.3×10^{-12}	9.4×10^{-20}	1
		22.00	(2.2,10)	1.0 ± 0.2	1.1×10^{-11}	1.4×10^{-19}	5*
^{13}CO(3−2)	330.588	15.00	(2.2,10)	4.4 ± 0.9	1.6×10^{-10}	9.6×10^{-19}	5
		21.90	(2.2,10)	2.7 ± 0.6	1.0×10^{-10}	1.3×10^{-18}	5
		13.20	(0,−3)	2.5 ± 0.6	9.2×10^{-11}	4.3×10^{-19}	2
		21.90	(0,−3)	1.4 ± 0.3	5.0×10^{-11}	6.4×10^{-19}	2
		21.90	(0,10)	1.2 ± 0.2	4.6×10^{-11}	5.9×10^{-19}	3*
IC 342							
CI(^{3}P$_1$−^{3}P$_0$)	492.162	10.00	(0,0)	54.0 ± 6.0	6.6×10^{-9}	1.8×10^{-17}	1
		21.90	(0,0)	12.0 ± 1.3	1.5×10^{-9}	1.9×10^{-17}	1*
CI(^{3}P$_2$−^{3}P$_1$)	809.902	8.95	(5,0)	49.8 ± 6.3	2.7×10^{-8}	5.8×10^{-17}	2
		21.90	(5,0)	9.1 ± 1.1	4.9×10^{-9}	6.3×10^{-17}	2*
^{12}CO(1−0)	115.271	21.00	(0,0)	213.2 ± 2.1	3.3×10^{-10}	3.9×10^{-18}	3*
^{12}CO(2−1)	230.538	14.00	(0,0)	324.3 ± 64.8	4.1×10^{-9}	2.1×10^{-17}	3
		21.90	(0,0)	135.9 ± 27.2	1.7×10^{-9}	2.2×10^{-17}	3*
		21.00	(0,0)	172.0 ± 19.0	2.2×10^{-9}	2.5×10^{-17}	1
^{12}CO(3−2)	345.796	14.00	(0,0)	186.0 ± 23.0	7.9×10^{-9}	4.1×10^{-17}	1
		21.90	(0,0)	78.0 ± 9.6	3.3×10^{-9}	4.2×10^{-17}	1
		21.90	(0,0)	109.8 ± 2.5	4.6×10^{-9}	5.9×10^{-17}	2*
^{12}CO(4−3)	461.041	11.00	(0,0)	209.0 ± 21.0	2.1×10^{-8}	6.7×10^{-17}	1
		21.90	(0,0)	55.5 ± 5.6	5.6×10^{-9}	7.1×10^{-17}	1
		14.55	(0,0)	110.8 ± 12.6	1.1×10^{-8}	6.3×10^{-17}	2
		21.90	(0,0)	50.0 ± 5.7	5.0×10^{-9}	6.4×10^{-17}	2*
^{12}CO(6−5)	691.473	10.60	(5,0)	108.1 ± 7.0	3.7×10^{-8}	1.1×10^{-16}	2
		21.90	(5,0)	26.8 ± 1.7	9.1×10^{-9}	1.2×10^{-16}	2*
^{12}CO(7−6)	806.652	8.95	(5,0)	40.3 ± 3.5	2.2×10^{-8}	4.6×10^{-17}	2
		21.90	(5,0)	7.3 ± 0.6	3.9×10^{-9}	5.0×10^{-17}	2*
^{13}CO(1−0)	110.201	21.00	(0,0)	18.9 ± 0.5	2.6×10^{-11}	3.0×10^{-19}	3*
^{13}CO(2−1)	220.399	14.00	(0,0)	29.7 ± 1.1	3.3×10^{-10}	1.7×10^{-18}	3
		21.90	(0,0)	12.4 ± 0.5	1.4×10^{-10}	1.7×10^{-18}	3*
		21.00	(0,0)	24.0 ± 3.0	2.6×10^{-10}	3.1×10^{-18}	1
^{13}CO(3−2)	330.588	14.00	(0,0)	17.1 ± 2.0	6.3×10^{-10}	3.3×10^{-18}	1

Table B.2. continued.

Transition	Freq (GHz)	beam size(")	offset position(")	$\int(T_{\rm mb}{\rm d}v)$ (K km s^{-1})	Intensity (Wm^{-2}sr^{-1})	Flux (Wm^{-2})	Ref. [a]
		21.90	(0,0)	7.2 ± 0.8	2.6×10^{-10}	3.4×10^{-18}	1
		21.90	(0,0)	19.9 ± 2.2	7.4×10^{-10}	9.4×10^{-18}	2*
M 83							
CI(^{3}P$_1$–^{3}P$_0$)	492.162	10.00	(5,5)	78.0 ± 15.6	9.5×10^{-9}	2.5×10^{-17}	1
		21.90	(5,5)	18.7 ± 3.7	2.3×10^{-9}	2.9×10^{-17}	1*
		21.00	(0,0)	55.0 ± 8.0	6.7×10^{-9}	7.9×10^{-17}	2
^{12}CO(1–0)	115.271	24.00	(0,0)	87.7 ± 2.1	1.3×10^{-10}	2.1×10^{-18}	3*
		16.00	(0,0)	80.0 ± 16.0	1.3×10^{-10}	8.5×10^{-19}	4
		21.90	(0,0)	44.2 ± 8.8	6.9×10^{-11}	8.8×10^{-19}	4
^{12}CO(2–1)	230.538	24.00	(0,0)	98.1 ± 0.8	1.2×10^{-9}	1.9×10^{-17}	3*
		21.00	(0,0)	261.0 ± 52.2	3.3×10^{-9}	3.8×10^{-17}	2
		30.50	(0,–10)	101.8 ± 20.4	1.3×10^{-9}	3.2×10^{-17}	5
^{12}CO(3–2)	345.796	21.90	(0,0)	99.9 ± 1.6	4.2×10^{-9}	5.4×10^{-17}	5*
		14.00	(5,5)	290.0 ± 58.0	1.2×10^{-8}	6.4×10^{-17}	1
		21.90	(5,5)	125.3 ± 25.1	5.3×10^{-9}	6.8×10^{-17}	1
		21.00	(0,0)	167.0 ± 15.0	7.1×10^{-9}	8.3×10^{-17}	2
^{12}CO(4–3)	461.041	14.55	(5,5)	196.9 ± 39.4	2.0×10^{-8}	1.1×10^{-16}	5
		21.90	(5,5)	91.3 ± 18.3	9.1×10^{-9}	1.2×10^{-16}	5*
		21.00	(0,0)	122.0 ± 15.0	1.2×10^{-8}	1.4×10^{-16}	2
		11.00	(5,5)	357.0 ± 71.4	3.6×10^{-8}	1.2×10^{-16}	1
		21.90	(5,5)	100.5 ± 20.1	1.0×10^{-8}	1.3×10^{-16}	1
^{12}CO(6–5)	691.473	10.60	(–5,0)	317.5 ± 20.6	1.1×10^{-7}	3.2×10^{-16}	5
		21.90	(–5,0)	83.9 ± 5.4	2.8×10^{-8}	3.6×10^{-16}	5*
^{13}CO(2–1)	220.399	21.00	(0,0)	28.5 ± 3.0	3.1×10^{-10}	3.7×10^{-18}	2*
^{13}CO(3–2)	330.588	21.90	(0,0)	11.8 ± 1.3	1.3×10^{-10}	1.7×10^{-18}	5*
		14.00	(0,0)	22.3 ± 1.0	8.2×10^{-10}	4.3×10^{-18}	2
		21.90	(0,0)	9.6 ± 0.4	3.6×10^{-10}	4.5×10^{-18}	2
NGC 253							
CI(^{3}P$_1$–^{3}P$_0$)	492.162	22.00	(0,0)	290.0 ± 45.0	3.5×10^{-8}	4.6×10^{-16}	10*
		10.20	(0,0)	575.0 ± 115.0	7.0×10^{-8}	1.9×10^{-16}	5
		21.90	(0,0)	210.5 ± 42.1	2.6×10^{-8}	3.3×10^{-16}	5
		43.00	(0,0)	98.0 ± 19.6	1.2×10^{-8}	5.9×10^{-16}	5
		23.00	(0,0)	320.0 ± 64.0	3.9×10^{-8}	5.5×10^{-16}	4
CI(^{3}P$_2$–^{3}P$_1$)	809.902	8.95	(0,0)	188.5 ± 37.7	1.0×10^{-7}	2.2×10^{-16}	11
		21.90	(0,0)	59.8 ± 12.0	3.3×10^{-8}	4.2×10^{-16}	11*
^{12}CO(1–0)	115.271	43.00	(0,0)	343.0 ± 68.6	5.4×10^{-10}	2.6×10^{-17}	2
		23.00	(0,0)	920.0 ± 82.8	1.4×10^{-9}	2.0×10^{-17}	6*
^{12}CO(2–1)	230.538	23.00	(0,0)	1062.0 ± 116.8	1.3×10^{-8}	1.9×10^{-16}	7*
		21.00	(0,0)	926.0 ± 185.2	1.2×10^{-8}	1.4×10^{-16}	2
^{12}CO(3–2)	345.796	21.90	(0,0)	815.6 ± 163.1	3.4×10^{-8}	4.4×10^{-16}	11*
		23.00	(0,0)	998.0 ± 139.7	4.2×10^{-8}	5.9×10^{-16}	7
		23.00	(0,0)	1194.0 ± 238.8	5.0×10^{-8}	7.1×10^{-16}	2
		14.00	(0,0)	1200.0 ± 240.0	5.1×10^{-8}	2.6×10^{-16}	5
		21.90	(0,0)	642.3 ± 128.5	2.7×10^{-8}	3.5×10^{-16}	5
		22.00	(0,0)	680.0 ± 60.0	2.9×10^{-8}	3.7×10^{-16}	8
^{12}CO(4–3)	461.041	15.00	(0,0)	507.0 ± 101.4	5.1×10^{-8}	3.0×10^{-16}	3
		21.90	(0,0)	296.8 ± 59.4	3.0×10^{-8}	3.8×10^{-16}	3
		22.00	(0,0)	1019.0 ± 120.0	1.0×10^{-7}	1.3×10^{-15}	9*
		10.40	(0,0)	2160.0 ± 432.0	2.2×10^{-7}	6.2×10^{-16}	5
		21.90	(0,0)	808.4 ± 161.7	8.1×10^{-8}	1.0×10^{-15}	5
^{12}CO(6–5)	691.473	10.60	(0,0)	1394.0 ± 278.8	4.7×10^{-7}	1.4×10^{-15}	11
		21.90	(0,0)	533.1 ± 106.6	1.8×10^{-7}	2.3×10^{-15}	11*
		8/30	(0,0)	861 ± 258.3	2.9×10^{-7}	5.0×10^{-15}	1
^{12}CO(7–6)	806.652	8.95	(0,0)	810.2 ± 162.0	4.3×10^{-7}	9.3×10^{-16}	11
		21.90	(0,0)	257.2 ± 51.4	1.4×10^{-7}	1.8×10^{-15}	11*
		11.5/60	(0,0)	1370 ± 411	7.3×10^{-7}	2.6×10^{-15}	10
^{13}CO(1–0)	110.201	23.00	(0,0)	80.0 ± 8.0	1.1×10^{-10}	1.5×10^{-18}	7*
^{13}CO(2–1)	220.399	23.00	(0,0)	82.0 ± 9.8	9.0×10^{-10}	1.3×10^{-17}	7*
		21.00	(0,0)	104.0 ± 20.8	1.1×10^{-9}	1.3×10^{-17}	2
^{13}CO(3–2)	330.588	23.00	(0,0)	90.0 ± 12.6	3.3×10^{-9}	4.7×10^{-17}	7*
		23.00	(0,0)	210.0 ± 42.0	7.8×10^{-9}	1.1×10^{-16}	2
NGC 6946							
CI(^{3}P$_1$–^{3}P$_0$)	492.162	21.00	(0,0)	44.0 ± 8.0	5.4×10^{-9}	6.3×10^{-17}	1
		14.55	(20,0)	24.6 ± 3.0	3.0×10^{-9}	1.7×10^{-17}	2

Table B.2. continued.

Transition	Freq (GHz)	beam size(")	offset position(")	$\int(T_{\rm mb}{\rm d}v)$ (K km s^{-1})	Intensity (Wm^{-2}sr^{-1})	Flux (Wm^{-2})	Ref. [a]
		21.90	(20,0)	11.3 ± 1.4	1.4×10^{-9}	1.8×10^{-17}	2*
^{12}CO(1−0)	115.271	21.00	(0,0)	198.1 ± 39.6	3.1×10^{-10}	3.6×10^{-18}	3*
		5.65	(0,0)	945.0 ± 189.0	1.5×10^{-9}	1.3×10^{-18}	4
		21.90	(0,0)	93.5 ± 18.7	1.5×10^{-10}	1.9×10^{-18}	4
		23.00	(0,0)	189.8 ± 38.0	3.0×10^{-10}	4.2×10^{-18}	5
		17.00	(0,0)	227.4 ± 45.5	3.6×10^{-10}	2.7×10^{-18}	6
		21.90	(0,0)	140.2 ± 28.0	2.2×10^{-10}	2.8×10^{-18}	6
		23.00	(0,0)	169.7 ± 33.9	2.7×10^{-10}	3.7×10^{-18}	7
^{12}CO(2−1)	230.538	30.50	(0,0)	104.7 ± 2.8	1.3×10^{-9}	3.3×10^{-17}	8
		21.90	(0,0)	199.7 ± 5.3	2.5×10^{-9}	3.2×10^{-17}	8*
		21.00	(0,0)	222.0 ± 20.0	2.8×10^{-9}	3.3×10^{-17}	1
		14.00	(0,0)	170.0 ± 34.0	2.1×10^{-9}	1.1×10^{-17}	9
		21.90	(0,0)	73.0 ± 14.6	9.1×10^{-10}	1.2×10^{-17}	9
		14.00	(0,0)	178.3 ± 35.7	2.2×10^{-9}	1.2×10^{-17}	7
		21.90	(0,0)	76.5 ± 15.3	9.6×10^{-10}	1.2×10^{-17}	7
^{12}CO(3−2)	345.796	22.00	(0,0)	129.1 ± 25.2	5.5×10^{-9}	7.0×10^{-17}	3
		21.00	(0,0)	145.0 ± 15.0	6.1×10^{-9}	7.2×10^{-17}	1
		21.90	(0,0)	200.0 ± 40.0	8.5×10^{-9}	1.1×10^{-16}	10
		21.90	(10,0)	134.9 ± 2.1	5.7×10^{-9}	7.3×10^{-17}	8*
		22.00	(0,0)	46.0 ± 2.0	1.9×10^{-9}	2.5×10^{-17}	11
^{12}CO(4−3)	461.041	17.00	(0,0)	82.4 ± 16.5	8.3×10^{-9}	6.4×10^{-17}	12
		21.90	(0,0)	50.8 ± 10.2	5.1×10^{-9}	6.5×10^{-17}	12
		21.00	(0,0)	112.0 ± 11.0	1.1×10^{-8}	1.3×10^{-16}	1
		17.00	(0,0)	155.4 ± 31.1	1.6×10^{-8}	1.2×10^{-16}	3
		21.90	(0,0)	95.8 ± 19.2	9.6×10^{-9}	1.2×10^{-16}	3
		14.55	(0,0)	194.1 ± 38.8	1.9×10^{-8}	1.1×10^{-16}	8
		21.90	(0,0)	89.4 ± 17.9	9.0×10^{-9}	1.1×10^{-16}	8*
^{12}CO(6−5)	691.473	10.60	(5,−10)	111.4 ± 23.0	3.8×10^{-8}	1.1×10^{-16}	8
		21.90	(5,−10)	29.1 ± 6.0	9.8×10^{-9}	1.3×10^{-16}	8*
^{13}CO(1−0)	110.201	21.00	(0,0)	17.9 ± 3.6	2.4×10^{-11}	2.9×10^{-19}	3*
^{13}CO(2−1)	220.399	12.00	(0,0)	20.7 ± 4.1	2.3×10^{-10}	8.7×10^{-19}	3
		21.90	(0,0)	6.7 ± 1.3	7.4×10^{-11}	9.4×10^{-19}	3*
		14.00	(0,0)	22.2 ± 3.0	2.4×10^{-10}	1.3×10^{-18}	1
		21.90	(0,0)	9.5 ± 1.3	1.0×10^{-10}	1.3×10^{-18}	1
^{13}CO(3−2)	330.588	22.00	(0,0)	5.6 ± 1.1	6.1×10^{-11}	7.9×10^{-19}	3
		14.00	(0,0)	11.4 ± 2.0	4.2×10^{-10}	2.2×10^{-18}	1
		21.90	(0,0)	4.9 ± 0.9	1.8×10^{-10}	2.3×10^{-18}	1
		21.90	(0,0)	28.0 ± 5.6	1.0×10^{-9}	1.3×10^{-17}	10
		21.90	(0,0)	7.9 ± 0.8	2.9×10^{-10}	3.7×10^{-18}	8*

[a] References: NGC 4038: 1: Gerin & Phillips (2000) but spectra have been analyzed again; 2: Aalto et al. (1995); 3: Stanford et al. (1990); 4: Zhu et al. (2003); 5: Our work; 6: Gao et al. (2001); 7: Glenn & Hunter (2001); *: used for constraining the models and for computing the C and CO cooling rates.
Overlap: 1: Gerin & Phillips (2000) but spectra have been analyzed again; 2: Stanford et al. (1990); 3: Aalto et al. (1995); 4: Zhu et al. (2003); 5: Our work; 6: Gao et al. (2001); 7: Glenn & Hunter (2001); *: used for constraining the models and for computing the C and CO cooling rates.
HENIZE 2-10: 1: Baas et al. (1994); 2: Kobulnicky et al. (1995); 3: Meier et al. (2001); 4: Gerin & Phillips (2000) but spectra have been analyzed again; 5: Bayet et al. (2004) ; *: used for constraining the models and for computing the C and CO cooling rates (see Bayet et al. (2004)).
IC 10: 1: Gerin & Phillips (2000) but spectra have been analyzed again; 2: Bolatto et al. (2000); 3: Our work; 4: PhD Thesis of Becker (1990); 5: Petitpas & Wilson (1998a); 6: Glenn & Hunter (2001); *: used for constraining the models and for computing the C and CO cooling rates.
IC 342: 1: Israel & Baas (2003); 2: Our work; 3: Eckart et al. (1990); *: used for constraining the models and for computing the C and CO cooling rates.
M 83: 1: Petitpas & Wilson (1998b); 2: Israel & Baas (2001); 3: Lundgren et al. (2004); 4: Handa et al. (1990); 5: Our work; *: used for constraining the models and for computing the C and CO cooling rates.
NGC 253: 1: Harris et al. (1991); 2: Wall et al. (1991); 3: Guesten et al. (1993); 4: Harrison et al. (1995); 5: Israel et al. (1995); 6: Mauersberger et al. (1996); 7: Harrison et al. (1999); 8: Dumke et al. (2001); 9: Israel & Baas (2002); 10: Bradford et al. (2003); 11: Bayet et al. (2004); *: used for constraining the models and for computing the C and CO cooling rates (see Bayet et al. (2004)).
NGC 6946: 1: Israel & Baas (2001); 2: Gerin & Phillips (2000) but spectra have been analyzed again; 3: Walsh et al. (2002); 4: Ishizuki et al. (1990); 5: Weliachew et al. (1988); 6: Sofue et al. (1988); 7: Casoli et al. (1990); 8: Our work; 9: Clausset et al. (1991); 10: Wall et al. (1993); 11: Mauersberger et al. (1999); 12: Nieten et al. (1999); *: used for constraining the models and for computing the C and CO cooling rates.

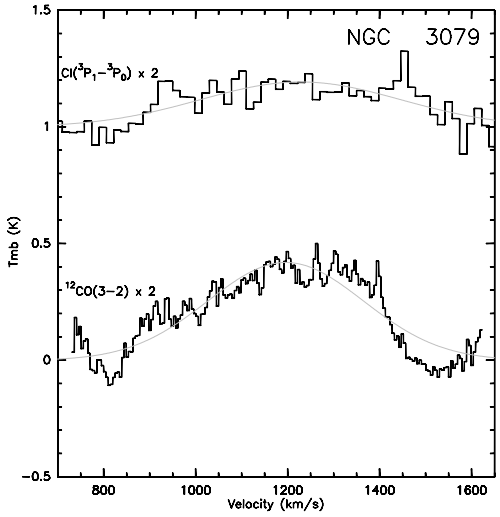

Fig. 4. Observed spectra towards NGC 3079 nucleus (see Table B.1). See the caption of Fig. 1.

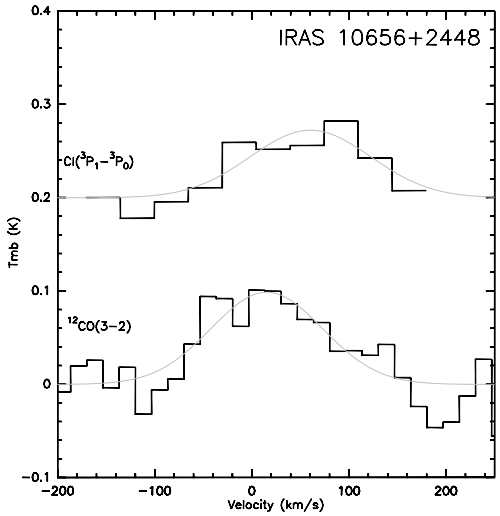

Fig. 5. Observed spectra towards IRAS 10565+2448 nucleus (see Table B.1). See the caption of Fig. 1.

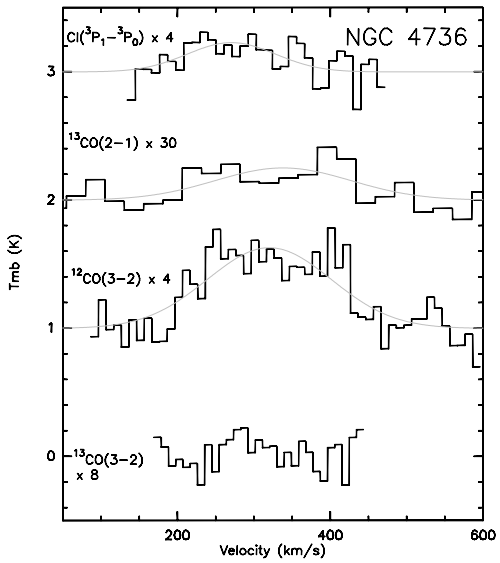

Fig. 8. Observed spectra towards NGC 4736 nucleus (see Table B.1). See the caption of Fig. 1.

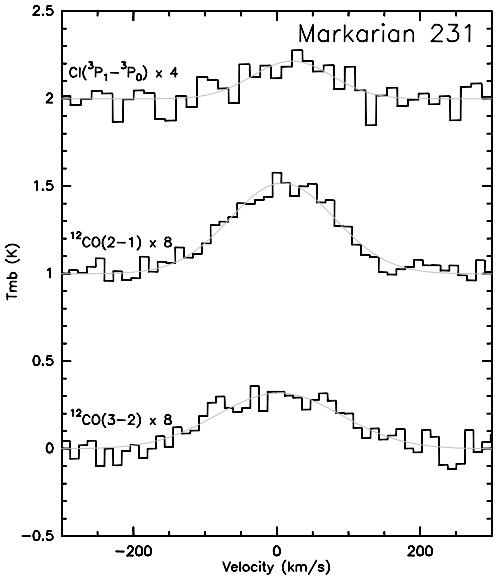

Fig. 9. Observed spectra towards Markarian 231 nucleus (see Table B.1). See the caption of Fig. 1.

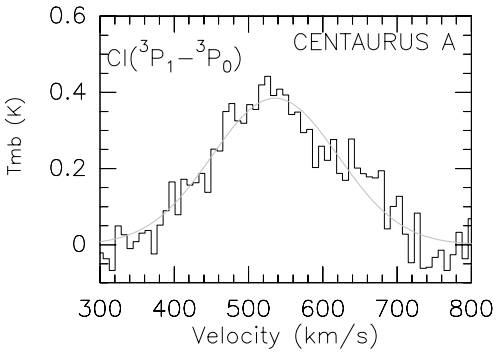

Fig. 10. Observed spectra towards Centaurus A nucleus (see Table B.1). See the caption of Fig. 1.

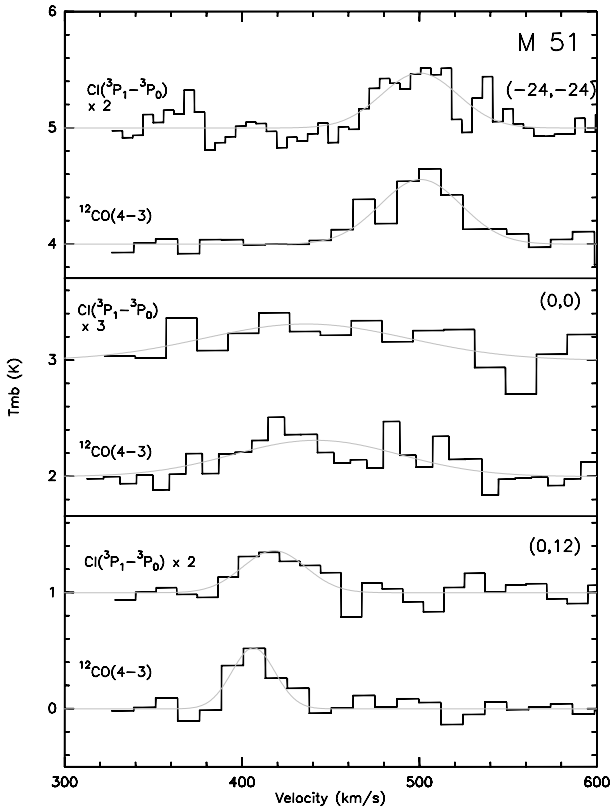

Fig. 11. Spectra of M 51 at various offset positions relative to the central position (0″, 0″,) given in Table 1 (see also Table B.1) : (–24″, −24″) (*top*), (0″, 0″) (*middle*) and (0″, 12″) (*bottom*). See the caption of Fig. 1. The [CI]($^3P_1$−$^3P_0$) spectrum at the central position (0″, 0″) is from Gerin & Phillips (2000) but it has been analyzed again to obtain an homogeneous dataset of observations.

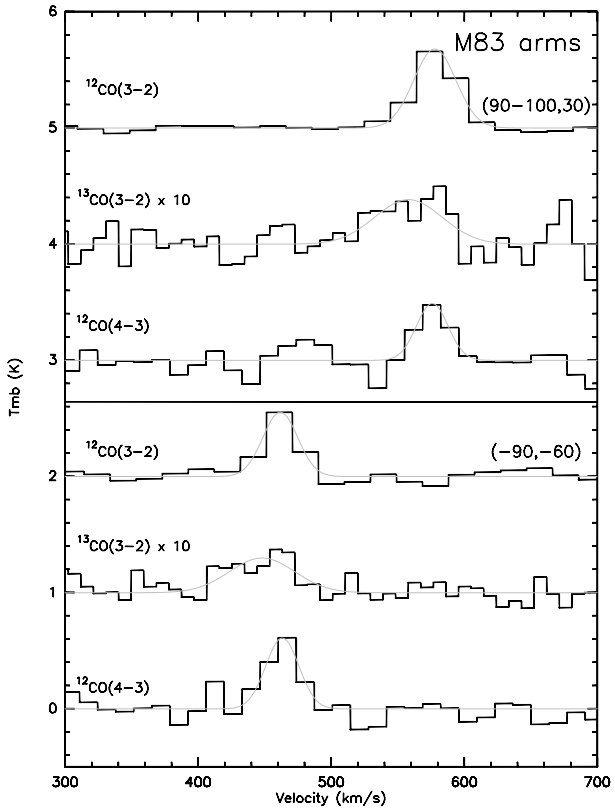

Fig. 15. Spectra taken in the M 83 arms at the offset positions (90″ – 100″, 30″) (*top*) and (−90″, −60″) (*bottom*) (relative to the central position (0″, 0″) listed in Table 1, see also Table B.1). See the caption of Fig. 1.

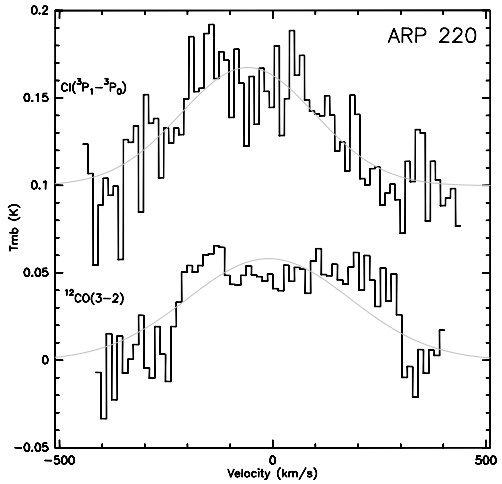

Fig. 13. Observed spectra towards Arp 220 nucleus (see Table B.1). See the caption of Fig. 1. In this figure, both spectra are from Gerin & Phillips (1998) but they have been analyzed again to obtain an homogeneous dataset of observations.

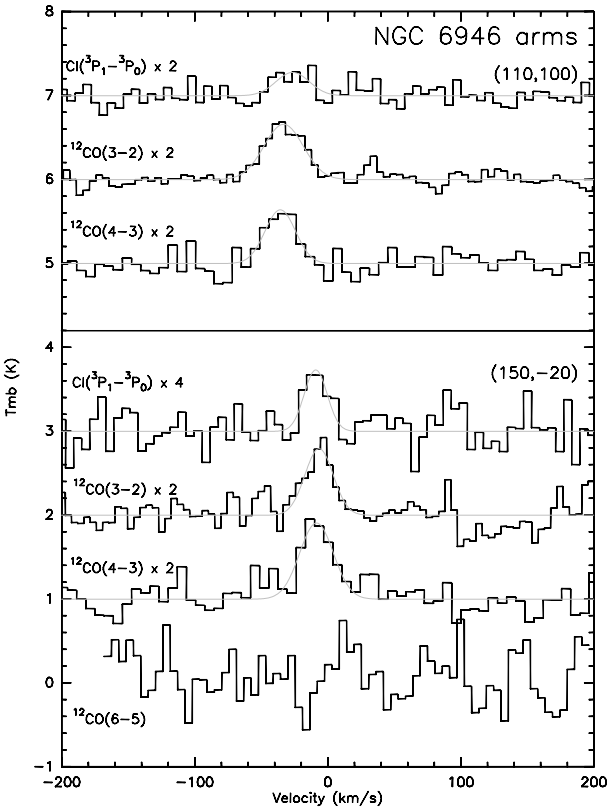

Fig. 16. Spectra taken towards the NGC 6946 arms at the offset positions (110″, 100″) (*top*) and (150″, −20”) (*bottom*) (relative to the central position (0″, 0″) listed in Table 1, see also Table B.1). See the caption of Fig. 1.